BARYON RESONANCES ON THE LATTICE:

THE P-WAVE NUCLEON-PION SCATTERING AMPLITUDE

IN THE $\Delta(1232)$ CHANNEL

By

Giorgio Silvi, M.Sc.

Advisor: Prof. Dr. Dr. Thomas Lippert

A dissertation submitted in partial fulfillment of
the requirements for the degree of

DOKTOR DER NATURWISSENSCHAFTEN

BERGISCHE UNIVERSITÄT WUPPERTAL
Fakultät für Mathematik und Naturwissenschaften

2021

BARYON RESONANCES ON THE LATTICE:

THE P-WAVE NUCLEON-PION SCATTERING AMPLITUDE

IN THE Δ(1232) CHANNEL

Abstract

by Giorgio Silvi, M.Sc.
Bergische Universität Wuppertal
2021

We present the determination of the $\Delta(1232)$ resonance parameters using lattice QCD and the Lüscher method. The resonance couples to the elastic pion-nucleon scattering with $J^P = 3/2^+$ in the isospin $I = 3/2$ P-wave channel. Our $N_f = 2 + 1$ flavor lattice setup features a pion mass of $m_\pi \approx 250$ MeV, such that the strong decay channel $\Delta \to \pi N$ is open for decay. We use the projection method for constructing the required lattice correlation functions from single- and two-hadron interpolating fields and their projection to irreducible representations of the lattice's relevant symmetry group. We show the energy spectra results in selected moving frames and irreducible representations and extract the scattering phase shifts P_{33} and S_{31}. From the determined pole position of the $\Delta(1232)$, we derive the resonance mass $m_\Delta = 1378(7)(9)$ MeV and the coupling $g_{\Delta-\pi N} = 23.8(2.78)(0.9)$.

ACKNOWLEDGMENT

There are several people without whom this dissertation might not have been written and to whom I am greatly indebted. I would like to express my deepest gratitude to my supervisors Prof. Dr. Dr. Thomas Lippert and Prof. Dr. Stefan Krieg for their full support and guidance on this journey. A special thank goes to the Lattice QCD group I have been part of in the last years; from Dr. Luka Leskovec for the immense help, especially in my first steps in the lattice topics, to Prof. Stefan Meinel for his expert guidance in all aspects of the theory, and the other colleagues for the countless brilliant and consistent advice. I would also like to thank Dr. Eric Gregory for the kind help and assistance in my everyday life at JSC. Finally, I want to thank my friends and family, who never ceased to support and push me through this venture.

TABLE OF CONTENTS

LIST OF TABLES

viii

LIST OF FIGURES

x

Dedication

To Barbara

Chapter One

Introduction

The strong force is one of the four known fundamental forces of nature that governs the interaction between quarks, the fundamental subatomic elements that build hadrons such as the protons and neutrons that make up atomic nuclei. The strong interactions are described by quantum chromodynamics (QCD), a quantum field theory developed in the second half of the 20th century to expand the theoretical framework describing particles' nature. QCD was developed in analogy with the successful quantum electrodynamics (QED), the electromagnetic force's quantum field theory. The counterpart of the electrical charge for strong force is the *color*, which comes in three different types of charges[1], or three anti-color charges. Asymptotically every particle has to be color-neutral, which can be achieved by objects made of three valence quarks known as *baryons*, or a pair of quark and antiquark called *mesons*. In QED, the photon is the force carrier particle, while in QCD it is the gluon; although both are massless, the latter carries the color charge, which enables the gluons to radiate further carrier particles. This feature limits the range at which the strong force can act. Opposite to the infinite range of the electromagnetic force, the strong has a short-range of about 1 fm (or 10^{-15} meter). This aspect also contributes to the confinement of quarks, as they have been observed only in composite particles. The interaction of two quarks creates a narrow flux-tube of color fields in between. As the spatial distance between the two quarks increases, the flux-tube's energy increases as well until, eventually, it becomes energetically preferable for a new quark-antiquark pair to appear from the vacuum spontaneously. At ordinary temperatures, this confinement mechanism builds composite hadrons of size around 1 fm and makes it impossible to observe a single quark alone. At large energies, the coupling becomes increasingly smaller, giving rise to the *asymptotic freedom* that makes it possible to tackle QCD perturbatively. In the region of interest for this study, i.e., the low-lying baryon resonance $\Delta(1232)$, QCD is strongly interacting, and it can be tackled only non-perturbatively. Lattice-QCD is a non-perturbative approach for solving QCD formulated on a lattice of points in space and time. Numerical simulations usually produce results that come from approximations of real physics. Lattice-QCD instead is computed from first principles, with no need for ad-hoc assumptions. A good starting point to discuss Lattice QCD is by introducing the continuum theory and QCD's non-pertubative nature in the low-energy regime.

The work presented in this thesis comes from two projects: the first one, outlined in Chapter 2, Chapter 3, Chapter 4, and Chapter 5, is the main focus of this dissertation and shows

---

[1]The three charges are called blue, red, and green, but there is no connection to color in common sense

the determination of the $\Delta(1232)$ resonance parameters using lattice QCD and the Lüscher method. Result for this work has been presented in the following publication:

- Giorgio Silvi, Srijit Paul, Constantia Alexandrou, Stefan Krieg, Luka Leskovec, Stefan Meinel, John Negele, Marcus Petschlies, Andrew Pochinsky, Gumaro Rendon, Sergey Syritsyn, and Antonino Todaro. "P-wave nucleon-pion scattering amplitude in the $\Delta(1232)$ channel from lattice QCD". in: *Phys. Rev. D* 103 (9 May 2021), p. 094508. DOI: 10.1103/PhysRevD.103.094508. URL: https://link.aps.org/doi/10.1103/PhysRevD.103.094508

which follows the results previously presented in the proceeding in [2]. A similar project I was part of, studied the κ and K^* resonances in the meson sector and was presented in the publication:

- Gumaro Rendon, Luka Leskovec, Stefan Meinel, John Negele, Srijit Paul, Marcus Petschlies, Andrew Pochinsky, **Giorgio Silvi**, and Sergey Syritsyn. "I= 1/2 S-wave and P-wave K π scattering and the κ and K* resonances from lattice QCD". in: *Physical Review D* 102.11 (2020), p. 114520

Nonetheless, as my contribution in this study was limited, I decided to focus on the $\Delta(1232)$ study throughout this dissertation.

The other project, presented in Chapter 6, investigates the Roberge-Weiss transition endpoint in the analytic continuation of the QCD phase diagram with imaginary chemical potential and was published in:

- Claudio Bonati, Enrico Calore, Massimo D'Elia, Michele Mesiti, Francesco Negro, Francesco Sanfilippo, Sebastiano Fabio Schifano, **Giorgio Silvi**, and Raffaele Tripiccione. "Roberge-Weiss endpoint and chiral symmetry restoration in $Nf = 2+1$ QCD". in: *Physical Review D* 99.1 (2019), p. 014502

with the software developed for the computation published in:

- Claudio Bonati, Enrico Calore, Massimo D'Elia, Michele Mesiti, Francesco Negro, Francesco Sanfilippo, Sebastiano Fabio Schifano, **Giorgio Silvi**, and Raffaele Tripiccione. "Portable multi-node LQCD Monte Carlo simulations using OpenACC". in: *International Journal of Modern Physics C* 29.01 (2018), p. 1850010

- Claudio Bonati, Simone Coscetti, Massimo D'Elia, Michele Mesiti, Francesco Negro, Enrico Calore, Sebastiano Fabio Schifano, **Giorgio Silvi**, and Raffaele Tripiccione. "Design and optimization of a portable LQCD Monte Carlo code using OpenACC". in: *International Journal of Modern Physics C* 28.05 (2017), p. 1750063

1.1 QCD

The continuum QCD lagrangian in Minkowsky spacetime is given by

$$\mathcal{L}_{QCD} = \bar{\psi}_i (i(\gamma^\mu D_\mu)_{ij} - m\delta_{ij})\psi_j - \frac{1}{4} G^a_{\mu\nu} G^{\mu\nu}_a, \qquad (1.1)$$

quark flavor	symbol	charge (Q/e)	mass (Mev/c^2)
up	u	$+2/3$	~ 3
down	d	$-1/3$	~ 7
strange	s	$-1/3$	~ 140
charm	c	$+2/3$	~ 1800
bottom	b	$-1/3$	$\sim 4.2 \times 10^3$
top	t	$+2/3$	$\sim 170 \times 10^3$

Table 1.1 Quarks and their properties

where the γ^μ are Dirac matrices satisfying the anticommutation relation $\{\gamma^\mu, \gamma^\nu\} = 2g^{\mu\nu}$. The ψ_i are Dirac spinors of the quark field with mass m, each with 12 independent components: three colors and four spinor degrees of freedom. In addition, the quarks comes in different flavors called *up, down, strange, charm, bottom, top* (see Tab. 1.1). The gauge covariant derivative is defined as,

$$D_\mu = \partial_\mu - ig\mathcal{A}_\mu^a T_a, \tag{1.2}$$

where $g = \sqrt{4\pi\alpha}$ ($\hbar = c = 1$) is the dimensionless coupling constant, and the traceless hermitian generators T_a follow the commutation relation

$$\left[T^a, T^b\right] = f^{abc}T^c, \tag{1.3}$$

where f^{abc} are the totally antysymmetric structure constants of $SU(3)$ color group.

The gauge part of the QCD lagrangian is composed of gauge-invariant gluon field strength tensor defined as:

$$G_{\mu\nu}^a = \partial_\mu\mathcal{A}_\nu^a - \partial_\nu\mathcal{A}_\mu^a + gf^{abc}\mathcal{A}_\mu^b\mathcal{A}_\nu^c, \tag{1.4}$$

where $\mathcal{A}_\mu^a(x)$ are gluon fields, the element of the Lie algebra of gauge group $SU(3)$.

1.2 Lattice formulation

The QCD action is defined as:

$$S_{QCD} = \int d^4x \mathcal{L}_{QCD}, \tag{1.5}$$

and in the framework of Feynman's path integral, the action plays an important role. Given an observable $\mathcal{O}(\psi, \bar{\psi}, \mathcal{A}_\mu)$ the expectation values is computed as

$$\langle 0| \mathcal{O}(\psi, \bar{\psi}, \mathcal{A}_\mu) |0\rangle = \frac{1}{Z} \int \mathcal{D}\psi\mathcal{D}\bar{\psi}\mathcal{D}\mathcal{A}_\mu \mathcal{O}(\psi, \bar{\psi}, \mathcal{A}_\mu)e^{-iS_{QCD}}, \tag{1.6}$$

where the partition function Z is given by,

$$Z = \int \mathcal{D}\psi\mathcal{D}\bar{\psi}\mathcal{D}\mathcal{A}_\mu e^{-iS_{QCD}}, \tag{1.7}$$

where the integral is meant over all field configurations. However, this formula alone would be impossible to evaluate due to oscillating integrands, i.e., the imaginary exponent. A solution, called *Wick Rotation*, is to let the coordinate t take on imaginary value making the rotation in the complex plane $x^0 = t \to -ix_4 = -i\tau$. The integration measure becomes

$$dx^0 dx^1 dx^2 dx^3 \to -i dx^1 dx^2 dx^3 dx^4, \tag{1.8}$$

and the exponent in the path integral in Eq. (1.6) gets real. This allows the exponent to be used as a probability measure for a given Monte Carlo configuration to be sampled. However, a numerical calculation over a continuum field is not quite possible without discretization. Replacing continuum spacetime with discrete lattice points gives to the field a precise mathematical meaning. Introducing the lattice spacing a, the minimal distance between different points, now the fields are described at the grid points $x = na = n_\mu a \hat{\mu}$ with $n_\mu \in \mathbb{Z}$. Degrees of freedom are still infinite; therefore, we limit the infinite to a finite set of $N_x \times N_y \times N_z \times N_t$ points. To tame the finite volume effects that arise from limitation, a general rule of thumb is to set the lattice's spatial extent above the largest correlation length in the system, i.e., that of the pion ($\propto 1/m_\pi$). Analogously to statistical mechanics, the temperature of the system T is given by

$$T = \frac{1}{aN_t}, \tag{1.9}$$

where N_t is the number of lattice sites in the temporal direction, where we set thermal boundary conditions. Those are periodic/anti-periodic for boson/fermion fields according to the spin-statistics theorem [7]. For zero-temperature studies, the temporal lattice range has to extend far above the pion correlation length. The introduction of a finite lattice spacing has a second effect: it acts as momentum cut-off, making integrations of Feynman integrals ultraviolet finite. This regularization merely corresponds to defining what we mean by path integral. Eventually, one would like to recover physics in the continuum limit removing the lattice structure $a \to 0$. As a decreases, the number of lattice points has to increase to maintain the physical volume constant (ideally, before sending a to zero, one would reach the thermodynamic limit).

1.3 Fields on the lattice

In this section, we introduce the boson and fermion fields suited for the lattice scheme. Additional details can be found in [8, 7]. The QCD action can be divided into the fermionic part S_F and the gauge part S_G. In general, it is possible to perform lattice simulations of a theory of pure gauge fields without fermions, known as *quenched* QCD.

1.3.1 Gauge fields: Wilson gauge action

We have seen in Sec. 1.1 that requiring to preserve local gauge invariance in the continuum lagrangian introduces the gauge fields A_μ through the covariant derivative in Eq. (1.2). On the lattice, the gauge fields are replaced by the link variables $U_\mu(x)$ that can be expressed

as the path-ordered exponential function,

$$U_\mu(x) = P \exp \left(ig \int\limits_{x}^{x+a\hat\mu} dx_\mu A_\mu(x) \right), \tag{1.10}$$

where the integral is carried along a path connecting the point x and $x+a\hat\mu$. These variables live on the link connecting two nearby sites, a segment oriented as $\hat\mu$ of length equal to the lattice spacing a. Now, we can construct a strictly gauge-invariant gauge action from the link variables. It can be easily built by taking the product of link variables around the smallest closed loop on the euclidean spacetime. Called Wilson *plaquette*, it is an elementary square in the $\mu\nu$ plane,

$$U_{\mu\nu}(x) = U_\mu(x)U_\nu(x+\hat\mu)U_\mu^\dagger(x+\hat\nu)U_\nu^\dagger(x), \tag{1.11}$$

where the link variables are path-ordered. To handle products of four-link variables in an organized way, it is useful to use the Baker-Campbell-Hausdorff formula

$$\exp(A)\exp(B) = \exp(A + B + \frac{1}{2}[A,B] + \dots), \tag{1.12}$$

where A and B are arbitrary matrices, and the dots indicate powers larger than two, which are omitted. Applying to the plaquette in Eq. (1.11), we end up with

$$U_{\mu\nu} = \exp\left(ia^2 G_{\mu\nu}(n) + \mathcal{O}(a^3)\right), \tag{1.13}$$

Finally, we can write the Wilson gauge action for a general non-abelian group $SU(N)$,

$$S_G^{Wilson} = \frac{\beta}{N} \sum_x \sum_{\mu<\nu} \text{Re}\left(\text{Tr}(\mathbb{1} - U_{\mu\nu}(x))\right) = \frac{a^4}{2g^2} \sum_x \sum_{\mu<\nu} \text{Tr}(G_{\mu\nu}^2(x)) + \mathcal{O}(a^2), \tag{1.14}$$

with the inverse coupling $\beta = 2N/g^2$. In the last term is used the expansion of the exponential in Eq. (1.13). In the limit $a \to 0$, this term reproduce the correct continuum gauge action,

$$S_G = \frac{1}{2g^2} \int d^4x \text{Tr}(G_{\mu\nu}^2). \tag{1.15}$$

1.3.2 Fermion fields

We can now move to the case of the Dirac fermion field. Consider the Lagrangian density,

$$\mathcal{L} = \bar\psi_\alpha \left(i\partial^\mu (\gamma_\mu)_{\alpha\beta} - m\delta_{\alpha\beta} \right) \psi_\beta, \tag{1.16}$$

where ψ is a 4-component field, and γ_μ are the Dirac matrices.

Moving from the Minkowski to the Euclidean metric, the gamma matrices becomes $\gamma_4^E = \gamma^0$, $\gamma_i^E = -i\gamma^i$. The euclidean action takes the form,

$$S_E = \int d^4x \bar\psi \left(\partial_\mu \gamma_\mu^E + m \right) \psi. \tag{1.17}$$

The derivative in the fermion Lagrangian appears at the first power; hence, there is no longer freedom in the choice of the analogous discrete term. The only derivative anti-hermitian by itself is the symmetric derivative,

$$\Delta_\mu^S \psi(x) = \frac{1}{2a} \left(\psi(x + \hat{\mu}) - \psi(x - \hat{\mu}) \right). \tag{1.18}$$

Thus the discrete Euclidean action takes the form of the so-called *naive fermion action*,

$$S_E^D = a^4 \sum_{\hat{\mu},x} \bar{\psi}(x) \gamma_\mu^E \frac{\psi(x + \hat{\mu}) - \psi(x - \hat{\mu})}{2a} + \sum_x \bar{\psi}(x) m \psi(x). \tag{1.19}$$

This can be rewritten further as a term bilinear in the fermion fields,

$$S_E^D = a^4 \sum_x \bar{\psi}(x) M \psi(x), \tag{1.20}$$

where M is the fermion matrix,

$$M = \sum_\mu (\gamma_\mu^E) \frac{[\delta_{x,x'+\hat{\mu}} - \delta_{x,x'-\hat{\mu}}]}{2a} + m. \tag{1.21}$$

To use Feynman's functional integral, we have to ensure that the fields satisfy the correct anti-commutation relations. It is then necessary to introduce Grassman numbers, which satisfy the following conditions

$$\{\eta_i, \eta_j\} = 0 \ ; \ \frac{\partial \eta_i}{\partial \eta_j} = \delta_{ij} \ ; \ \int d\eta_i = 0 \ ; \ \int d\eta_j \eta_i = \delta_{ij}. \tag{1.22}$$

Next, we integrate over Grassmann 4-component spinors $\psi(x)$ and $\bar{\psi}(x)$. Using series expansion for the powers in the exponential, we get

$$\int \prod_x d\bar{\psi}(x) \prod_y d\psi(y) e^{-\bar{\psi}(k) M_{kl} \psi(l)} = \mathcal{N} \det(M),$$

$$\int \prod_x d\bar{\psi}(x) \prod_y d\psi(y) e^{-\bar{\psi}(k) M_{kl} \psi(l)} \bar{\psi}(i) \psi(j) = \mathcal{N} \det(M) M_{ij}^{-1}, \tag{1.23}$$

$$< \bar{\psi}(x) \psi(y) > = M_{x,y}^{-1}. \tag{1.24}$$

The Fourier transform of the inverse of matrix M gives the free fermion propagator,

$$\tilde{M}^{-1}(p) = \frac{m - i a^{-1} \sum_\mu \gamma_\mu^E \sin(p_\mu a)}{m^2 + a^{-2} \sum_\mu \sin^2(p_\mu a)}, \tag{1.25}$$

and finally obtain, in the continuum limit,

$$< \psi_\alpha(x) \bar{\psi}_\beta(y) > = \lim_{a \to 0} \int_{-\frac{\pi}{a}}^{\frac{\pi}{a}} \frac{d^4 p}{(2\pi)^4} \frac{\left[-i \sum_\mu (\gamma_\mu^E) \frac{\sin(p_\mu a)}{a} + m \right]_{\alpha\beta}}{\sum_\mu \frac{\sin^2(p_\mu a)}{a^2} + m^2} e^{i p_\nu (x-y)_\nu}. \tag{1.26}$$

In the limit $a \to 0$ the quantity $\frac{sin(p_\mu a)}{a}$ stays finite both in the infrared region ($p_\mu = 0$) and in ultraviolet region ($p_\mu = \pm\frac{\pi}{a}$).

It seems we end up with an incorrect limit, with non-physical contributions. Even worse, they double for each dimension, ending up with a total of $16 = 2^4 = 2^d$ different regions of contribution in momentum space, with only one of them being physical. This problem, known in the literature as *fermion doubling*, has its origin in the use of the symmetric derivative. It is possible to fix those unwanted extra spurious doublers with the Wilson term,

$$\tilde{M}^{-1}(p) = m + \frac{i}{a} \sum_\mu \left(\gamma_\mu^E \sin(p_\mu a) + \frac{i}{a}(1 - \cos(p_\mu a)) \right), \qquad (1.27)$$

where the extra 15 doublers get proportional to a^{-1}, thus infinitely heavy in the continuum limit. While for the proper pole with $p_\mu = 0$, the correct fermion mass is kept in place.

Interactive fermion action

It is now time to couple the fermion and gauge fields together. This merely means modifying the derivative to the covariant derivative adding the link variables U_μ, which transform the interactive fermion action as,

$$S_F^{D(wilson)} = a^4 \sum_{\hat{\mu},x} \bar{\psi}(x)\gamma_\mu^E \frac{U_\mu(x)\psi(x+\hat{\mu}) - U_{-\mu}(x)\psi(x-\hat{\mu})}{2a} + \sum_x \bar{\psi}(x)m\psi(x), \qquad (1.28)$$

where $U_{-\mu}(x) = U_\mu(x-\hat{\mu})^\dagger$. Eq. (1.28) is a combination of two forward derivatives, i.e., a discretization of $-(a/2)\mathcal{D}_\mu\mathcal{D}_\mu$ and will vanish in the continuum limit. In general, mass terms explicitly break chiral symmetry[2], but in the chiral limit $m \to 0$, chiral symmetry is restored. However, the Wilson action breaks the chiral invariance explicitly even in the chiral limit; a price to pay to remove the unphysical fermion excitations.

The complete action for fermion and gauge fields then reads

$$S[U, \bar{\psi}, \psi] = S_G[U] + S_F[U, \bar{\psi}, \psi], \qquad (1.29)$$

where we emphasize the dependences. Notice that both the gauge action and the fermion action depend on the fields $A_\mu(n)$ through the link $U_\mu(n)$. This means that in the functional integral is possible to substitute the integration measure $D[A_\mu(n)]$ with $D[U_\mu(n)]$.

1.4 Improvements

1.4.1 Symanzik gauge action

In this section, we introduce Symanzik's improvement [9, 10] for the Wilson action in Eq. (1.14) that aims to approach the continuum limit quicker by subtracting an extra term in action, i.e., minimizing the consequence of a non-zero lattice spacing.

---

[2]the invariance of the action for transformations in flavor space

We have to remember that the discretization we have chosen is not unique, and, as long as we keep the continuum limit unchanged, it's possible to add different terms. This is equivalent to a change of the regularization scheme. Symanzik has shown [11] that every Lagrangian field theory on the lattice in d dimension yield the same on-shell matrix elements of an effective local Lagrangian in the continuum of the type

$$\mathcal{L}_{latt} \simeq \mathcal{L}_{eff} = \sum_i c_i^{(0)} \mathcal{O}_i^{(0)} + a^2 \sum_i c_i^{(2)} \mathcal{O}_i^{(2)} + a^4 \sum_i c_i^{(4)} \mathcal{O}_i^{(4)} + \dots, \tag{1.30}$$

where $\mathcal{O}_i^{(n)}$ are local operators of dimension $d + n$. Then, in order to build an improved lattice action, the corresponding effective Lagrangian will have the form,

$$\mathcal{L}_{latt,impr} \equiv \mathcal{L}_{eff,impr} = \mathcal{L} + a^{2p} \sum_i c_i^{(2p)} \mathcal{O}_i^{(2p)} + \dots, \tag{1.31}$$

using appropriate linear combinations of operators $\mathcal{O}_i^{(2p)}$ where p is an integer. Its a non-trivial task determining the coefficients c_i, and there are several different ways to do it, both numerically and perturbatively [12].

In our simulation, we use a *tree-level* $O(a^2)$ improved Symanzik gauge action; thus, lattice artifacts are corrected only in part. This is done by showing that the Wilson action is equivalent on the continuum to the effective Lagrangian

$$\mathcal{L}_{eff} = -\frac{1}{4} F_{\mu\nu} F^{\mu\nu} + \frac{1}{12} a^2 \partial_\mu F_{\mu\nu} \partial^\mu F^{\mu\nu} + \mathcal{O}(a^4), \tag{1.32}$$

thus, to cancel out the $\mathcal{O}(a^2)$ term, we add an irrelevant operator.

The choice for this work is

$$S_g^{Sym} = \beta \left[\frac{c_0}{3} \sum_{\text{plaq}} \text{ReTr}(1 - U_{\text{plaq}}) + \frac{c_1}{3} \sum_{rectq} Re\, Tr(1 - U_{rect}) \right], \tag{1.33}$$

where U_{plaq} and U_{rect} are respectively square (1×1) and rectangular (1×2) loop. The parameters c_i are set to their tree-level values $c_1 = -1/12$ and $c_0 = 1 - 8c_1 = 5/3$.

1.4.2 Clover-improved Wilson fermion

It is also possible to improve the Wilson lattice fermion action to $O(a)$ level. This is done by adding the so-called *clover term* to obtain the following improved action

$$S_f^{SW} = S_f^W[V] - \frac{c_{SW}}{2} \sum_x \sum_{\mu<\nu} (\bar{\psi} \sigma_{\mu\nu} F_{\mu\nu}[V] \psi)(x), \tag{1.34}$$

with $\sigma_{\mu\nu} = \frac{i}{2}[\gamma_\mu, \gamma_\nu]$ and the *Sheikholeslami-Wohlert* coefficient [13] is set to the tree level value $c_{SW} = 1$. The lattice field strength tensor $F_{\mu\nu}$ can be written as

$$F_{\mu\nu}(x) = \frac{-i}{8a^2} (Q_{\mu\nu}(x) - Q_{\nu\mu}(x)) \tag{1.35}$$
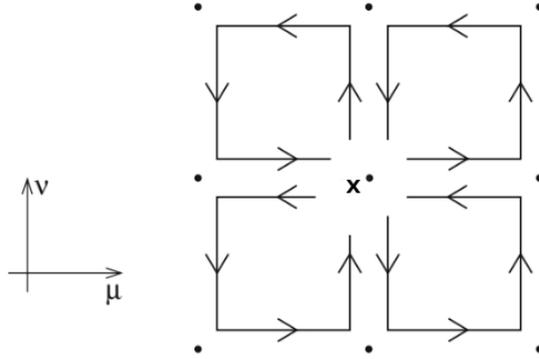
Figure 1.1 Clover term graphical representation: sum $Q_{\mu\nu}(x)$ of plaquettes $U_{\mu,\nu}(x)$

where $Q_{\mu\nu}(x)$ (shown in Fig. 1.1) is the sum of plaquettes $U_{\mu,\nu}$ in the $\mu - \nu$ plane as

$$Q_{\mu\nu}(x) = U_{\mu,\nu}(x) + U_{\nu,-\mu}(x) + U_{-\mu,-\nu}(x) + U_{-\nu,\mu}(x) \tag{1.36}$$

where the plaquettes are computed for smeared links V that have undergone two levels of HEX smearing [14]. HEX derives from the HYP setup [15], but with stout/EXP smearing [16] rather than the standard APE smearing [15]. When smoothing or smearing, one replaces the link variables by local averages over short paths connecting the link endpoints. Smearing techniques are used to reduce violent short distance fluctuations of the gauge fields, leading to improved long-distance correlation functions.

Chapter Two

Resonances

Most hadrons are observed experimentally as resonances: particles with very short lifetimes (e.g., $10^{-23}s$) that manifest themselves as structures in experimental observables. In an experiment, the typical process for the formation of resonances (R) is usually of the form

$$A + B \rightarrow R \rightarrow C_1 + \cdots + C_n, \tag{2.1}$$

where an energy scan makes them appearing (ideally) as peaks in scattering cross-sections. When the structure appears narrow, and there are no other resonances nearby or relevant thresholds, the resonance can be fitted employing a Breit-Wigner parametrization (Sec. 5.4). However, the rich phenomena of resonances with its vast range of widths (from few to several hundreds of MeV) and often overlaps of similar quantum numbers, call for refined parametrization that combined resonances terms in a non-trivial way, e.g., the K-matrix approximation (Sec. 2.5). When the process in Eq. (2.1) involves the same in- and out-going particles, the scattering is regarded as elastic, which offers a more straightforward theoretical treatment.

When it comes to low-energy (or low-momentum transfer), QCD perturbative methods can not be applied. Quarks and gluons are confined within color-neutral hadrons with a complex structure that requires non-perturbative methods such as Lattice QCD. The study of resonances and the determination of their parameters in the last decade has mainly focus on low-lying meson resonances, in particular the low-lying ρ meson [17, 18, 19, 20, 21, 22, 23, 24, 25, 26, 27, 28, 29, 30, 31, 32, 33, 34]. This initial round of studies served as the first evidence of the applicability, in LQCD calculation, of the Lüscher method. At present, elastic meson-meson scattering is already achieving high-precision measurement, establishing a solid foundation for more complex scattering processes.

On the other hand, scattering involving baryon-meson is far less established, with few studies published at present date [35, 36, 37, 38, 39, 40, 41, 42]. Scattering amplitudes involving baryon have more difficulties when compared to the pure meson-meson sector [43]. The signal-to-noise ratio in baryon correlation functions is known to be generally worse than the meson interpolators [44, 45], with the former running as $\propto e^{(m_B - 3/2m_\pi)t}$ and the latter as $\propto e^{(m_M - m_\pi)t}$. Wick contractions also escalate with the additional valence quarks included, leading to higher storage and computational cost. Moreover, on the group-theoretical side, the half-integer spin of baryons complicates the construction of irrep-projected operators [46].
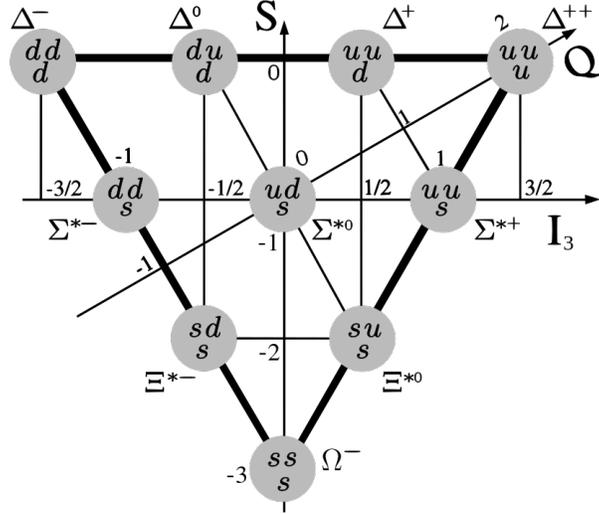
Figure 2.1 Baryon decuplet of spin-$\frac{3}{2}$ with the Δ family on the top row.

2.1 The $\Delta(1232)$ baryon resonance
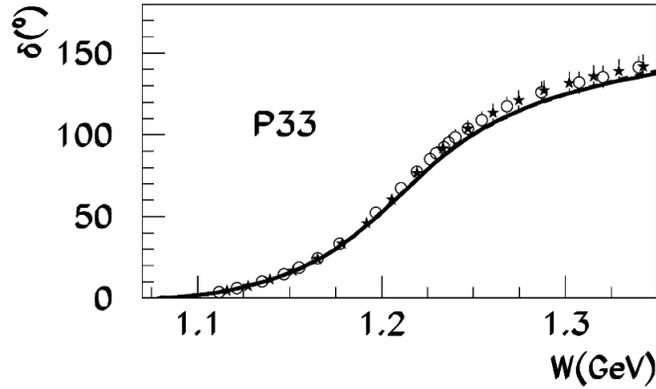
Figure 2.2 Phase shift P_{33} ($l = 1, I = 3/2, J = 3/2$) for nucleon-pion system from fit to experimental data [47]. The change in the value of the phase shift δ signal the onset of the resonance. The center-of-mass energy value at which the phase shift cross $90°$ is where the scattering amplitude reaches its maximum.

In this work, the focus is the $N\pi \rightarrow N\pi$ elastic scattering in the $I = 3/2$ and $J^P = 3/2^+$ channel where the lowest-lying baryon resonance, i.e., the $\Delta(1232)$ is located. In particular, we aim to extract the phase shift in the elastic region (see Fig. 2.2), which is the region between the $N\pi$ and $N\pi\pi$ thresholds. First observed in pion-nucleon scattering [49], the $\Delta(1232)$ can also be produced when energetic photons or neutrinos hit a nucleon [50].

The Δ baryons come in nature in a family of four composed particles of u and d quarks:

11

Particle	J^P	$\Gamma_{N\pi}[MeV]$
$\Delta(1232)$	$3/2^+$	112.4(5)
$\Delta(1600)$	$3/2^+$	18(4)
$\Delta(1620)$	$1/2^-$	37(2)
$\Delta(1700)$	$3/2^-$	36(2)
$\ldots$	$\ldots$	$\ldots$

Table 2.1 The $\Delta(1232)$ and nearby resonances with listed J^P and decay width in $N\pi$ [48].

$\Delta^-, \Delta^0, \Delta^+$ and Δ^{++} (see Fig. 2.1). Due to isospin symmetry in u and d quarks on the lattice, the four variants have the same properties. Thus, in the following, we choose to consider only the $\Delta^{++}(I_3 = +3/2)$.

The Particle Data Group (PDG) [51] describes the $\Delta(1232)$ resonance as follow:

- Mass m: Re (pole position) ≈ 1210 MeV / Breit-Wigner mass ≈ 1232 MeV

- Width Γ: 2 Im (pole position) ≈ 100 Mev / Breit-Wigner full width ≈ 117 MeV

- Decay modes:

  $N\pi$: 99.4%

  $N\gamma$: $0.55 - 0.65\%$

where the width [1] corresponds to a lifetime $\tau = \frac{\hbar}{\Gamma} \sim 5 \times 10^{-24} s$. The strong decay dominance in the nucleon-pion system shows an almost completely elastic process (visible in Fig. 2.5) [48]. Nevertheless, nearby resonances with equal or similar quantum numbers (see Tab. 2.1) urge us to take into account possible small contributions on the phase shift [52]. This fact is of particular relevance considering lattice irreps that combine several infinite-volume angular momenta, thus mixing different phase shift contributions.

In the next section, we revisit the concepts and methods used to parametrized the scattering amplitudes of resonances in scattering processes.

2.2 Quantum mechanical scattering

In the following, we present a quick review [53] of the methods that lead to the partial waves parametrization, often implemented to examine how states with definite angular momenta are affected by the scattering (for a broader introduction see e.g. [54, 55, 56]).

Let us start from the Hamiltonian of two-body system particles of mass m_1, m_2 combined with a short-ranged potential V,

$$H = \frac{\vec{p_1}^2}{2m_1} + \frac{\vec{p_2}^2}{2m_2} + V, \tag{2.2}$$

---

[1]It correspond to the physical width only at physical pion mass
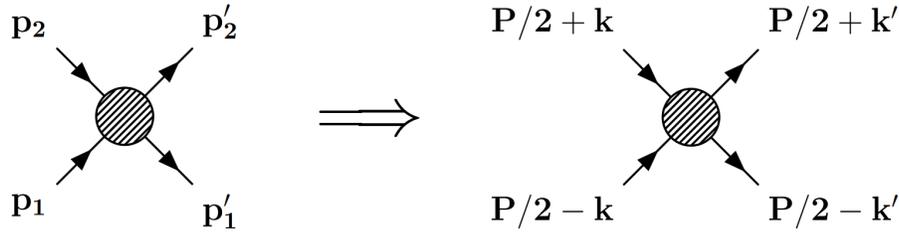
Figure 2.3 Kinematics in laboratory frame and relative coordinates.

It is then convenient to switch to relative and center of mass coordinates (see Fig. 2.3),

$$\vec{r} = \vec{r}_1 - \vec{r}_2, \qquad \vec{R} = \frac{m_1\vec{r}_1 + m_2\vec{r}_2}{m_1 + m_2}, \tag{2.3}$$

$$\vec{k} = \frac{m_2\vec{p}_1 - m_1\vec{p}_2}{m_1 + m_2}, \qquad \vec{P} = \vec{p}_1 + \vec{p}_2, \tag{2.4}$$

which transform the Hamiltonian as

$$H = \frac{\vec{P}^2}{2M} + \frac{\vec{k}^2}{2\mu} + V = T_{cm} + H_{rel}, \tag{2.5}$$

where $M = m_1 + m_2$ and the reduced mass is $\mu = m_1 m_2/M$. The potential now is described only with a dependence on the relative coordinates so that we can split the total wave function in waves for center-of-mass motion and relative motion:

$$|\Psi\rangle = |\psi_{cm}\rangle |\psi_{rel}\rangle, \tag{2.6}$$

where $|\psi_{cm}\rangle$ depends only on the kinetic energy (through total momentum $\vec{P}$), while $|\psi_{rel}\rangle$ encapsulate the scattering momentum $\vec{k}$. The problem is now turned effectively into a one-body problem, and setting $\vec{P} = 0$, we can focus on the wave function $|\psi_{rel}\rangle$ only (we will drop the label *rel* from now on). This describes an elastic scattering on potential V from an incoming $\vec{k}$ to an outgoing $\vec{k}'$ with $|\vec{k}| = |\vec{k}'|$ and $E = k^2/(2\mu)$(with $\hbar = 1$). The process can be view in terms of an incoming (incident) plane-wave and an outgoing (scattered) spherical-wave,

$$\psi^{(+)}(\vec{r}) = \psi_{in}(\vec{r}) + \psi_{sc}(\vec{r}) = \frac{e^{i\vec{k}\cdot\vec{r}}}{(2\pi)^{3/2}} + \psi_{sc}(\vec{r}), \tag{2.7}$$

and assuming that the potential V falls off faster than $1/r$, then the wave function has an asymptotic form,

$$\psi^{(+)} \xrightarrow[r\to\infty]{} (2\pi)^{-3/2}(e^{i\vec{k}\cdot\vec{r}} + f(k,\theta,\phi)\frac{e^{ikr}}{r}), \tag{2.8}$$

with scattering angle θ given by $\cos\theta = \hat{k}\cdot\hat{k}'$ (see Fig. 2.4). In Eq. (2.8) is introduced the scattering amplitude f, which encapsulates the physical information about the scattering. It

13
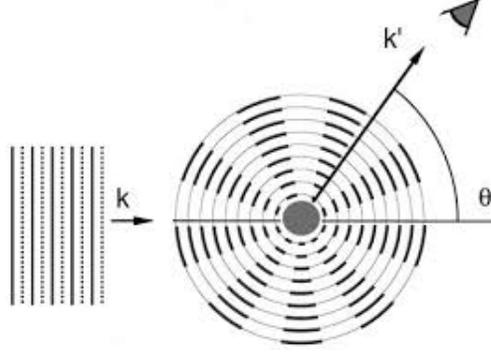
Figure 2.4 Scattering problem for an incident plane wave on a spherical target.

modulates the out-going spherical wave function with a dependence on the scattering angles (relative to the beam direction).

The differential cross section is defined as,

$$\frac{d\sigma}{d\Omega}(k,\theta,\phi) = \frac{\text{number of scattered particles into } d\Omega \text{ per unit time}}{\text{number of incident particles per unit area and time}} = \frac{S_{sc}r^2}{S_{in}}, \tag{2.9}$$

where S_{sc} and S_{in} represent the scattered and incident probability densities,

$$S_{in} = \text{Re}(\psi_{in}^* \frac{d}{dz}\frac{1}{i\mu}\psi_{in}) = \text{Re}(e^{-ikz}\frac{1}{i\mu}ike^{ikz}) \propto \frac{k}{\mu}, \tag{2.10}$$

$$S_{sc} = \text{Re}(\psi_{sc}^* \frac{d}{dr}\frac{1}{i\mu}\psi_{sc}) = \text{Re}(f^*\frac{e^{-ikr}}{r}\frac{1}{i\mu}ikf\frac{e^{ikr}}{r}) + \mathcal{O}(\frac{1}{r^3}) \propto \frac{k}{\mu r^2}|f|^2 + \mathcal{O}(\frac{1}{r^3}), \tag{2.11}$$

which reduce the differential cross section to

$$\frac{d\sigma}{d\Omega}(k,\theta,\phi) = |f(k,\theta,\phi)|^2. \tag{2.12}$$

Now, considering a more straightforward case where we do not consider spin observables, e.g., the spin orientation of at least one of the particles is known (polarized), then the scattering amplitude $f(k,\theta,\phi)$ is independent of ϕ, and we can then drop this dependence.

Expanding the wave function in spherical coordinates,

$$\psi(r,\theta) = \sum_{l=0}^{\infty} c_l \frac{u_l(r)}{r}Y_{l0}(\theta,\phi) = \sum_{l=0}^{\infty} \tilde{c}_l \frac{u_l(r)}{r}P_l(\cos\theta), \tag{2.13}$$

where there is only the spherical harmonic $Y_{l0}(\theta,\phi) = \langle\theta,\phi|l,m_l = 0\rangle$, because there is no ϕ dependence, so it can be used $Y_{l0} = \frac{2l+1}{4\pi}P_l(\cos\theta)$. The radial Schröedinger equation,

$$\frac{d^2u_l}{dr^2} - \left[\frac{l(l+1)}{r^2} + 2\mu V - k^2\right]u_l = 0, \tag{2.14}$$

14

is satisfied by the radial part $u_l(r)$ of the wave function (if there is no mixing of different l values) with solutions of the kind,

$$u_l(r) = C \sin kr + D \cos kr, \tag{2.15}$$

which we can rewrite in the form

$$u_l(r) = B \sin(kr - l\pi/2 + \delta_l), \quad C = B \cos \delta_l, \ \ D = B \sin \delta_l, \tag{2.16}$$

where the values of B and δ_l are determined by the exact solution, which depends on the potential V.

2.3 Partial waves and S-matrix

In general, resonances have a well-defined spin. Angular momentum is conserved in a spherically symmetric central potential due to Noether's theorem. We expand the wave function in the angular momentum eigenstates and parametrized the scattering amplitude f in terms of a sum among the components of the partial wave

$$f(k, \theta) = \sum_{l=0}^{\infty} (2l + 1) f_l(k) P_l(\cos \theta). \tag{2.17}$$

The incoming plane can be expanded over all values of l as,

$$e^{i\vec{k}\cdot\vec{r}} = e^{ikr\cos\theta} = \sum_{l=0}^{\infty} (2l+1) i^l j_l(kr) P_l(\cos\theta) \xrightarrow[r\to\infty]{} \sum_{l=0}^{\infty} (2l+1) P_l(\cos\theta) \frac{e^{ikr} - (-1)^l e^{-ikr}}{2ikr}, \tag{2.18}$$

where is used the spherical Bessel function j_l in the limit of large r,

$$j_l(kr) \xrightarrow[r\to\infty]{} \frac{\sin(kr - l\frac{\pi}{2})}{kr} = \frac{1}{kr} \frac{e^{ikr} - (-1)^l e^{-ikr}}{2i}, \tag{2.19}$$

which contain both incoming and outgoing waves.

Finally, we can apply the partial-wave expansion to Eq. (2.8) and obtain

$$\psi^{(+)}(r) \xrightarrow[r\to\infty]{} (2\pi)^{-3/2} \sum_{l=0}^{\infty} (2l+1) P_l(\cos\theta) \frac{S_l(k) e^{ikr} - (-1)^l e^{-ikr}}{2ikr}, \tag{2.20}$$

where is introduced the partial wave S-matrix

$$S_l(k) = 1 + 2ik f_l(k), \tag{2.21}$$

For elastic scattering, the conservation of probability ensures that the S-matrix is unitary ($|S_l(k)|^2 = 1$). From the constrain given by the optical theorem [56] the S-matrix can be parametrized through the phase shift $\delta_l(k)$ as,

$$S_l(k) = e^{2i\delta_l(k)} = \frac{e^{i\delta_l(k)}}{e^{-i\delta_l(k)}}, \tag{2.22}$$

which also parametrize the scattering amplitudes $f_l(k)$ as

$$f_l(k) = \frac{S_l(k) - 1}{2ik} = \frac{e^{i\delta_l(k)} \sin \delta_l(k)}{k} = \frac{1}{k \cot \delta_l(k) - ik}. \tag{2.23}$$

Putting pieces together, the asymptotic wave function in Eq. (2.20) becomes

$$\psi^{(+)}(r) \xrightarrow[r\to\infty]{} (2\pi)^{-3/2} \sum_{l=0}^{\infty} (2l+1) P_l(\cos\theta) i^l e^{i\delta_l} \frac{\sin(kr - l\frac{\pi}{2} + \delta_l)}{kr}, \tag{2.24}$$

And, in terms of the phase shift, the total cross section is,

$$\sigma(k) = 4\pi \sum_{l=0}^{\infty} (2l+1)|f_l(k)|^2 = \frac{4\pi}{k^2} \sum_{l=0}^{\infty} (2l+1) \sin^2 \delta_l(k), \tag{2.25}$$

which can be related to the imaginary part of the scattering amplitude f at angle $\theta = 0$, through the *optical theorem*,

$$\sigma = \frac{4\pi}{k} \mathrm{Im} f(\theta = 0), \tag{2.26}$$

which connects the total cross section to the forward scattering amplitude. The phase factor δ_l derives from probability conservation; scattering must conserve the flux from the ingoing to the outgoing wave. The shift in phase causes the interference among the partial waves resulting not in the plane wave anymore, but in a scattered wave.

The S-matrix in Eq. (2.21) for the case of multi-channel scattering is parameterized as,

$$S_{ba} = \delta_{ba} + 2i f_{ba}, \tag{2.27}$$

where labels a, b indicated the scattering channels. From the unitarity of the S-matrix one gets for the diagonal element,

$$f_{aa} = \frac{\eta \exp(2i\delta_a) - 1}{2i}, \tag{2.28}$$

where δ_a denotes the phase shift from channel a to channel a. The additional parameter η refers to the inelasticity: $\eta = 1$ means purely elastic, while $\eta < 1$ infers absorption (e.g., excitation) or inelasticity (e.g., the production of extra particles in the outgoing state). The off-diagonal element for a two-channel problem is parametrized as $f_{ba} = \sqrt{1 - \eta^2}/2 \exp(i(\delta_b + \delta_a))$. The evolution in the energy scan of partial wave amplitude in Eq. (2.28) can be displayed in the trajectory of an Argand plot in the complex plane.

Fig. 2.5 shows the Argand plot for the P_{33} phase shift of the $N\pi$ scattering, where P_{33} is a nomenclature convention which refers to P-wave ($l = 1$) with isospin $I = 3/2$ and total angular momentum $J = 3/2$. From the center of the complex plane, an increase in energy corresponds to a counter-clockwise rotation around the unitarity circle. The inelasticity η parametrizes the center's distance; a pure elasticity would keep the trajectory on the unitarity circle at a fixed radius. For the vast majority of the energy range, it can be seen a purely elastic scattering, with a sign of inelasticity appearing only at the upper end of the energy scan caused by the crossing of the $N\pi\pi$ threshold. The depicted resonance $(P_{33})\Delta(1232)$ has an elasticity of 99.4% [48].
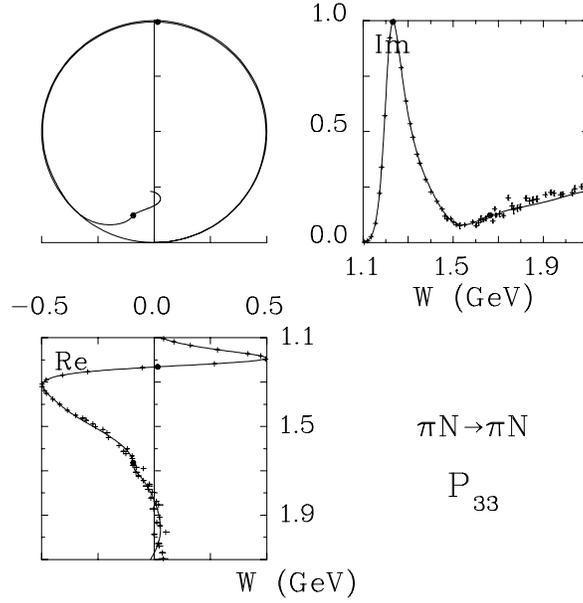
Figure 2.5 Argand plot in the complex plane as a function of c.m. energy (W) of the elastic P_{33} amplitude for $\pi N \to \pi N$. Also, the imaginary and the real part of the scattering amplitude are plotted against the c.m. energy. Taken from [48].

2.4 Pole structure

In a $2 \to 2$ scattering process, the 4-momenta p_i used to describe the kinematics represents a total of 12 independent variables. Nevertheless, the dynamic is constrained by 4 mass-shell conditions, i.e. $|\vec{p}_i|^2 = m_i^2$, 3 Lorentz boosts, and 3 rotations. This fact enables us to choose a smaller set of Lorentz invariant variables to describe the kinematics. A popular choice of variables is the Mandelstam variables (with only 2 of them being independent) defined as

$$s = (p_1 + p_2)^2 = (p_3 + p_4)^2 \tag{2.29}$$
$$t = (p_1 - p_3)^2 = (p_2 - p_4)^2 \tag{2.30}$$
$$u = (p_1 - p_4)^2 = (p_2 - p_3)^2, \tag{2.31}$$

where p_1, p_2 are the initial and p_3, p_4 the final 4-momenta of the particles. Using the on-shell mass condition $p_i^2 = m_i^2$ (with the rest mass m_i), one gets immediately

$$s + t + u = \sum_{i=1}^{4} p_i^2 = \sum_{i=1}^{4} m_i^2, \tag{2.32}$$

which can be visualized in the Mandelstam plane in Fig. 2.6.

This triangle's vertices in Fig. 2.6 refer to thresholds (sum of the square of rest masses of the incoming particles) that, once crossed, access the regions of elastic scattering. The S-matrix (Eq. (2.21)) is analytic in the Mandelstam plane, generally true up to its poles or

17
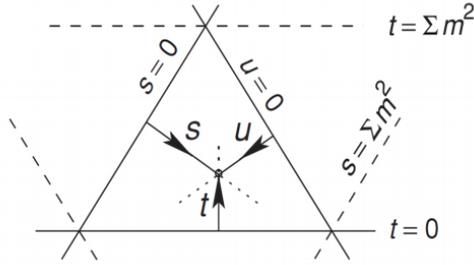
Figure 2.6 Mandelstam plane. The region on the bottom right where the Mandelstam variable s cross the threshold represents the physical region of scattering, also known as the s-channel.
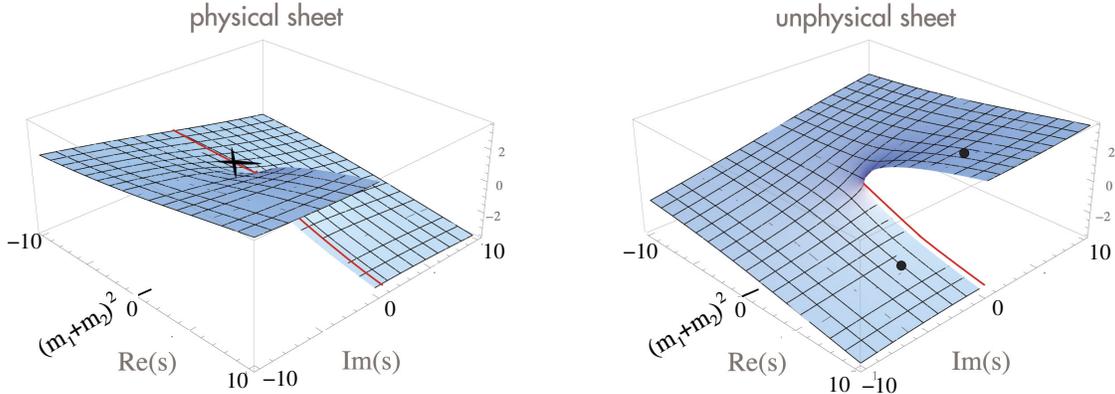
Figure 2.7 Riemann sheets: *physical* and *unphysical* sheets are connected smoothly along their discontinuities. The cross represents a bound state, while the dot indicates the resonance poles. The solid line is the physical axis (shifted by $i\epsilon$ into the physical sheet). Taken from [58].

branch points. Branch points onsets whenever there is a threshold (channel opening), which translates in Riemann sheets doubling [57]. Those are defined as *physical* and *unphysical* sheet (see Fig. 2.7) if they have, respectively, $\text{Im}(\sqrt{s - \sum m^2}) > 0$ or $\text{Im}(\sqrt{s - \sum m^2}) < 0$. Those sheets are analytically connected along the right-hand cut above the threshold. For example, the s-channel is the branch cut opening at $s = \sum m^2$ (see Fig. 2.6) that will open two sheets in the complex s-plane.

Poles refer to bound states, virtual states, or resonances. Bound states belong on the physical sheet on the real axis, while virtual states and resonances are located on the unphysical sheet closest to the physical one. Analyticity requires for each pole located in s to have a mirror pole located in the complex conjugate value at s^* (as in Fig. 2.7). A difference between these two poles is that the one located in the negative imaginary part is closer to the physical axis. Thus it has a more substantial influence on the observables in the resonance energy region.

2.5 K-matrix parametrization

In this section, is presented a brief review of the K matrix formalism [59], originally introduced to study resonances in nuclear reactions by Wigner [60] and Wigner and Eisenbud [61]. As discussed before, in a multi-channel scattering, the amplitude of an asymptotic initial state $|i\rangle$ to be found in an asymptotic final state $|f\rangle$ is

$$S_{fi} = \langle f| S |i\rangle \tag{2.33}$$

where S is the scattering operator (introduced in Eq. (2.21)). In order to exclude the case of non-interaction between the particle (the identity operator I), is common to parametrize it as

$$S^{(l)}(s) = I + 2iT^{(l)}(s), \tag{2.34}$$

where is defined the transition operator T (or T-matrix). The dependence is on the invariant mass of the system s and the partial wave l. A clear difference in the two parametrizations is that the S-matrix consider also the incident wave, while T-matrix parametrizes only the scattered wave. Conservation of probability infers the unitarity of the scattering operator, $SS^\dagger = S^\dagger S = I$ and subsequently, one gets

$$\frac{1}{2i}[T_{ij}^{(l)} - T_{ji}^{(l)*}] = \text{Im}\{T_{ij}^{(l)}\} = T_{ik}^{(l)*}\theta(s - s_{thr}^{(k)})T_{kj}^{(l)}, \tag{2.35}$$

where we assume that due to time-reversal of the strong interaction, $T^{(l)} = T^{(l)\intercal}$ [3]. Here the indices i, j label the channel of the scattering, and s_{thr} represent the threshold energy for the channel i. Equivalently,

$$\text{Im}\{T^{(l)-1}{}_{ij}\} = -\theta(s - s_{thr})\delta_{ij}. \tag{2.36}$$

One can now introduce the K operator to capture the real contribution of $T^{(l)-1}$ in the following way

$$\{T_{ij}^{(l)-1}\} = \{K_{ij}^{(l)-1}\} - \theta(s - s_{thr})\delta_{ij}, \tag{2.37}$$

and from time-reversal symmetry of S and T follows that K has to be real and symmetric. Multiplying Eq. (2.37) by K and T from left and right remove the inverse operators as

$$T^{(l)} = K^{(l)} + iT^{(l)}K^{(l)} = K^{(l)} + iK^{(l)}T^{(l)}, \tag{2.38}$$

which shows that operators K and T commute, i.e. $[K, T] = 0$.

To properly relate the K-matrix to the T-matrix under the S-matrix unitarity constraint, the imaginary part in Eq. (2.37) above threshold has to have the form $\text{Im}I_{ij} = -\rho_i(s)\theta(s - s_{thr})\delta_{ij}$. The Chew-Mandelstam function relates the real part to the imaginary part through a dispersion integral and also offers a smooth transition across the kinematic threshold [62]. Thus, as outlined in our previous work [3], in order to describe the correct analytic structure from the $N\pi$ threshold we define a two-body wave function for an initial and final state with a proper normalization of the two-particles states [63],

$$\rho_{ii} = diag\left(\sqrt{\left(1 - (\frac{m_a^i + m_b^i}{\sqrt{s}})^2\right)\left(1 - (\frac{m_a^i - m_b^i}{\sqrt{s}})^2\right)}\right), \tag{2.39}$$

where i label the scattering channel and a, b represent the two particles involved in the process (for us, that would be the nucleon and the pion). We can then define the rescaled T-matrix, $\hat{T}$,

$$T^{(l)} = \rho^{1/2}\hat{T}^{(l)}\rho^{1/2}, \tag{2.40}$$

as well as the rescaled K-matrix, $\hat{K}$, as

$$K^{(l)} = \rho^{1/2}\hat{K}^{(l)}\rho^{1/2}. \tag{2.41}$$

Finally, the scattering phase shift δ_l can be related to the K-matrix via

$$K^{(l)} = \tan(\delta_l), \tag{2.42}$$

or to the transition amplitude $T^{(l)}$ as

$$T^{(l)} = \frac{1}{\cot(\delta_l) - i}. \tag{2.43}$$

Chapter Three

Hadron Spectroscopy on the lattice

On the lattice, the study of two hadrons interactions requires the creation and annihilation of the hadrons through operators O tuned with the desired quantum numbers. These operators are then used to build correlation matrices to extract energies from the evaluation of matrices elements such as

$$C_{ij}(t) = \langle O_i(t_f)\bar{O}_j(t_i)\rangle = \sum_{n=1}^{\infty} e^{-E_n t}\psi_{ni}\psi_{nj}^*, \qquad \psi_{ni} = \langle 0| O_i |n\rangle, \tag{3.1}$$

where t_i is the source time, and t_f is the sink time. Also, $|n\rangle$ represents eigenstates of the Hamiltonians and is assumed a large temporal extent T. The correlation matrix elements are evaluated by performing the Wick contractions: the path integral over the quark fields for a certain configuration of the gauge-field.

We seek to use operators that maximize the overlap ψ_{ni} with low-energy states in this work. Consequently, use them to create projected operators that transform under the symmetry corresponding to the spin (or angular momentum) of interest. Strictly speaking, the aim is to maximize overlap with the states of interest while also reducing the variance in the estimate of the matrix element C_{ij}. In the next sections are shown the steps we follow to build the operators N, Δ, and $N\pi$, and project in the appropriate lattice irrep.

3.1 Interpolating operators

	Δ^{++}	π^+	N^+
J	3/2	0	1/2
I	3/2	1	1/2
I_3	+3/2	+1	+1/2
P	+1	-1	+1

Table 3.1 Quantum numbers of the hadrons under study: total angular momentum J, isospin I, third component of the isospin I_3, and parity P.

Below are presented first the unprojected operators of the three particles involved in the process to study. The chosen structures are pretty standard among the studies that implement the same type of particle states. In Tab. 3.1, a list of quantum numbers of the single hadrons relevant to this work is outlined.

3.1.1 Pion

The pion is a pseudoscalar meson with quantum numbers $I = 1, J^P = 0^-$ composed of a quark and an anti-quark. In Nature, it comes in a family of three particles: π^0, π^-, π^+. Our choice for interpolator for the positively charged pion ($I_3 = +1$) is:

$$\pi^+(\vec{p}) = \sum_{\vec{x}} \bar{d}(\vec{x})\gamma_5 u(\vec{x}) e^{i\vec{p}\cdot\vec{x}} \tag{3.2}$$

Under parity transformation $\mathcal{P}$ the operator in Eq. (3.2) shows the negative parity,

$$
\begin{aligned}
\pi^+(\vec{x}, x_0) &= \bar{d}(\vec{x}, x_0)\gamma_5 u(\vec{x}, x_0) \\
&\xrightarrow{\mathcal{P}} \bar{d}(-\vec{x}, x_0)\gamma_0\gamma_5\gamma_0 u(-\vec{x}, x_0) \\
&= -\bar{d}(-\vec{x}, x_0)\gamma_5 u(-\vec{x}, x_0) \\
&= -\pi^+(-\vec{x}, x_0)
\end{aligned}
\tag{3.3}
$$

Conjugating the interpolator in Eq. (3.2) gives the interpolators for the creation operator

$$\bar{\pi}^+(\vec{p}) = \sum_{\vec{x}} \bar{u}(\vec{x})\gamma_5 d(\vec{x}) e^{i\vec{p}\cdot\vec{x}} \tag{3.4}$$

3.1.2 Nucleon

The nucleon (with quantum numbers $I = 1/2, J^P = 1/2^+$) is a baryon made of three valence quarks representing the proton and neutron. The neutron is composed of udd quarks resulting in an overall neutral electric charge, while the proton has an electric charge $Q = +e$ from quark content uud. From the fact that the electric charge in QCD is not relevant, both proton and nucleon are related by isospin symmetry ($I = 1/2$) and are commonly represented by the nucleon operator.

The nucleon interpolator we implement is with $I_3 = +1/2$:

$$N_\mu(\vec{p}) = \sum_{\vec{x}} \epsilon_{abc}(\Gamma_1 u^a(\vec{x}))_\mu (u_\gamma^{bT}(\vec{x})(\Gamma_2)_{\gamma\delta} d_\delta^c(\vec{x})) e^{i\vec{p}\cdot\vec{x}} \tag{3.5}$$

where the combination (Γ_1, Γ_2) can assume the three values $(\gamma_5, C), (\mathbb{1}, C\gamma_5)$ and $(\mathbb{1}, C\gamma_0\gamma_5)$. These first two combinations belong to the restricted Lorentz group irrep $D(1/2, 0) \oplus D(0, 1/2)$ and the third to $D(1/2, 1) \oplus D(1, 1/2)$. After an initial assessment of the overlap of the three different combinations of (Γ_1, Γ_2) we restrict ourselves to the two best gammas combination overlapping with the nucleon state: $(\mathbb{1}, C\gamma_5)$ and $(\mathbb{1}, C\gamma_0\gamma_5)$. As an example, for the gamma combination $(\mathbb{1}, C\gamma_5)$ the nucleon operator transform under parity as,

$$
\begin{aligned}
N(\vec{x}, x_0) &= \epsilon_{abc} u_a(\vec{x}, x_0)(u_b^T(\vec{x}, x_0) C\gamma_5 d_c(\vec{x}, x_0)) \\
&\xrightarrow{\mathcal{P}} \epsilon_{abc}\gamma_0 u_a(-\vec{x}, x_0)(u_b^T(-\vec{x}, x_0)\gamma_0^T C\gamma_5\gamma_0 d_c(-\vec{x}, x_0)) \\
&= \epsilon_{abc}\gamma_0 u_a(-\vec{x}, x_0)(u_b^T(-\vec{x}, x_0) C\gamma_5 d_c(-\vec{x}, x_0)) \\
&= \gamma_0 N(-\vec{x}, x_0)
\end{aligned}
\tag{3.6}
$$

where we used $\gamma_u^T C = -C\gamma_u$. The nucleon creation operator is given by,

$$\bar{N}_\mu(\vec{p}) = \sum_{\vec{x}} \epsilon_{abc}(\bar{u}_b^T(\vec{x})\Gamma_2^{(i)}\bar{d}_c(\vec{x}))(\Gamma_1^{(i)}\bar{u}_a(\vec{x}))_\mu e^{i\vec{p}\cdot\vec{x}} \tag{3.7}$$

3.1.3 Delta

The Δ is a baryon with quantum numbers $I = 3/2$, $J^P = 3/2^+$. It can be obtained with a combination of gammas $(\Gamma_1, \Gamma_2) = (\mathbb{1}, C\gamma_j)$, where $j = x, y, z$. The spatial gamma matrix γ_j creates a diquark with $J = 1$, which, combined with the third quark outside $(J = 1/2)$, creates a mixture of $J = 3/2$ and $J = 1/2$. Subsequent Rarita-Schiwnger projection [64], shown in Eq. (3.11), makes it possible to isolate the $J = 3/2$ component. The construction of the Δ vector-spinor start from the interpolator,

$$\psi_j^\mu = \epsilon_{abc} u_\mu^a (u^{bT} C\gamma_j u^c) \tag{3.8}$$

where, from the isospin symmetry, is considered the quark content of the Δ^{++} (uuu). The quantization conditions for the vector-spinor field ψ

$$p \cdot \psi(p) = 0 \tag{3.9}$$

$$\not{\psi} = 0 \tag{3.10}$$

together with the Rarita-Schwinger projection on the spin-3/2 components,

$$P_{\mu\nu}^{3/2} = \delta_{\mu\nu} - \frac{1}{3}\gamma_\mu\gamma_\nu - \frac{1}{3p^2}(\gamma \cdot p\gamma_\mu p_\nu + p_\mu\gamma_\nu\gamma \cdot p) \tag{3.11}$$

gives the delta operator,

$$\Delta(p)_k^\alpha = \left(P^{3/2}(p)_{kl}\right)_{\alpha\beta} \psi(p)_l^\beta \tag{3.12}$$

In particular we resort to using two Δ operators with $I_3 = +3/2$:

$$\begin{aligned}
\Delta_{\mu i}^{(1)}(\vec{p}) &= \sum_{\vec{x}} \epsilon_{abc} (u_a(\vec{x}))_\mu (u_b^T(\vec{x}) C\gamma_i u_c(\vec{x})) \, e^{i\vec{p}\cdot\vec{x}}, \\
\Delta_{\mu i}^{(2)}(\vec{p}) &= \sum_{\vec{x}} \epsilon_{abc} (u_a(\vec{x}))_\mu (u_b^T(\vec{x}) C\gamma_i\gamma_0 u_c(\vec{x})) \, e^{i\vec{p}\cdot\vec{x}}.
\end{aligned} \tag{3.13}$$

3.2 Spin on the lattice

To correctly identify the hadrons is essential to tune the operators to the correct quantum numbers of the specifically chosen hadron. In continuum, QCD states are classified according to their angular momentum J and parity P, which labels the irreducible representation (irrep) of the relevant symmetry group, i.e., the improper rotation group $O(3)$. These irreps have both bosonic (single-valued) and fermionic (double-valued) representations [65].

Standard practices for building relativistic operators in the continuum theory involved combining γ matrices, conjugation matrices C, and Dirac spinors to create objects with transformation property of scalars, pseudoscalars, vectors, and pseudovectors. The same technique can be applied to the discrete case of lattice field theory with mostly successful results. Though it is known to be less effective with particles of a higher spin quantum number, often coupling to states of different J^P (spin-parity) [66]. This spin mixing, present only in the finite volume, is due to the hypercube lattice breaking Lorentz covariance. The

rotational symmetry on the lattice is heavily reduced with respect to the infinite-volume. The 24 operations (rotations) that leave the lattice grid unchanged is the octahedral group O. Once the inversion is added as symmetry operation, the group is O_h, which has 48 operations.

Lattice states are classified by irreducible representations Λ, which are a reminiscence of the infinite-volume irreps J^P. In addition, the projection of the angular momentum onto some axis J_z that labels the row of the representation J^P correspond, in the lattice irreps, to the row r of the irreps Λ.

In this study, we are interested in baryons, for which the symmetry group of interest for fermions is the double group, labeled in the following as superscript "D" as in, e.g., O_h^D [67]. Double groups (also called *double cover*) extend the number of elements of the original group introducing an additional element $\bar{E}$, i.e., a 2π rotation, to have a proper one-to-one mapping with a spinorial group, e.g., $SU(2)$ [68].

The mapping between infinite- and finite-volume is from an infinite to a finite amount of irreps. Therefore there is no one-to-one mapping, but rather each lattice irrep Λ contains many states from different continuum irreps. This state's mix makes proper spin identification a challenging task where different spins belonging to the same irrep are virtually indistinguishable from one another.

Additionally, considering only the $N\pi$ system in the rest frame results in a rather sparse energy spectrum. To increase the energy points available to constrain the phase shift fit we consider also moving frames [69, 70] on the same ensemble, where the Lorentz boost contracts the box, resulting in different effective values of the spatial length along the boost direction. Unfortunately, states mix in the irreps belonging to moving frames is enhanced due to the reduced symmetry of boosted frames.

To build operators that transform according to the group (reduced) symmetry of the lattice, there exist various techniques [71]: the projection method, the helicity method, and the partial wave method. Given the simplicity and broader usage among other studies on the subject, we choose to implement the projection method. In particular, we align to the implementation of the projection method used in [66] and [46], using the same naming convention of groups, irreps, and elements of the groups (rotation and inversion).

3.2.1 Spin-J rotations matrices

This section outlines the rotation matrices employed to transform the operators according to their spin J (for a broader introduction, see e.g., [72]). In general, for a specific axis of rotation $\vec{n}$ and angle of rotation ω around this axis, the rotation matrices $U^J(w, \vec{n})$ are,

$$U_{M,M'}^J(w, \vec{n}) = \langle J, M | exp(-i\omega\vec{n} \cdot \vec{J}) | J, M' \rangle \tag{3.14}$$

where is assumed $|\vec{n}| = 1$.

More specifically, for each spin J employed in the projection method, we present below the generators used to build the rotation matrices.

SU(2), J = 1/2

The generators for $SU(2)$ $J = 1/2$ rotations slightly differ depending on the choice of gamma matrices (we use the DeGrand-Rossi matrices shown in App. A). They are given by,

$$(\vec{J}^{1/2})_j = \frac{1}{8j}\epsilon_{jkl}[\gamma_k, \gamma_l], \quad j, k, l \in [x, y, z] \tag{3.15}$$

and the exponentiation of Eq. (3.15) gives the proper rotation matrices. In addition, the reflection (inversion) for a spinor is given by $I = \gamma_t$.

SU(2), J = 1

The reflection transformation is given by $I = -\mathbb{1}_3$

Cartesian basis   The generators for $SU(2)$ $J = 1$ in the cartesian basis are

$$J_x^1 = \begin{pmatrix} 0 & 0 & 0 \\ 0 & 0 & -i \\ 0 & i & 0 \end{pmatrix} \tag{3.16}$$

$$J_y^1 = \begin{pmatrix} 0 & 0 & i \\ 0 & 0 & 0 \\ -i & 0 & 0 \end{pmatrix} \tag{3.17}$$

$$J_z^1 = \begin{pmatrix} 0 & -i & 0 \\ i & 0 & 0 \\ 0 & 0 & 0 \end{pmatrix} \tag{3.18}$$

The rotation for the cartesian basis for angle ω around the axis $\vec{n}$ are given by

$$(R_i)_{\alpha\beta} = \cos(w_i)\delta_{\alpha\beta} + (1 - \cos(w_i))n_\alpha^{(i)}n_\beta^{(i)} - \sin(w_i)\epsilon_{\alpha\beta\gamma}n_\gamma^{(i)}, \quad \alpha\beta\gamma = x, y, z \tag{3.19}$$

or from the exponentiation of the generator in Eq. (3.16)

$$R_{\vec{n},w_i} = \exp(-i\vec{n}\cdot\vec{J}_i^1 w_i), \quad i = x, y, z \tag{3.20}$$

These are the rotations applied to the 3-momentum vector $\vec{p} = (p_x, p_y, p_z)$ and to the operator $\Delta_i = (\Delta_x, \Delta_y, \Delta_z)$

Spherical basis   Alternatively, it is also possbile to use the spherical basis. In this case one start from the *spherical basis* $\left(-(\Delta_x - i\Delta_y)/\sqrt{2}, \Delta_z, (\Delta_x + i\Delta_y)/\sqrt{2}\right)$. The transformation to spherical basis coordinates is given by

$$\begin{pmatrix} v^{+1} \\ v^0 \\ v^{-1} \end{pmatrix} = U \begin{pmatrix} v^x \\ v^y \\ v^z \end{pmatrix} \tag{3.21}$$

$$U = \begin{pmatrix} -\frac{1}{\sqrt{2}} & \frac{i}{\sqrt{2}} & 0 \\ 0 & 0 & 1 \\ \frac{1}{\sqrt{2}} & \frac{i}{\sqrt{2}} & 0 \end{pmatrix} \tag{3.22}$$

The generators for $SU(2)$ $J = 1$ in the spherical basis are

$$\mathcal{J}_x^1 = \frac{1}{\sqrt{2}} \begin{pmatrix} 0 & 1 & 0 \\ 1 & 0 & 1 \\ 0 & 1 & 0 \end{pmatrix} \tag{3.23}$$

$$\mathcal{J}_y^1 = \frac{i}{\sqrt{2}} \begin{pmatrix} 0 & -1 & 0 \\ 1 & 0 & -1 \\ 0 & 1 & 0 \end{pmatrix} \tag{3.24}$$

$$\mathcal{J}_z^1 = \begin{pmatrix} 1 & 0 & 0 \\ 0 & 0 & 0 \\ 0 & 0 & -1 \end{pmatrix} \tag{3.25}$$

SU(2), J = 3/2

For the spin $J = 3/2$ the generators are,

$$J_x^{\frac{3}{2}} = \begin{pmatrix} 0 & \frac{\sqrt{3}}{2} & 0 & 0 \\ \frac{\sqrt{3}}{2} & 0 & 1 & 0 \\ 0 & 1 & 0 & \frac{\sqrt{3}}{2} \\ 0 & 0 & \frac{\sqrt{3}}{2} & 0 \end{pmatrix} \tag{3.26}$$

$$J_y^{\frac{3}{2}} = i \begin{pmatrix} 0 & -\frac{\sqrt{3}}{2} & 0 & 0 \\ \frac{\sqrt{3}}{2} & 0 & -1 & 0 \\ 0 & 1 & 0 & -\frac{\sqrt{3}}{2} \\ 0 & 0 & \frac{\sqrt{3}}{2} & 0 \end{pmatrix} \tag{3.27}$$

$$J_z^{\frac{3}{2}} = \begin{pmatrix} \frac{3}{2} & 0 & 0 & 0 \\ 0 & \frac{1}{2} & 0 & 0 \\ 0 & 0 & -\frac{1}{2} & 0 \\ 0 & 0 & 0 & -\frac{3}{2} \end{pmatrix} \tag{3.28}$$

3.2.2 Matrix elements of irreducible representations

The construction of matrices of irreducible representation in the double group O_h^D (rest frame) can be found in [73, 74]. The formulas for the half-integer matrices belonging to irreps 2-dim. G_1, G_2, and 4-dim H are:

$$G_1: \ (R_i)_{\alpha\beta} = \exp\left(-\frac{i}{2} \vec{n}^{(i)} \vec{\sigma} \omega_i\right)_{\alpha\beta} = \delta_{\alpha\beta} \cos\frac{\omega_i}{2} - i\vec{n}^{(i)} \vec{\sigma}_{\alpha\beta} \sin\frac{\omega_i}{2}$$

Λ	$\Gamma^\Lambda(C_{4y})$	$\Gamma^\Lambda(C_{4z})$
A_{1u}	$[1]$	$[1]$
G_{1g}	$\frac{1}{\sqrt{2}}\begin{bmatrix} 1 & -1 \\ 1 & 1 \end{bmatrix}$	$\frac{1}{\sqrt{2}}\begin{bmatrix} 1-i & 0 \\ 0 & 1+i \end{bmatrix}$
G_{2g}	$\frac{-1}{\sqrt{2}}\begin{bmatrix} 1 & -1 \\ 1 & 1 \end{bmatrix}$	$-\frac{1}{\sqrt{2}}\begin{bmatrix} 1-i & 0 \\ 0 & 1+i \end{bmatrix}$
H_g	$\frac{1}{2\sqrt{2}}\begin{bmatrix} 1 & -\sqrt{3} & \sqrt{3} & -1 \\ \sqrt{3} & -1 & -1 & \sqrt{3} \\ \sqrt{3} & 1 & -1 & -\sqrt{3} \\ 1 & \sqrt{3} & \sqrt{3} & 1 \end{bmatrix}$	$\frac{1}{\sqrt{2}}\begin{bmatrix} -1-i & 0 & 0 & 0 \\ 0 & 1-i & 0 & 0 \\ 0 & 0 & 1+i & 0 \\ 0 & 0 & 0 & -1+i \end{bmatrix}$

Table 3.2 Representation matrices taken from [46] of two transformation elements for irreps belonging to group $O_h^{(D)}$. All other group elements can be obtained from proper compositions of these two elements and the element for space inversion I_s. $\Gamma^\Lambda(I_s)$ is the identity matrix for the even-parity irreps (subscript g, meaning *gerade*) and minus times the identity matrix for the odd-parity ones (subscript u, meaning *ungerade*).

G_2: the matrices are like G_1 except change the sign in the conjugacy classes $6C_8$ (six $\pm\pi/2$ rotations about three coordinate axis, e.g., $\vec{n} = (n_x, n_y, n_z) = (1,0,0)$), $6C_8'$ (six $\pm 3\pi/2$ rotations about three coordinate axis), and $12C_4'$ (twelve $\pm\pi$ rotations about axes parallel to six face diagonals, e.g., $\vec{n} = (1,1,0)$) (see Tab. 4 in [73]).

H: the matrices $(R_i)_{\alpha\beta} = \exp\left(-i\vec{n}^{(i)}\vec{J}^{\frac{3}{2}}\omega_i\right)_{\alpha\beta}$ where $\vec{J}^{\frac{3}{2}}_{\alpha\beta}$ denote the group generators in spin-$3/2$ case.

The vector $\vec{n}^{(i)}$ of the rotation axis and the rotation angles w_i for all 48 rotation elements of the double cover are listed in Tab. 4 of ref. [73]. When using the DeGrand-Rossi gamma matrix basis the generators for irrep H are modified in $\vec{J}^{\frac{3}{2}} \to U^\dagger \vec{J}^{\frac{3}{2}} U$, with $U = \gamma_2$.

This work follows the prescription in [46], where we compute two rotation elements of each irrep and the spatial inversion, and then use them as generators to provide all other group elements. In App. B.2 are presented the rotations elements belonging to each group, along with the combinations used to construct each element for two initial rotations. In the case of irreps in the group O_h^D the matrices of two elements are presented in Tab. 3.2. The elements of the irreps belonging to moving frames can be obtained from the ones in the rest frame through subduction (see Tab. 3.4), which means, to identify the subgroup of rotation elements (allowed on the lattice) that leaves the boosted frame momentum vector unchanged.

For the representation matrices Γ^Λ, it also holds the great orthogonality theorem [67],

$$\sum_{R\in G} \Gamma^\Lambda_{mn}(R)\Gamma^{\Lambda'*}_{m'n'}(R) = \frac{g_G}{\sqrt{d_\Lambda d_{\Lambda'}}}\delta_{\Lambda\Lambda'}\delta_{mm'}\delta_{nn'} \tag{3.29}$$

$Irr \backslash J$	$J=1/2$	$J=3/2$	$J=5/2$	$J=7/2$	$J=9/2$
$G_{1g/u}$	1	0	0	1	1
$G_{2g/u}$	0	0	1	1	0
$H_{g/u}$	0	1	1	1	2

Table 3.3 Subduction of half-integer J irreps of $SU(2)$ in lattice irreps of group O_h^D (rest frame). Also, spin-content and occurrences of irreps.

where d_Λ is the dimension of the irrep Λ, and g_G is the number of elements in the group, equal among irreps of the same group. It states the orthogonality between different irreps and different rows.

3.3   Projection method

The projection method is a known technique to construct an operator that transforms according to a specific symmetry group [71]. Two cases are presented: the single and two-hadron operators, both necessary for a complete determination of the resonance properties [29].

3.3.1   Single operator

The projection method for a single operator in a specific irrep Λ, row r, and embedding i, is given by the formula [71, 46]

$$O^{\Lambda,r,i}(\vec{p}) = \frac{d_\Lambda}{g_{G^D}} \sum_{\tilde{R} \in G^D} \Gamma_{r,r}^\Lambda(\tilde{R}) W(\tilde{R})^{-1} O(\vec{p}) \quad r \in \{1,\dots,dim(\Gamma^\Lambda)\} \tag{3.30}$$

where Γ^Λ are the representation matrices of the elements $\tilde{R}$ (rotations and inversion) of the double group G^D and $O(\vec{p})$ is an unprojected operator (e.g., the ones presented in the sections above). The index i labels the embedding into the irrep and replaces any free Dirac/Lorentz indices appearing on the r.h.s. of Eq. (3.30). The transformation matrices $W(\tilde{R})^{-1}$ correspond to the matrices in the right-hand sides of Eq. (3.37) for the delta, and Eq. (3.38) for pion and nucleon. Additionally, d_Λ is the dimension of the irrep Λ and g_{G^D} is the order, i.e., the number of elements in the group G^D. Examples of representation matrices of irreps belonging to the double group O_h^D are given in Tab. 3.2. Due to the trivial scalar transformations of the pion, the projection does not affect its form.

In general, the choice of 3-momenta $\vec{p}$ establishes the relevant symmetry of the lattice and the double group G^D associated. One can then project the operator $O(\vec{p})$ to a specific irrep Λ from the same group. Looking at Tab. 3.3, the angular momentum J of our state of interest can give us some hint on which irrep it belongs. However, to have a complete identification that takes into account also possible multiplicities, we deduce them from the characters χ (i.e. the trace) of the transformation matrices W_{ij}.

$\Lambda(O_h^D)$	$\downarrow C_{4v}^D$	$\downarrow C_{2v}^D$	$\downarrow C_{3v}^D$
$G_{1g/u}$	G_1	G	G
$G_{2g/u}$	G_2	G	G
$H_{g/u}$	$G_1 \oplus G_2$	$2G$	$F1 \oplus F2 \oplus G$

Table 3.4 Subduction of the relevant irrep of double group O_h^D in little groups of moving frames.

Multiplicity

It is possible to find the multiplicity/occurrence m of the irrep Λ using the formula [67, 74],

$$m_\Lambda = \frac{1}{g_{G^D}} \sum_{\tilde{R} \in G^D} \chi^{\Gamma^\Lambda}(\tilde{R}) \chi^W(\tilde{R}) \tag{3.31}$$

where $\chi^{\Gamma^\Lambda}(\tilde{R})$ and $\chi^W(\tilde{R})$ represent respectively the trace of the representation matrix Γ of the irrep Λ and the trace of the transformation matrix W, both for elements $\tilde{R}$ (rotation+inversion) of the group G^D. The sum is then normalized of the number of elements of the group g_{G^D}.

The procedure to find the multiplicity can be either done for the irreps of the group O_h^D and then subduced to the moving frames irreps (see Tab. 3.4), or apply Eq. (3.31) individually to each irrep of each group. The identification we obtain for the nucleon and pion on each frame is given in Tab. 3.5, while the same for the delta can be found in Tab. 3.6.

In other words, Eq. (3.31) not only tells us which irrep occurs in each frame but also how many times. In fact, in our work, there are many cases with multiple occurrences, e.g., the moving frames of the nucleon. The multiplicity is reflected in the number of independent operators we obtain for a given momentum $\vec{p}$, irrep Λ, and row r. In Fig. 3.1 and Fig. 3.2 are shown the tensor decomposition of the transformation matrix for the nucleon and delta in various relevant group and irreps. In the rest frame, irreps occur only once and are distinct in parity. The situation changes in the moving frames where the loss of parity and reduction of symmetry shifts the situation to fewer irreps and, consequently, increases their occurrences. The most extreme case is in Fig. 3.2 for the delta in the group C_{2v}^D, where the reduced symmetry leaves only one irrep, i.e. G, which manifests six occurrences.

Projection matrix

Practically, the projection formula in Eq. (3.30) produces a list of projected operators (labeled by index i) that may exceed the multiplicity m_Λ, which means that the operators are not guaranteed to be linearly independent. To extract then the minimal set of independent operators, we implement a procedure that uses Gaussian elimination to filter the projected operators of unnecessary not-independent operators. We use an alternative version of the projection formula in Eq. (3.30) from [66], where we build the projection matrix P_{ij} for an

irrep Λ and row r defined as

$$P_{ij}^{\Lambda,r} = \frac{d_\Lambda}{g_{G^D}} \sum_{\tilde{R} \in G^D} \Gamma_{r,r}^\Lambda(R) W_{ij}(R) \tag{3.32}$$

where the matrices W_{ij} represent the transformation matrices for the considered operator $\mathcal{O}$. Then we apply the Gaussian elimination (instead of the Grand-Schmidt procedure of [66]) on P_{ij} to obtain the smaller coefficient matrix c_{nj} (where $n \leq i$) that express the final projected operators with respect to the original set of operators as,

$$\mathcal{O}_n^{\Lambda,r}(\vec{p}) = \sum_j c_{nj}^{\Lambda,r} \mathcal{O}(\vec{p}) \tag{3.33}$$

This procedure guarantees that we obtain a basis of linearly independent operators with a rank equal to the multiplicity m_Λ.

Nucleon operator projection
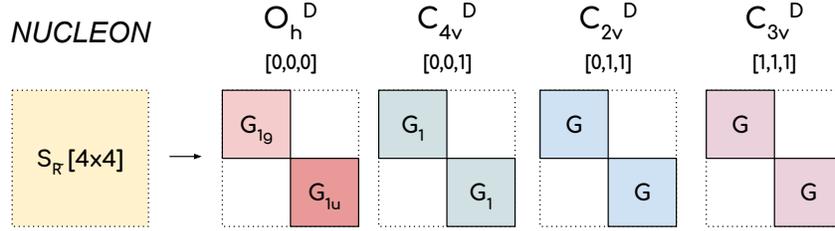
Figure 3.1 Tensor decomposition of the nucleon transformation matrix S (see Eq. (3.34)) for element $\tilde{R}$ in the four groups studied (one rest frame and three moving frames).

The rotations for $SU(2)$ in $J = 1/2$ in our bi-spinor representation is given by:

$$S(C_{nj}) = \exp\left(\frac{1}{8}\omega_{\mu\nu}\left[\gamma_\mu, \gamma_\nu\right]\right) \tag{3.34}$$

where C_{nj} represents a rotation of angle $2\pi/n$ around the axis j (with the antisymmetric tensor $\omega_{kl} = -2\pi\epsilon_{jkl}/n$ and $\omega_{4k} = \omega_{k4} = 0$) [46]. The spatial inversion I_s is given by

$$S(I_s) = \gamma_4(= \gamma_t) \tag{3.35}$$

The actual form of the transformation matrices depends on the choice of the Euclidean γ-matrices. We set on the DeGran-Rossi basis listed in App. A.

P_{ref}	$N_{direction}$	Group	$N_{elements}$	Irrep(dim): nucleon	Irrep(dim): pion
$(0,0,0)$	1	O_h^D	96	$G_{1g}(2)$	$A_{1u}(1)$
$(0,0,1)$	6	C_{4v}^D	16	$2G_1(2)$	$A_2(1)$
$(0,1,1)$	12	C_{2v}^D	8	$2G(2)$	$A_2(1)$
$(1,1,1)$	8	C_{3v}^D	12	$2G(2)$	$A_2(1)$

Table 3.5 General info for each frame of nucleon ($J^P = 1/2^+$) and pion ($J^P = 0^-$)

P_{ref}	$N_{direction}$	Group	$N_{elements}$	Irrep(dim): delta
$(0,0,0)$	1	O_h^D	96	$H_g(4)$
$(0,0,1)$	6	C_{4v}^D	16	$2G_1(2) \oplus 2G_2(2)$
$(0,1,1)$	12	C_{2v}^D	8	$4G(2)$
$(1,1,1)$	8	C_{3v}^D	12	$2G(2) \oplus 2F_1(1) \oplus 2F_2(1)$

Table 3.6 General info for each frame of the delta ($J^P = 3/2^+$)

The projection formula in Eq. (3.30) can be rewritten for the case of the nucleon operator with explicit Dirac indices and the proper transformation matrices $S(\tilde{R})$ as:

$$N_\alpha^{\Lambda,r}(\vec{p}) = \frac{d_\Lambda}{g_{G^D}} \sum_{\tilde{R}\in G^D} \Gamma_{r,r}^\Lambda(\tilde{R}) S(\tilde{R})_{\alpha\beta}^{-1} N_\beta(\vec{p}) \tag{3.36}$$

As expected, looking at column 4 in Tab. 3.5 (or Fig. 3.1), for the case of nucleon for each irrep (and row) we get one single operator in the rest frame (irrep G_{1g} and G_{1u}). The double occurrence for irreps G_1 and G produces two independent operators per row in the moving frames. This comes from the fact that a clear parity identification is lost in the moving frames, and the subduction mixes the parity in the same irrep. Parity is indeed a good quantum number only in the rest frame. An explicit list of projected nucleon operators can be found in Tab. B.9 in the Appendix.

Delta operator projection

The rotations and inversion operation for the vector-spinor delta operators follow

$$\mathsf{R}\Delta_{\alpha k}(\vec{p})\mathsf{R}^{-1} = A(R)_{kk'}^{-1} S(R)_{\alpha\beta}^{-1}\Delta_{\beta k'}(R\vec{p}), \quad \mathsf{I}\Delta_{\alpha k}(\vec{p})\mathsf{I}^{-1} = (\gamma_t)_{\alpha\beta}\Delta_{\beta k}(\vec{p}) \tag{3.37}$$

where $A(R)$ denotes the 3-dim $J = 1$ irrep of $SU(2)$ from Eq. (3.19) and $S(R)$ is given in Eq. (3.34).

The number of projected operators obtained for the delta in each irrep match the irreps listing of Fig. 3.2. Respectively we obtain one for H_g, four in G_1, two in G_2, six in G for the group C_{2v}^D, and for group C_{3v}^D four in G and one in both F_1 and F_2.
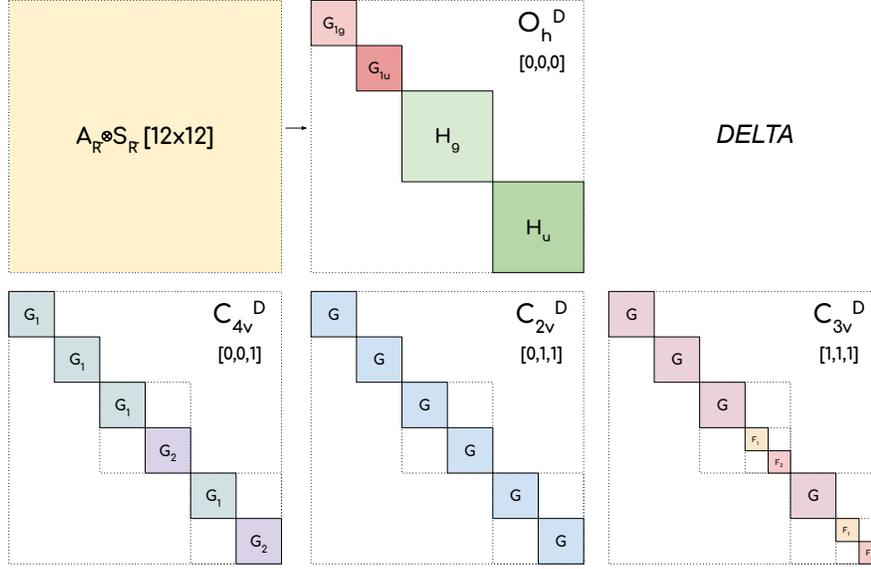
Figure 3.2 Tensor decomposition of the delta transformation matrices $A_{\tilde{R}} \otimes S_{\tilde{R}}$ (see refeqdeltatransformation) in the four groups studied. The diagonal order among which the irreps are shown and the dashed frame is a visual aid meant only to underline the irrep's subduction from the rest frame's irrep (as also listed in Tab. 3.4).

3.3.2 Two-hadron operator

The two-hadron operator composed of nucleon and pion also needs to be projected in the correct angular momentum state J. A more careful approach is needed when applying the projection method formula of Eq. (3.30). The pion requires the transformation properties of a pseudo-scalar particle, while the nucleon (Sec. 3.1.2) transforms as a Dirac bispinor.

The transformations of annihilation fields π, N in momentum space are

$$\mathsf{R}\pi(\vec{p})\mathsf{R}^{-1} = \pi(R\vec{p}), \quad \mathsf{I}\pi(\vec{p})\mathsf{I}^{-1} = -\pi(-\vec{p}) \tag{3.38}$$

$$\mathsf{R}N_\mu(\vec{p})\mathsf{R}^{-1} = \exp\left(\frac{1}{8}\omega_{\mu\nu}\left[\gamma_\mu, \gamma_\nu\right]\right) N_\mu(R\vec{p}), \quad \mathsf{I}N_\mu(\vec{p})\mathsf{I}^{-1} = \gamma_t N_\mu(-\vec{p})$$

with $\omega_{kl} = -2\pi\epsilon_{jkl}/n$ and $\omega_{4k} = \omega_{k4} = 0$.

$N\pi$ operator projection

In the case of the multi-hadron operator $O_{N\pi}$ we project using the formula:

$$O_{N\pi}^{\Lambda,r,i}(\vec{P}) = \frac{d_\Lambda}{g_{G^D}} \sum_{\tilde{R} \in G^D} \sum_{\vec{p}} \Gamma_{r,r}^\Lambda(\tilde{R}) W_N(\tilde{R})^{-1} N(\tilde{R}\vec{p}) W_\pi(\tilde{R})^{-1} \pi(\vec{P} - \tilde{R}\vec{p}) \tag{3.39}$$

where the projected operator is given for an irrep Λ, row r of the irrep, and embedding/occurrence i. The transformation matrices W_N and W_π are shown in the r.h.s. of

Eq. (3.38) for both nucleon and pion. As we have done for the single operator, we use the Gaussian elimination method to extract the minimal subset of independent operators from the result of Eq. (3.39). The result of the orthogonalization process produces a minimal set of independent operators. The number of operators in the final set matches the multiplicity of the irrep Λ given by Eq. (3.31).

For each moving frame, multiple momentum directions of $\vec{P}$ with equal $|\vec{P}|$ are used to increase statistics. In a similar fashion used in [46], we choose a reference momentum P_{ref} in each moving frame, and for each equivalent momentum direction, we define a reference rotation that connects the initial reference momentum to the new one. The lists of representation matrices Γ^{Λ} are defined only for the reference momentum direction.

The operators projected in the reference momentum P_{ref} are then rotated to a new direction using transformation matrices of the reference rotations (shown in Tab. B.1). The transformation matrices are shown in Eq. (3.38) for the $N\pi$ system and Eq. (3.37) for the Delta.

An equal procedure to build operators belonging to the same irrep Λ but with different directions of $\vec{P}$ would be to rotate the transformation matrices $A(R)$ and $S(R)$ in Eq. (3.38) and Eq. (3.37) while keeping the representation matrices unchanged. Even though this procedure would ensure to obtain the same list of operators, it would not guarantee that the operators obtained after the Gaussian elimination procedure would match the order of the operators from another direction. In practical terms, this means that when later on, during the computation of the correlation matrices of projected operators, averaging over matrices from different momentum directions would require assessing the correspondence among operators of different correlation matrices. Given the unnecessary additional uncertainty, we choose to produce operators of different momentum directions from operators produced in the reference momentum P_{ref} with a simple rotation.

For the same reason, we also implement the procedure from [66, 75] to generate operators belonging to a certain row $r > 1$ from the one generated in the first row ($r = 1$) using:

$$O^{\Lambda,r,n}(\vec{p}) = \sum_j c_{ij}^{\Lambda,1} \frac{d_\lambda}{g_{G^D}} \sum_{\tilde{R} \in G^D} \Gamma_{r,1}^{\Lambda}(\tilde{R}) \mathsf{R} O(\vec{p}) \mathsf{R}^{-1} \qquad (3.40)$$

where c_{ij} is the coefficient matrix defined in Eq. (3.33) and the rotation/inversion $\mathsf{R}O(\vec{p})\mathsf{R}^{-1}$ are performed as in Eq. (3.30) and Eq. (3.39) depending on the structure of $O(\vec{p})$. This step guarantees that projected operators that belong to different rows produce an equivalent set, enabling the averaging correlation matrices over rows, removing the risk of summing different quantities [76].

We restrict the momentum content for the nucleon and pion to the elastic region (and slightly above). As a general rule, we limit the momenta content of the multi hadron operators to $|\vec{p}_N|^2 + |\vec{p}_\pi|^2 \leq 3(\frac{2\pi}{L})^2$. This limits the range of operators to consider: the ones lying between the $N\pi$ and $N\pi\pi$ thresholds and the first few levels above it (this cut limits the numbers of operators to be computed to the list outlined in Tab. B.1). A complete list of operators used for the $\Delta - N\pi$ correlators can be found in Tab. 3.7. As an example from this list, for the rest frame (group O_h^D) we limit the momentum content for nucleon and pion operator in the multihadron $N\pi$ to a maximum of one unit of momentum each. From the
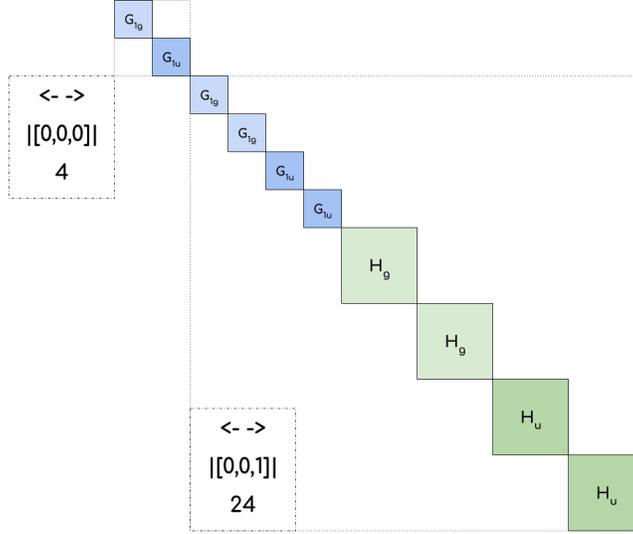
Figure 3.3 Tensor decomposition of the $N\pi$ system transformation matrices for $\vec{P}_{tot} = \vec{p}_\pi + \vec{p}_N = 0$. Listed is the absolute value of the back-to-back momentum for the two hadrons; for which $|\vec{p}_\pi| = |\vec{p}_N|$.

tensor decomposition shown in Fig. 3.3 is visible that if we project onto the irrep H_g, we obtain two independent operators per row, i.e. multiplicity $m = 2$, both with momentum $\vec{p}_\pi = -\vec{p}_N = \frac{2\pi}{L}(0, 0, 1)$ (and permutations). On the other hand, the case where the pion and the nucleon are simultaneously at rest belongs only to irreps G_{1g} and G_{1u}.

$\frac{L}{2\pi}\vec{P}_{ref}$ $[N_{dir}]$	Group	Irrep Λ (Rows)	Ang. mom. content	Operator structure	Mult.
(0,0,0) [1]	O_h^D	G_{1u} (2)	$J = 1/2, 7/2, ...$	$N\pi$ with $|\vec{p_1}| = |\vec{p_2}| = 0$	1
				$N\pi$ with $|\vec{p_1}| = |\vec{p_2}| = \frac{2\pi}{L}$	2
		H_g (4)	$J = 3/2, 5/2, ...$	$\Delta^{(1,2)}(\vec{P})$	1
				$N\pi$ with $|\vec{p_1}| = |\vec{p_2}| = \frac{2\pi}{L}$	2
(0,0,1) [3]	C_{4v}^D	G_1 (2)	$J = 1/2, 3/2, ...$	$\Delta^{(1,2)}(\vec{P})$	4
				$N\pi$ with $|\vec{p_1}| = 0$ and $|\vec{p_2}| = \frac{2\pi}{L}$	2
				$N\pi$ with $|\vec{p_1}| = \frac{2\pi}{L}$ and $|\vec{p_2}| = 0$	2
				$N\pi$ with $|\vec{p_1}| = \frac{2\pi}{L}$ and $|\vec{p_2}| = \sqrt{2}\frac{2\pi}{L}$	4
				$N\pi$ with $|\vec{p_1}| = \sqrt{2}\frac{2\pi}{L}$ and $|\vec{p_2}| = \frac{2\pi}{L}$	4
		G_2 (2)	$J = 3/2, 5/2, ...$	$\Delta^{(1,2)}(\vec{P})$	2
				$N\pi$ with $|\vec{p_1}| = \sqrt{2}\frac{2\pi}{L}$ and $|\vec{p_2}| = \frac{2\pi}{L}$	4
				$N\pi$ with $|\vec{p_1}| = \frac{2\pi}{L}$ and $|\vec{p_2}| = \sqrt{2}\frac{2\pi}{L}$	4
(0,1,1) [6]	C_{2v}^D	$(2)G$ (2)	$J = 1/2, 3/2, ...$	$\Delta^{(1,2)}(\vec{P})$	6
				$N\pi$ with $|\vec{p_1}| = 0$ and $|\vec{p_2}| = \sqrt{2}\frac{2\pi}{L}$	2
				$N\pi$ with $|\vec{p_1}| = \sqrt{2}\frac{2\pi}{L}$ and $|\vec{p_2}| = 0$	2
				$N\pi$ with $|\vec{p_1}| = |\vec{p_2}| = \frac{2\pi}{L}$	4
(1,1,1) [4]	C_{3v}^D	G (2)	$J = 1/2, 3/2, ...$	$\Delta^{(1,2)}(\vec{P})$	4
				$N\pi$ with $|\vec{p_1}| = 0$ and $|\vec{p_2}| = \sqrt{3}\frac{2\pi}{L}$	2
				$N\pi$ with $|\vec{p_1}| = \sqrt{3}\frac{2\pi}{L}$ and $|\vec{p_2}| = 0$	2
				$N\pi$ with $|\vec{p_1}| = \frac{2\pi}{L}$ and $|\vec{p_2}| = \sqrt{2}\frac{2\pi}{L}$	4
				$N\pi$ with $|\vec{p_1}| = \sqrt{2}\frac{2\pi}{L}$ and $|\vec{p_2}| = \frac{2\pi}{L}$	4
		$F_1(1)/$ $F_2(1)$	$J = 3/2, 5/2, ...$	$\Delta^{(1,2)}(\vec{P})$	2
				$N\pi$ with $|\vec{p_1}| = \frac{2\pi}{L}$ and $|\vec{p_2}| = \sqrt{2}\frac{2\pi}{L}$	2
				$N\pi$ with $|\vec{p_1}| = \sqrt{2}\frac{2\pi}{L}$ and $|\vec{p_2}| = \frac{2\pi}{L}$	2

Table 3.7 List of projected operators for the single-hadron Δ and multi-hadrons $N\pi$ for all irreps with multiplicity associated.

Chapter Four

Quantization condition

The task of extracting properties of unstable particles on the lattice is particularly challenging: resonances do not directly associate to a single energy level of the lattice Hamiltonian. Due to the use of Euclidean time, it is not possible to extract infinite-volume scattering amplitudes directly [77].

Nevertheless, work by Lüscher [78] made it possible to compute scattering amplitudes of elastic scattering from the lattice spectra, exploiting the shift in energy between the non-interacting energies and the interacting values. His work was further extended to moving frames by Gottlieb and Rummukainen [69] and Feng et al. [79]. It had been then generalized to two body systems of arbitrary mass by Davoudi and Savage [80], Fu [81], and Leskovec and Prelovsek [82]. These breakthrough in the theoretical aspects, combined with advancement in computing technology, has enabled LQCD calculations of resonance parameters in both the meson and baryon sector; in particular the former [83]. Nonetheless, there remain problems such as partial wave mixing that is worse for particles with unequal masses [82, 70, 83].

A finite volume gives rise to a discretized set of energy levels (which would be a continuum in infinite-volume). The discrete spectra, categorized by different irreps, encapsulate the intrinsic information about the phase shift, for which the Lüscher formulation successfully models the dependence. In our study, when considering the $N\pi$ system in the rest frame, the quantization of momenta $\vec{p} = \frac{2\pi}{L}(n_x, n_y, n_z)$ in a finite volume of size L^3 results in a quite sparse energy spectrum across the elastic region between the $N\pi$ and $N\pi\pi$ thresholds. This leaves a few energy points for the $N\pi$ system available to constrain the phase shift we aim to measure. A straightforward way to gain additional points would be to add a spatially larger ensemble; nevertheless, this is computationally quite expensive. A more inexpensive approach to increase the limited number of energy points available is to resort to non-zero total momentum frames [70], where the Lorentz boost contracts the box, resulting in different effective values of the spatial length L along the momentum directions [82], and thus, different quantized momenta.

4.1   Two particles in a box

Is it instructive to briefly review the work of Lüscher [78]. It laid down the framework that connects the infinite-volume phase shift to the information encapsulated in the energy shift between non-interacting and interacting cases. This section follows the derivations in [70, 82]

4.1.1 Non-Interacting case

Consider a cubic lattice of spatial volume L^3 with periodic boundary conditions. For two non-interacting particles, the single particle's momenta are quantized,

$$\vec{p_1} = \frac{2\pi}{L}\vec{n_1}, \quad \vec{p_2} = \frac{2\pi}{L}\vec{n_2} \quad \vec{n_1}, \vec{n_2} \in \mathbb{Z}^3 \tag{4.1}$$

as well as the total momentum,

$$\vec{P}_{tot} = \vec{p_1} + \vec{p_2} = \frac{2\pi}{L}\vec{d} \quad \vec{d} \in \mathbb{Z}^3 \tag{4.2}$$

The energy of the two particles system in the laboratory frame (L) is then given by,

$$E_L = \sqrt{\vec{p_1}^2 + m_1^2} + \sqrt{\vec{p_2}^2 + m_2^2} \tag{4.3}$$

that can provide the energy levels of the non-interacting case. The spectrum provides useful information (ahead of the computation) on the energy region of interest as it does not differ heavily from the interacting case spectrum [82].
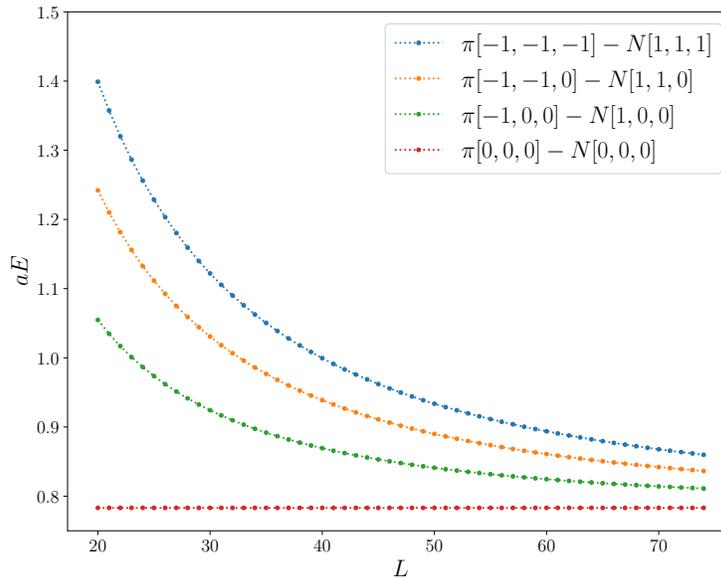
Figure 4.1 Non-interacting energy levels for the $N\pi$ system in the rest frame ($\vec{P}_{tot} = \frac{2\pi}{L}[0,0,0]$) in a finite volume of spatial size L.

Fig. 4.1 and Fig. 4.2 show the non-interacting energies levels for the $N\pi$ system in terms of the box size L, respectively for the rest frame ($\vec{P}_{tot} = \frac{2\pi}{L}[0,0,0]$) and the moving frame of momentum $\vec{P}_{tot} = \frac{2\pi}{L}[0,0,1]$. Clearly, as the box size L increases, the energy levels tend to get closer in energy, as expected in the continuum limit.
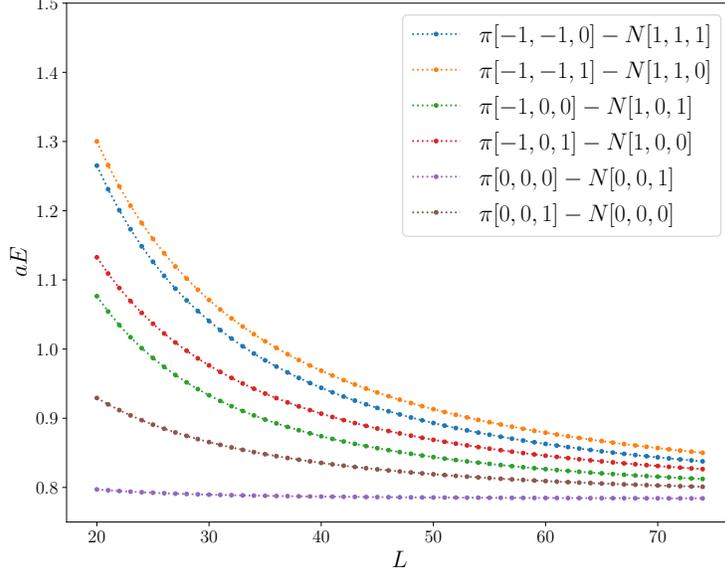
Figure 4.2 Non-interacting energy levels for the $N\pi$ system in a moving frame ($\vec{P}_{tot} = \frac{2\pi}{L}[0,0,1]$) in a finite volume of spatial size L.

The system has a velocity,

$$\vec{v} = \frac{\vec{P}_{tot}}{E} \qquad \gamma = \frac{1}{\sqrt{1-v^2}} \tag{4.4}$$

with respect to the center-of-mass frame (CM). We can write Eq. (4.3) for the center-of-mass frame as

$$E^*_{CM} = \sqrt{\vec{p}_1^{*2} + m_1^2} + \sqrt{\vec{p}_2^{*2} + m_2^2} = \gamma^{-1}E_L \tag{4.5}$$

where we can expressed $\vec{p}^* = \vec{p}_1^* = -\vec{p}_2^*$ in terms of the dimensionless CM momentum $\vec{q}$ via,

$$\vec{p}^* = \frac{2\pi}{L}\vec{q} \quad \text{with} \quad \vec{q} \in P_d = \{\vec{q}|\vec{q} = \gamma^{-1}(\vec{n} - \frac{1}{2}A\vec{d})\} \qquad \vec{n}, \vec{d} \in Z^3 \tag{4.6}$$

where P_d is the set of points (in the space of discrete momenta) that define the mesh arrangement [1], and the quantity A is defined

$$A \equiv 1 + \frac{m_1^2 - m_2^2}{E^{*2}_{CM}} \tag{4.7}$$

which plays a role only when $m_1 \neq m_2$ [82]. This is true in our case as we have different particles scattering: $m_N \neq m_\pi$. The mesh of points P_d, and particularly the symmetries under which they are invariant, define the symmetry group and its transformation elements that enable the creation of operators with a desired angular momentum J.

---

[1]the mesh of points in a rest frame is described by the symmetry group O_h. In a boosted frame the mesh seen by the CMF is distorted, which changes the symmetry group associated.

4.1.2 Interacting case

Following [69, 82, 81], we can now look at the case for interacting particles in a finite volume using relativistic quantum mechanics. In the interacting case, only the total momentum of the system is quantized,

$$\vec{P}_{tot} = \vec{p}_1 + \vec{p}_2 = \frac{2\pi}{L}\vec{d} \quad \vec{d} \in \mathbb{Z}^3 \tag{4.8}$$

where $\vec{p}_1$ and $\vec{p}_2$ are the momenta of the two particles in the laboratory frame.

The energy of the laboratory frame is related to the CM frame by,

$$E_L = \sqrt{\vec{P}_{tot}^2 + E_{CM}^{*2}} \tag{4.9}$$

with

$$E_{CM}^* = \sqrt{\vec{p}^{*2} + m_1^2} + \sqrt{\vec{p}^{*2} + m_2^2} \tag{4.10}$$

where $\vec{p}^* = \vec{p}_1^* = -\vec{p}_2^*$ is called scattering momentum and is the particles' momentum in the CM frame. Thus, the two frames (L and CM) are connected by basic Lorentz transformation,

$$\vec{p}^* = \gamma^{-1}(\vec{p}_1 - \vec{v}\sqrt{\vec{p}_1^2 + m_1^2}) = \gamma^{-1}(\vec{p}_1 - \frac{1}{2}A\vec{P}_{tot}) \tag{4.11}$$

where we define the coefficient A in Eq. (4.7).

The interactive-case energies, in general, are slightly shifted with respect to the non-interacting case. The difference is usually small enough to make use of the non-interactive energies as a qualitative prediction of the spectrum of scattering states and corresponding energy levels that can be expected from the lattice computation. In the interacting case, the resonance's presence alters the energy levels' position, and $\vec{p}^*$ gets different values with respect to the non-interacting case (no more integer values). The difference between these two cases quantifies the interaction between the nucleon and the pion. The phase shift, which encodes the unknown information regarding the interaction, is then extracted from the interacting case's energy shift. Furthermore, in the case of non-zero total momentum, the grid of points of the lattice is distorted in the CMF (through the γ factor in Eq. (4.11)). The initial cubic symmetry group is reduced to a smaller symmetry group, called *Little Group* (LG). With the change in the lattice's symmetry, one then needs to build the interpolators according to the symmetries of the appropriate little group. Also, since each moving frame provides different CMF energies with respect to the rest frame case, one can expect new energy points to improve the constrain of the phase shift fit.

4.1.3 Solutions to the Helmholtz equation

The solution to the Helmholtz equation is the first step to discuss the scattering phases of interacting particle systems [70, 69]. The two-particles system in the laboratory frame is described by the wave function,

$$\psi_L(x_1; x_2) = e^{-iE_L t - \vec{P}\vec{X}}\phi_L(x_0, \vec{x}) \tag{4.12}$$

where

$$\vec{X} = \frac{m_1\vec{x_1} + m_2\vec{x_2}}{m_1 + m_2}, \quad \vec{x} = \vec{x_1} - \vec{x_2} \tag{4.13}$$

$$t = \frac{m_1 x_1^0 + m_2 x_2^0}{m_1 + m_2}, \quad x^0 = x_1^0 - x_2^0 \tag{4.14}$$

and the focus is on the case for both particles with equal time coordinates, $x_1^0 = x_2^0$. The coordinates in the CM frame are labeled as $x^* = (x^{0*}, \vec{x}^*)$. To transform coordinates from the laboratory frame to the center-of-mass frame one can use

$$\begin{pmatrix} x^{0*} \\ \vec{x}^* \end{pmatrix} = \begin{pmatrix} \gamma & \gamma\vec{v} \\ \gamma\vec{v} & \vec{\gamma} \end{pmatrix} \begin{pmatrix} 0 \\ \vec{x} \end{pmatrix}$$

with

$$\phi_L(0, \vec{x}) = \phi_{CM}(x^{0*}, \vec{x}^*) \tag{4.15}$$

Non-interacting case

Following from the Klein-Gordon equation, the wave equation obeys the equation of motion

$$\left(-\nabla_{x^{0*}}^2 + \vec{\nabla}_{x^*}^2 + (E^2 - (m_1 + m_2)^2)\frac{m_1 m_2}{(m_1 + m_2)^2}\right)\phi_{CM}(x^{0*}, \vec{x}^*) = 0 \tag{4.16}$$

with

$$\left(-i\nabla_{x^{0*}} - \frac{E_1 m_2 - E_2 m_1}{m_1 + m_2}\right)\phi_{CM}(x^{0*}, \vec{x}^*) = 0 \tag{4.17}$$

One can factor out the time dependence writing,

$$\phi_{CM}(x^{0*}, \vec{x}^*) = e^{i\frac{E_1 m_2 - E_2 m_1}{m_1 + m_2}x^0}\phi_{CM}(0, \vec{x}^*) \tag{4.18}$$

and thus, obtaining the Helmholtz equation,

$$(\vec{\nabla}_r^2 + \vec{p}^{*2})\phi_{CM}(\vec{x}^*) = 0 \tag{4.19}$$

with $\phi_{CM}(\vec{x}^*) = \phi_{CM}(0, \vec{x}^*)$ and $\vec{p}^*$ given by Eq. (4.6). The laboratory frame wave function has periodicity over spatial translation

$$\psi_L(x_1^0, \vec{x}_1; x_2^0, \vec{x}_2) = \psi_L(x_1^0, \vec{x}_1 + \vec{n}_1 L; x_2^0, \vec{x}_2 + \vec{n}_2 L), \quad \vec{n}_{1,2} \in \mathbb{Z}^3 \tag{4.20}$$

To obtain the equivalent relation for the CM frame, we combine Eq. (4.12), Eq. (4.15) and Eq. (4.18), and get

$$\psi_L(0, \vec{x}_1, 0, \vec{x}_2) = e^{i(\vec{P}\vec{X} + \frac{E_1 m_2 - E_2 m_1}{E(m_1 + m_2)}\vec{P}\vec{x})}\phi_{CM}(\vec{x}^*) \tag{4.21}$$

where we use $x^{0*} = \gamma\vec{v}\vec{x} = \vec{P}\vec{x}/E$. Finally, the periodicity relation for the wave function in the CMF is given by

$$\phi_{CM}(\vec{x}^*) = e^{-i\pi\vec{n}A}\phi_{CM}(\vec{x}^* + \vec{\gamma}\vec{n}L) \tag{4.22}$$

with $\vec{n} = \vec{n}_1 - \vec{n}_2$ and the coefficient A defined in Eq. (4.7). For unequal masses $m_1 \neq m_2$, the wave function picks up a phase $e^{-i\pi\vec{n}A}$ when crossing spatial boundary [70].

Interacting case

When there is an interaction between particles we have a potential $V(\vec{r^*})$ that depends on the relative distance $\vec{x^*} = \vec{x^*_1} - \vec{x^*_2}$. We assume that the interaction is of finite range, and we proceed to consider the wave function in the outer region, where:

$$V(\vec{x^*}) = 0 \quad \text{for} \quad |\vec{x^*}| > R \tag{4.23}$$

with $L \gg 2R$. Outside the region of interaction, $\phi_{CM}(x^*)$ satisfies the Helmholtz equation

$$\left(\vec{\nabla}^2_{x^*} + \vec{p}^{*2}\right) \phi_{CM}(\vec{x^*}) = 0 \tag{4.24}$$

with

$$\vec{p}^{*2} = \frac{(E^2 - (m_1^2 + m_2^2))^2 - 4m_1^2 m_2^2}{4E^2} \tag{4.25}$$

where E are the energies as in Eq. (4.10). The effect of the interior region on the Helmholtz equation solution $\phi_{CM}(x^*)$ is given by the phase shift $\delta_l(p^*)$. The general solution to the Helmholtz equation for a given p^* can be written as linear combinations of the spherical Bessel functions [84] as,

$$\phi_{CM} = \sum_{l,m} c_{lm} Y_{lm}(\theta, \varphi) \left[a_l(p^*) j_l(p^* x^*) + b_l(p^*) n_l(p^* x^*)\right] \tag{4.26}$$

A general definition for the phase shift $\delta_l(p^*)$ is the ratio of the out-going wave $j_l - in_l$ and the in-going wave $j_l + in_l$ [85]

$$e^{2i\delta_l(p^*)} = \frac{a_l(p^*) + ib_l(p^*)}{a_l(p^*) - ib_l(p^*)} \tag{4.27}$$

This definition, usually defined for the continuum, will be used also in the finite volume, even as the wave function can not be expressed anymore in terms of j_l and n_l due to boundary conditions [82]. The boundary condition in Eq. (4.20) imposes $\phi_{CM}(\boldsymbol{x^*})$ to satisfy the $\vec{d}$-periodic boundary condition [81, 82]

$$\phi_{CM}(x^*) = (-1)^{A\vec{n}\cdot\vec{d}} \phi_{CM}(\vec{x^*} + \boldsymbol{\gamma}\vec{n}L) \quad \vec{n} \in \mathbb{Z}^3 \tag{4.28}$$

Satisfying both the Helmholtz equation and the $\vec{d}$-periodic boundary condition is achieved, for example, by the Green function

$$G^{\vec{d}}(\vec{x^*}, p^*) = \gamma^{-1} L^{-3} \sum_{k=\frac{2\pi}{L}\vec{r}, \vec{r}\in P_d} \frac{e^{i\vec{k}\cdot\vec{x^*}}}{\vec{k}^2 - p^{*2}} \tag{4.29}$$

where P_d is the mesh of points defined in Eq. (4.6). Other solutions to the Helmholtz equations (and boundary condition) are the functions [78, 69, 81]

$$G^{\vec{d}}_{lm}(\vec{x^*}, p^*) = \mathcal{Y}_{lm}(\nabla) G^{\vec{d}}(\vec{x^*}, p^*) \tag{4.30}$$

with the harmonic polynomials,

$$\mathcal{Y}_{lm}(\vec{x}) \equiv x^l Y_{lm}(\theta, \varphi) \tag{4.31}$$

The functions $G_{lm}^{\vec{d}}$ form a complete set of solutions and any singular $\vec{d}$-periodic solution of degree Λ is a linear combination of the functions $G_{lm}^{\vec{d}}(\vec{x}^*, p^*)$ with $l \leq \Lambda$ [81, 78]. The solution $\phi_{CM}(x^*)$ can then be rewritten in terms of the functions $G_{lm}^{\vec{d}}$ as

$$\phi_{CM}(x^*) = \sum v_{lm} G_{lm}^{\vec{d}}(\vec{x}^*, p^*) \tag{4.32}$$

Additionally, they can be expanded in terms of the spherical Bessel functions j_l and n_l and spherical harmonics $Y_{lm}(\theta, \varphi)$ [84] as,

$$G_{lm}^{\vec{d}}(\vec{x}^*, p^*) = \frac{(-1)^l (p^*)^{l+1}}{4\pi} \left[n_l(p^* x^*) Y_{lm}(\theta, \varphi) + \sum_{l'=0}^{\infty} \sum_{m'=-l'}^{l'} \mathcal{M}_{lm,l'm'}^{\vec{d}}(q^2) j_{l'}(p^* x^*) Y_{l'm'}(\theta, \varphi) \right] \tag{4.33}$$

where $x^* = |\vec{x}^*|$, and θ, φ are the polar coordinates of $\vec{x}^*$, and $\mathcal{M}_{lm,l'm'}^{\vec{d}}(q^2)$ is given as,

$$\mathcal{M}_{lm,l'm'}^{\vec{d}}(q^2) = \frac{(-1)^l \gamma^{-1}}{\pi^{3/2}} \sum_{j=|l-l'|}^{l+l'} \sum_{s=-j}^{j} \frac{i^j}{q^{j+1}} Z_{js}^{\vec{d}}(1, q^2)^* C_{lm,js,l'm'}, \quad q = \frac{p^* L}{2\pi} \tag{4.34}$$

An important fact is that the matrices $\mathcal{M}_{lm,l'm'}$ are calculable for a given $l, m, l', m', \vec{d}$ and q. The modified zeta function, defined in [80, 81], is

$$Z_{lm}^{\vec{d}}(s; q^2) = \sum_{\vec{r} \in P_d} \frac{\mathcal{Y}_{lm}(\vec{r})}{(\vec{r}^2 - q^2)^s} \tag{4.35}$$

where the summation is over the mesh of points P_d defined in Eq. (4.6). The coefficient $C_{lm,js,l'm'}$ is expressed in terms of Wigner 3j-symbols as

$$C_{lm,js,l'm'} = (-1)^{m'} i^{l-j-l'} \sqrt{(2l+1)(2j+1)(2l'+1)} \begin{pmatrix} l & j & l' \\ m & s & -m' \end{pmatrix} \begin{pmatrix} l & j & l' \\ 0 & 0 & 0 \end{pmatrix} \tag{4.36}$$

Inserting Eq. (4.33) in the exterior solution of Eq. (4.32) provides a general relation, which, once related to Eq. (4.26), provide the phase shift δ_l as is defined in Eq. (4.27),

$$\phi_{CM}(\vec{x}^*) = \sum_{l,m} v_{lm} \frac{(-1)^l (p^*)^{l+1}}{4\pi} \left[n_l(p^* x^*) Y_{lm}(\theta, \varphi) + \sum_{m',l'} \mathcal{M}_{lm,l'm'}^{\vec{d}}(q^2) j_{l'}(p^* x^*) Y_{l'm'}(\theta, \varphi) \right]$$

$$= \sum_{l,m} c_{lm} Y_{lm}(\theta, \varphi) [a_l(p^*) j_l(p^* x^*) + b_l(p^*) n_l(p^* x^*)] \tag{4.37}$$

from which one get the two relations

$$v_{lm} \frac{(-1)^l (p^*)^{l+1}}{4\pi} = c_{lm} b_l(p^*), \quad \sum_{l',m'} v_{l',m'} \frac{(-1)^{l'} (p^*)^{l'+1}}{4\pi} \mathcal{M}_{l'm',lm}(q^2) = c_{lm} a_l(p^*) \tag{4.38}$$

42

Expressing v_{lm} from the first relation and inserting it into the second gives,

$$\sum_{l',m'} c_{l'm'} \left[b_{l'}(p^*) \mathcal{M}_{l'm',lm}(q^2) - a_{l'}(p^*) \delta_{ll'} \delta_{mm'} \right] = 0 \qquad (4.39)$$

for which we have a non-trivial solution for $c_{l'm'}$ only if

$$\det(BM - A) = 0 \qquad (4.40)$$

where $A \equiv a_l(p^*) \delta_{ll'} \delta_{mm'}$ and $B \equiv b_l(p^*) \delta_{ll'} \delta_{mm'}$ are diagonal matrices that connect the phase shift δ_l definition in Eq. (4.27) by

$$e^{2i\delta} = \frac{A + iB}{A - iB} \qquad (4.41)$$

Finally, we divide Eq. (4.40) by the non-zero quantity $\det(A - iB)$, and obtain the determinant condition [78],

$$\det \left[e^{2i\delta_l(p^*)\delta_{ll',mm'}} (\mathcal{M}^{\vec{d}}_{lm,l'm'}(q^2) - i) - (\mathcal{M}^{\vec{d}}_{lm,l'm'}(q^2) + i) \right] = 0 \qquad l, l' \leq l_{max} \qquad (4.42)$$

Also called *quantization condition*, Eq. (4.42) relates the infinite-volume phase shift δ_l and the energies (via $q = p^* L / 2\pi$) measured on the lattice through the calculable matrix $\mathcal{M}^{\vec{d}}_{lm,l'm'}(q^2)$. The information about the phase shift $\delta_l(p^*)$ is concealed in the shift in energy between non-interacting and interacting energies E, and the quantization condition (Eq. (4.42)) provides that connection through CMF momentum p^*. To simplify notation, in the following we proceed to define the function w_{lm} as

$$w_{lm} \equiv \frac{1}{\pi^{3/2} \sqrt{2l+1} \gamma q^{l+1}} Z^{\vec{d}}_{lm}(1; q^2) \qquad (4.43)$$

4.1.4 Particles with spin

Since this is a study of baryon resonances, we proceed to extend to the case of particles carrying half-integer spin as in [70]. In the wave function, one can factor out the spin-dependent part as the spin operator $\hat{S}$ commutes with the Hamiltonian. In the outer region $|\vec{r}| > R$ the wave function solution we have is then,

$$\phi_{CM}(\boldsymbol{x}^*) = \sum_{J,\mu,l,m,\sigma} \langle lm, \tfrac{1}{2}\sigma | J\mu \rangle \, c_{lm} G^{\vec{d}}_{lm}(\boldsymbol{x}^*, q^2) \chi^{\frac{1}{2}}_{\sigma} \qquad (4.44)$$

where $\chi^{\frac{1}{2}}_{\sigma}$ is the baryon two-component spinor. This make for a basis where $\mathcal{M}^{\vec{d}}$ carry quantum numbers J, l, μ and relate to the spin-zero counterpart as

$$\mathcal{M}^{\vec{d}}_{Jl\mu,J'l'\mu'} = \sum_{m,\sigma,m',\sigma'} \langle lm, \tfrac{1}{2}\sigma | J\mu \rangle \langle l'm', \tfrac{1}{2}\sigma' | J'\mu' \rangle \, \mathcal{M}^{\vec{d}}_{lm,l'm'} \qquad (4.45)$$

Following [73], we can modify the Lüscher quantization condition in Eq. (4.42)) to include the spin content with the matrix $\mathcal{M}^{\vec{d}}_{Jl\mu,J'l'\mu'}$ as

$$\det(\mathcal{M}^{\vec{d}}_{Jl\mu,J'l'\mu'} - \delta_{JJ'} \delta_{ll'} \delta_{\mu\mu'} \cot \delta_{Jl}) = 0 \qquad (4.46)$$

43

The interpretation of the above formula goes as follows: given a total momentum $\vec{d}$ and a set of scattering amplitudes δ_{Jl}, in a finite volume $L \times L \times L$, the discrete spectrum of states $E_n(\vec{d}, L)$ is given by the energies for which the determinant equals zero [83].

4.2 Symmetries of the zeta function

In addition to the rest frame, we consider boosted frames that enable gathering additional energy levels to better extrapolate the phase shift δ_{Jl}. Each frame carries different symmetries that translate into different contributions to the zeta function of Eq. (4.35).

For this work, Tab. 4.1 lists the selected frames of momentum $\vec{d}$ (plus equivalent momenta up to a global rotation).

$\vec{d}$ Axis	$[0,0,0]$ $\equiv 0$	$[0,0,1]$ $\equiv \boldsymbol{e}_3$	$[1,1,0]$ $\equiv \boldsymbol{e}_1 + \boldsymbol{e}_2$	$[1,1,1]$ $\equiv \boldsymbol{e}_1 + \boldsymbol{e}_2 + \boldsymbol{e}_3$
Group LG	$O_h^{(D)}$	$C_{4v}^{(D)}$	$C_{2v}^{(D)}$	$C_{3v}^{(D)}$
Axis and planes of symmetry				
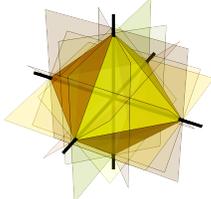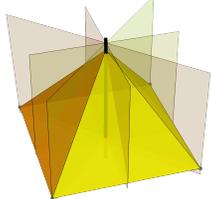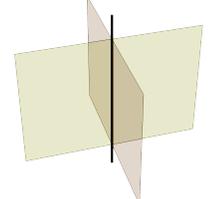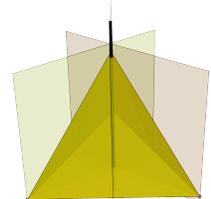
Table 4.1 Choices of total momenta $\vec{d}$ for the frames, along with the symmetry groups LG, and axis and planes of symmetry. Images credit: [86].

We now consider each frame and its symmetries to simplify the function w_{lm} (Eq. (4.43)) and, in turn, the generalized zeta function. In general, the zeta function for unequal masses [70] follows,

$$Z^{\vec{d}}_{l-m}(1; q^2) = (-1)^m Z^{\vec{d}}_{lm}(1; q^2)^* \tag{4.47}$$

plus additional constraints depending on the frame considered. In the following, the relations for moving frames were derived in [70], while for the rest frame they can be found in [78].

Case: $\vec{d} = [0,0,0]$

In the rest frame, there is a symmetry under the exchange of the three axis $1 \leftrightarrow 2 \leftrightarrow 3 \leftrightarrow 1$ and reflection on any axis. These translate in the following properties for the zeta function:

- $Z^{\vec{d}}_{lm}(1; q^2) = 0$ if l is odd

- $Z^{\vec{d}}_{lm}(1; q^2) = Z^{\vec{d}}_{l-m}(1; q^2)$

- $Z^{\vec{d}}_{lm}(1; q^2) = 0$ if m is not a multiple of 4

also,(for $l \leq 4$) the following relations hold

- $Z_{20}^{\vec{d}}(1; q^2) = 0$

- $Z_{44}^{\vec{d}}(1; q^2) = \frac{\sqrt{70}}{14} Z_{40}^{\vec{d}}(1; q^2)$

The w_{lm} (defined in Eq. (4.43)) that are non-zero in the rest frame are,

l	w_{lm}
0	(w_{00})
1	$(0, 0, 0)$
2	$(0, 0, 0, 0, 0)$
3	$(0, 0, 0, 0, 0, 0, 0)$
4	$(\frac{\sqrt{70}}{14} w_{40}, 0, 0, 0, w_{40}, 0, 0, 0, \frac{\sqrt{70}}{14} w_{40})$

Case: $\vec{d} = [0, 0, 1]$

For this boosted frame, there is a symmetry under rotations around $\boldsymbol{e}_3$ by $\pi/2$, which translate to

$$Z_{lm}^{\vec{d}}(1; q^2) = 0, \quad \text{for } m \neq 0 \mod 4 \tag{4.48}$$

as well as interchange of axis $1 \leftrightarrow 2$ and reflection $\boldsymbol{e}_{1,2} \rightarrow -\boldsymbol{e}_{1,2}$.

The non-zero elements are then,

l	w_{lm}
0	(w_{00})
1	$(0, w_{10}, 0)$
2	$(0, 0, w_{20}, 0, 0)$
3	$(0, 0, 0, w_{30}, 0, 0, 0)$
4	$(w_{44}, 0, 0, 0, w_{40}, 0, 0, 0, w_{44})$

Case: $\vec{d} = [1, 1, 0]$

In this boosted frame, there is a symmetry under interchange of axes $1 \leftrightarrow 2$ and reflection of the third axis $\boldsymbol{e}_3$.

The non-zero elements are,

l	w_{lm}
0	(w_{00})
1	$\sqrt{2} \operatorname{Re}(e^{i\pi/4}, 0, -e^{-i\pi/4})$
2	$(w_{22}, 0, w_{20}, 0, -w_{22})$
3	$\sqrt{2}(e^{-i\pi/4} \operatorname{Re} w_{33}, 0, e^{i\pi/4} \operatorname{Re} w_{31}, 0, -e^{-i\pi/4} \operatorname{Re} w_{31}, 0, -e^{i\pi/4} \operatorname{Re} w_{33})$
4	$(w_{44}, 0, w_{42}, 0, w_{40}, 0, -w_{42}, 0, w_{44})$

Case: $\vec{d} = [1, 1, 1]$

The symmetry for this frame is reduced to a cyclic permutation of the axis $1 \leftarrow 2 \leftarrow 3 \leftarrow 1$. The non-zero w_{lm} elements are,

l	w_{lm}
0	(w_{00})
1	$w_{10}(-e^{i\pi/4}, 1, e^{-i\pi/4})$
2	$w_{22}(1, -\sqrt{2}e^{-i\pi/4}, 0, -\sqrt{2}e^{i\pi/4}, -1)$
3	$(-\frac{\sqrt{10}}{4}e^{-i\pi/4}w_{30}, w_{32}, \frac{\sqrt{6}}{4}e^{i\pi/4}w_{30}, w_{30}, -\frac{\sqrt{6}}{4}e^{-i\pi/4}w_{30}, -w_{32}, \frac{\sqrt{10}}{4}e^{i\pi/4}w_{30})$
4	$(\frac{\sqrt{70}}{14}w_{40}, -\frac{\sqrt{7}}{2}e^{i\pi/4}w_{42}, w_{42}, \frac{1}{2}e^{-i\pi/4}w_{42}, w_{40}, \frac{1}{2}e^{i\pi/4}w_{42}, -w_{42}, -\frac{\sqrt{7}}{2}e^{-i\pi/4}w_{42}, \frac{\sqrt{70}}{14}w_{40})$

4.2.1 Irrep Basis for quantization condition

The determinant condition in Eq. (4.46) can be simplified when $\mathcal{M}$ is written on such a basis that leads to a block-diagonal form. In this form, the determinant is simply the products of separate determinants from the blocks. Following [70], the basis vectors of the irrep Λ for half-integer spin can be written as,

$$|\Lambda r Jln\rangle = \sum_{\mu} c_{Jl\mu}^{\Lambda rn} |Jl\mu\rangle \tag{4.49}$$

where r represents the row and n labels the occurrence of the irrep Λ. The basis vectors and the coefficients $c_{Jl\mu}^{\Lambda rn}$ [2] for the frames and irreps used are given in Tab. 4.2, Tab. 4.3, Tab. 4.4, and Tab. 4.5 for $l \leq 2$. The matrix elements of $\mathcal{M}$ in the new basis are given by

$$\langle \Lambda r Jln| \mathcal{M} |\Lambda' r' J'l'n'\rangle = \sum_{\mu\mu'} c_{Jl\mu}^{\Lambda rn} c_{J'l'\mu'}^{\Lambda'r'n'} \mathcal{M}_{Jln,J'l'n'} \tag{4.50}$$

And we find from Schur's lemma that the matrix $\mathcal{M}$ is partially diagonalized (in irrep Λ and rows r) in the new basis as,

$$\langle \Lambda r Jln| \mathcal{M} |\Lambda' r' J'l'n'\rangle = \delta_{\Lambda\Lambda'}\delta_{rr'}\mathcal{M}_{Jln,J'l'n'} \tag{4.51}$$

This change in the irrep basis makes Eq. (4.46) simpler to tackle as it block-diagonalizes the determinant condition in separate conditions for each irrep Λ as,

$$\det(\mathcal{M}_{Jln,J'l'n'}^{\Lambda} - \delta_{JJ'}\delta_{ll'}\delta_{nn'}\cot\delta_{Jl}) = 0 \tag{4.52}$$

4.3 Reduced matrices and quantization conditions

In this section, we discuss the block-diagonalized matrices $\mathcal{M}^{\Lambda}$ in the irrep basis. Each contains, in principle, infinitely many partial waves; however, the contributions from higher

---

[2]detail for the computation of the coefficients can be found in [73]

partial waves are further suppressed [3]. Irreps are characterized by content in total angular momentum J, and for each J there are different possible orbital angular momentum l associated, depending on the spin of the particles. For the $N\pi$ system, irreps that contain $J = 3/2$ have a contribution from the resonant P-wave ($l = 1$), but also the D-wave ($l = 2$), with the former being the dominant. Several irreps mix $J = 3/2$ with $J = 1/2$, wherein the latter, two extra contributions can come from S- and P-wave (orbital angular momenta $l = 0, 1$). Nevertheless, at our level of precision, we limit the partial wave contribution to the combinations ($J = \frac{1}{2}, l = 0$) and ($J = \frac{3}{2}, l = 1$). The P-wave (with $J = \frac{3}{2}$) represents the phase shift of the $\Delta(1232)$ resonance, which is the primary goal of the study. While the S-wave (with $J = \frac{1}{2}$) measures the main non-resonant contribution, where the closest resonance in energy resonance would be around 1.62 GeV (see Tab. 2.1). This resonance is still quite far in energy to expect a substantial contribution, thus we do not expect a precise measure of the non-resonant phase shift.

$$\vec{d} = [0, 0, 0], O_h^D$$

Λ	J	l	r	Basis vectors
$G_{1g/u}$	$\frac{1}{2}$	0	1	$\left|\frac{1}{2}, \frac{1}{2}\right\rangle$
			2	$\left|\frac{1}{2}, -\frac{1}{2}\right\rangle$
$G_{1g/u}$	$\frac{1}{2}$	1	1	$\left|\frac{1}{2}, \frac{1}{2}\right\rangle$
			2	$\left|\frac{1}{2}, -\frac{1}{2}\right\rangle$
$H_{g/u}$	$\frac{3}{2}$	1	1	$\left|\frac{3}{2}, \frac{3}{2}\right\rangle$
			2	$\left|\frac{3}{2}, \frac{1}{2}\right\rangle$
			3	$\left|\frac{3}{2}, -\frac{1}{2}\right\rangle$
			4	$\left|\frac{3}{2}, -\frac{3}{2}\right\rangle$
$H_{g/u}$	$\frac{3}{2}$	2	1	$\left|\frac{3}{2}, \frac{3}{2}\right\rangle$
			2	$\left|\frac{3}{2}, \frac{1}{2}\right\rangle$
			3	$\left|\frac{3}{2}, -\frac{1}{2}\right\rangle$
			4	$\left|\frac{3}{2}, -\frac{3}{2}\right\rangle$

Table 4.2 Basis vectors for irreducible representations $G_{1g/u}, H_{g/u}$ of group O_h^D [73].

In the rest frame the symmetry group is O_h^D and the irreps are $G_{1g/u}$ and $H_{g/u}$. The matrix $\mathcal{M}^{\vec{d}}$ computed in this frame for our combinations ($J = 3/2, l = 1$) and ($J = 1/2, l = 0$) is

$$\mathcal{M}^{(0,0,0)}_{Jl\mu, J'l'\mu'} = \begin{array}{c} \\ \frac{1}{2},0,-\frac{1}{2} \\ \frac{1}{2},0,\frac{1}{2} \\ \frac{3}{2},1,-\frac{3}{2} \\ \frac{3}{2},1,-\frac{1}{2} \\ \frac{3}{2},1,\frac{1}{2} \\ \frac{3}{2},1,\frac{3}{2} \end{array} \begin{pmatrix} w_{00} & 0 & 0 & 0 & 0 & 0 \\ 0 & w_{00} & 0 & 0 & 0 & 0 \\ 0 & 0 & w_{00} & 0 & 0 & 0 \\ 0 & 0 & 0 & w_{00} & 0 & 0 \\ 0 & 0 & 0 & 0 & w_{00} & 0 \\ 0 & 0 & 0 & 0 & 0 & w_{00} \end{pmatrix} \tag{4.53}$$

with column headers $\frac{1}{2},0,-\frac{1}{2}$ $\quad$ $\frac{1}{2},0,\frac{1}{2}$ $\quad$ $\frac{3}{2},1,-\frac{3}{2}$ $\quad$ $\frac{3}{2},1,-\frac{1}{2}$ $\quad$ $\frac{3}{2},1,\frac{1}{2}$ $\quad$ $\frac{3}{2},1,\frac{3}{2}$

After the change of basis using Eq. (4.50) and coefficients in Tab. 4.2, we get the (block) matrices $\mathcal{M}^\Lambda$ for the irrep G_{1u} and H_g ,

$$
\left(\mathcal{M}^{G_{1u}}_{Jl,J'l'}\right) = \begin{array}{c} \\ \frac{1}{2},0 \\ \frac{1}{2},1 \end{array} \overset{\displaystyle \frac{1}{2},0 \quad \frac{1}{2},1}{\begin{pmatrix} w_{00} & 0 \\ 0 & 0 \end{pmatrix}}
\tag{4.54}
$$

$$
\left(\mathcal{M}^{H_g}_{Jl,J'l'}\right) = \begin{array}{c} \\ \frac{3}{2},0 \\ \frac{3}{2},1 \end{array} \overset{\displaystyle \frac{3}{2},0 \quad \frac{3}{2},1}{\begin{pmatrix} w_{00} & 0 \\ 0 & 0 \end{pmatrix}}
\tag{4.55}
$$

which results, applying Eq. (4.52), in the quantization condition for irrep G_{1u}:

$$
- w_{00} + \cot \delta_{\frac{1}{2},0} = 0
\tag{4.56}
$$

and the quantization condition for irrep H_g:

$$
- w_{00} + \cot \delta_{\frac{3}{2},0} = 0
\tag{4.57}
$$

$\vec{d} = [0,0,1], C^D_{4v}$

Λ	J	l	r	Basis vectors
G_1	$\frac{1}{2}$	0	1	$\left|\frac{1}{2},\frac{1}{2}\right\rangle$
			2	$-\left|\frac{1}{2},-\frac{1}{2}\right\rangle$
G_1	$\frac{1}{2}$	1	1	$\left|\frac{1}{2},\frac{1}{2}\right\rangle$
			2	$\left|\frac{1}{2},-\frac{1}{2}\right\rangle$
G_1	$\frac{3}{2}$	1	1	$\left|\frac{3}{2},\frac{1}{2}\right\rangle$
			2	$-\left|\frac{3}{2},-\frac{1}{2}\right\rangle$
G_1	$\frac{3}{2}$	2	1	$\left|\frac{3}{2},\frac{1}{2}\right\rangle$
			2	$\left|\frac{3}{2},-\frac{1}{2}\right\rangle$
G_2	$\frac{3}{2}$	1	1	$\left|\frac{3}{2},-\frac{3}{2}\right\rangle$
			2	$\left|\frac{3}{2},\frac{3}{2}\right\rangle$
G_2	$\frac{3}{2}$	2	1	$\left|\frac{3}{2},-\frac{3}{2}\right\rangle$
			2	$-\left|\frac{3}{2},\frac{3}{2}\right\rangle$

Table 4.3 Basis vectors for irreducible representations G_1, G_2 of little group C^D_{4v} [70].

In this frame the symmetry group is C_{4v}^D with irreps G_1 and G_2. The matrix $\mathcal{M}^{\vec{d}}$ is,

$$\mathcal{M}^{(0,0,1)}_{Jl\mu,J'l'\mu'} = \begin{array}{c} \\ \frac{1}{2},0,\text{-}\frac{1}{2} \\ \frac{1}{2},0,\ \frac{1}{2} \\ \frac{3}{2},1,\text{-}\frac{3}{2} \\ \frac{3}{2},1,\text{-}\frac{1}{2} \\ \frac{3}{2},1,\ \frac{1}{2} \\ \frac{3}{2},1,\ \frac{3}{2} \end{array} \overset{\displaystyle \begin{array}{cccccc} \frac{1}{2},0,\text{-}\frac{1}{2} & \frac{1}{2},0,\frac{1}{2} & \frac{3}{2},1,\text{-}\frac{3}{2} & \frac{3}{2},1,\text{-}\frac{1}{2} & \frac{3}{2},1,\frac{1}{2} & \frac{3}{2},1,\frac{3}{2} \end{array}}{\left(\begin{array}{cccccc} w_{00} & 0 & -i\sqrt{2}w_{10} & 0 & 0 & 0 \\ 0 & w_{00} & 0 & 0 & -i\sqrt{2}w_{10} & 0 \\ 0 & 0 & w_{00}-w_{20} & 0 & 0 & 0 \\ i\sqrt{2}w_{10} & 0 & 0 & w_{00}+w_{20} & 0 & 0 \\ 0 & i\sqrt{2}w_{10} & 0 & 0 & w_{00}+w_{20} & 0 \\ 0 & 0 & 0 & 0 & 0 & w_{00}-w_{20} \end{array} \right)}$$

$$(4.58)$$

From the change to irreps basis, using Eq. (4.50) and coefficients in Tab. 4.3, we get the (block) matrices $\mathcal{M}^{\Lambda}$ for the irrep G_1 and G_2 ,

$$\left(\mathcal{M}^{G_1}_{Jl,J'l'}\right) = \begin{array}{c} \\ \frac{1}{2},0 \\ \frac{1}{2},1 \\ \frac{3}{2},1 \\ \frac{3}{2},2 \end{array} \overset{\displaystyle \begin{array}{cccc} \frac{1}{2},0 & \frac{1}{2},1 & \frac{3}{2},1 & \frac{3}{2},2 \end{array}}{\left(\begin{array}{cccc} w_{00} & 0 & i\sqrt{2}w_{10} & 0 \\ 0 & 0 & 0 & 0 \\ -i\sqrt{2}w_{10} & 0 & w_{00}+w_{20} & 0 \\ 0 & 0 & 0 & 0 \end{array} \right)}, \qquad (4.59)$$

$$\left(\mathcal{M}^{G_2}_{Jl,J'l'}\right) = \begin{array}{c} \\ \frac{3}{2},1 \\ \frac{3}{2},2 \end{array} \overset{\displaystyle \begin{array}{cc} \frac{3}{2},1 & \frac{3}{2},2 \end{array}}{\left(\begin{array}{cc} w_{00}-w_{20} & 0 \\ 0 & 0 \end{array} \right)} \qquad (4.60)$$

which results in the quantization condition for irrep G_1:

$$-2w_{10}^2 + (w_{00} - \cot\delta_{\frac{1}{2},0})(w_{00} + w_{20} - \cot\delta_{\frac{3}{2},1}) = 0 \qquad (4.61)$$

and quantization condition for irrep G_2:

$$-w_{00} + w_{20} + \cot\delta_{\frac{3}{2},1} = 0 \qquad (4.62)$$

$\vec{d} = [\mathbf{1,1,0}], C_{2v}^D$

In this frame the symmetry group is C_{2v}^D and there is only the irrep G which have a double occurence for $J = 3/2$ and $l = 1, 2$. Hence, we label it as $(2)G$ throughout the thesis. The two occurences are differentiated with an additional label, n. The computed matrix

Λ	J	l	r	Basis vectors
$(2)G$	$\frac{1}{2}$	0	1	$\left|\frac{1}{2},-\frac{1}{2}\right\rangle$
			2	$-i\left|\frac{1}{2},\frac{1}{2}\right\rangle$
$(2)G$	$\frac{1}{2}$	1	1	$\left|\frac{1}{2},\frac{1}{2}\right\rangle$
			2	$\left|\frac{1}{2},-\frac{1}{2}\right\rangle$
$(2)G$	$\frac{3}{2}$	1	1	$\left|\frac{3}{2},-\frac{3}{2}\right\rangle$
			2	$\left|\frac{3}{2},\frac{3}{2}\right\rangle$
$(2)G$	$\frac{3}{2}$	1	1	$-\left|\frac{3}{2},\frac{1}{2}\right\rangle$
			2	$\left|\frac{3}{2},-\frac{1}{2}\right\rangle$
$(2)G$	$\frac{3}{2}$	2	1	$i\left|\frac{3}{2},\frac{3}{2}\right\rangle$
			2	$\left|\frac{3}{2},-\frac{3}{2}\right\rangle$
$(2)G$	$\frac{3}{2}$	2	1	$\left|\frac{3}{2},-\frac{1}{2}\right\rangle$
			2	$i\left|\frac{3}{2},\frac{1}{2}\right\rangle$

Table 4.4 Basis vectors for irreducible representations $(2)G$ of little group C_{2v}^D [70].

$\mathcal{M}^{(1,1,0)}_{Jl\mu,J'l'\mu'}$ for this frame is

$$
\begin{array}{c}
\quad\quad \frac{1}{2},0,\text{-}\frac{1}{2} \quad\quad \frac{1}{2},0,\frac{1}{2} \quad\quad \frac{3}{2},1,\text{-}\frac{3}{2} \quad\quad \frac{3}{2},1,\text{-}\frac{1}{2} \quad\quad \frac{3}{2},1,\frac{1}{2} \quad\quad \frac{3}{2},1,\frac{3}{2} \\
\begin{array}{c}
\frac{1}{2},0,\text{-}\frac{1}{2} \\
\frac{1}{2},0,\frac{1}{2} \\
\frac{3}{2},1,\text{-}\frac{3}{2} \\
\frac{3}{2},1,\text{-}\frac{1}{2} \\
\frac{3}{2},1,\frac{1}{2} \\
\frac{3}{2},1,\frac{3}{2}
\end{array}
\left(
\begin{array}{cccccc}
w_{00} & 0 & (-1+i)\sqrt{3}\mathrm{Re}(w_{11}) & 0 & (1+i)\mathrm{Re}(w_{11}) & 0 \\
0 & w_{00} & 0 & (-1+i)\mathrm{Re}(w_{11}) & 0 & (1+i)\sqrt{3}\mathrm{Re}(w_{11}) \\
(1+i)\sqrt{3}\mathrm{Re}(w_{11}) & 0 & w_{00}-w_{20} & 0 & \sqrt{2}w_{22} & 0 \\
0 & (1+i)\mathrm{Re}(w_{11}) & 0 & w_{00}+w_{20} & 0 & \sqrt{2}w_{22} \\
(-1+i)\mathrm{Re}(w_{11}) & 0 & -\sqrt{2}w_{22} & 0 & w_{00}+w_{20} & 0 \\
0 & (-1+i)\sqrt{3}\mathrm{Re}(w_{11}) & 0 & -\sqrt{2}w_{22} & 0 & w_{00}-w_{20}
\end{array}
\right)
\end{array}
\tag{4.63}
$$

which transform using Eq. (4.50) and coefficients in Tab. 4.4 to $\mathcal{M}^{(2)G}_{Jl[n],J'l'[n']} =$

$$
\begin{array}{c}
\quad\quad \frac{1}{2},0 \quad\quad \frac{1}{2},1 \quad\quad \frac{3}{2},1[1] \quad\quad \frac{3}{2},1[2] \quad \frac{3}{2},2[1] \quad \frac{3}{2},2[2] \\
\begin{array}{c}
\frac{1}{2},0 \\
\frac{1}{2},1 \\
\frac{3}{2},1[1] \\
\frac{3}{2},1[2] \\
\frac{3}{2},2[1] \\
\frac{3}{2},2[2]
\end{array}
\left(
\begin{array}{cccccc}
w_{00} & 0 & (1+i)\sqrt{3}\mathrm{Re}(w_{11}) & (1-i)\mathrm{Re}(w_{11}) & 0 & 0 \\
0 & 0 & 0 & 0 & 0 & 0 \\
(-1+i)\sqrt{3}\mathrm{Re}(w_{11}) & 0 & w_{00}-w_{20} & \sqrt{2}w_{22} & 0 & 0 \\
(-1-i)\mathrm{Re}(w_{11}) & 0 & -\sqrt{2}w_{22} & w_{00}+w_{20} & 0 & 0 \\
0 & 0 & 0 & 0 & 0 & 0 \\
0 & 0 & 0 & 0 & 0 & 0
\end{array}
\right)
\end{array}
\tag{4.64}
$$

which result in the quantization condition for the irrep $(2)G$:

$$
-(w_{00}-\cot\delta_{\frac{1}{2},0})(-w_{20}^2+2w_{22}^2+(w_{00}-\cot\delta_{\frac{3}{2},1})^2)-4\Re(w_{11})^2(2w_{00}+w_{20}-i\sqrt{6}w_{22}-2\cot\delta_{\frac{3}{2},1})=0
\tag{4.65}
$$

$\vec{d} = [\mathbf{1,1,1}], C_{3v}^D$

Λ	J	l	r	Basis vectors
G	$\frac{1}{2}$	0	1	$\frac{\sqrt{6}}{3}\left|\frac{1}{2},-\frac{1}{2}\right\rangle + \frac{1}{\sqrt{6}}(1-i)\left|\frac{1}{2},\frac{1}{2}\right\rangle$
			2	$-\frac{1}{\sqrt{6}}(1-i)\left|\frac{1}{2},-\frac{1}{2}\right\rangle - \frac{\sqrt{6}}{3}i\left|\frac{1}{2},\frac{1}{2}\right\rangle$
G	$\frac{1}{2}$	1	1	$\left|\frac{1}{2},\frac{1}{2}\right\rangle$
			2	$\left|\frac{1}{2},-\frac{1}{2}\right\rangle$
G	$\frac{3}{2}$	1	1	$\frac{1}{\sqrt{6}}(1+i)\left|\frac{3}{2},-\frac{3}{2}\right\rangle + \frac{1}{\sqrt{2}}\left|\frac{3}{2},-\frac{1}{2}\right\rangle + \frac{1}{\sqrt{6}}i\left|\frac{3}{2},\frac{3}{2}\right\rangle$
			2	$-\frac{1}{\sqrt{6}}\left|\frac{3}{2},-\frac{3}{2}\right\rangle - \frac{1}{\sqrt{2}}i\left|\frac{3}{2},\frac{1}{2}\right\rangle + \frac{1}{\sqrt{6}}(1+i)\left|\frac{3}{2},\frac{3}{2}\right\rangle$
G	$\frac{3}{2}$	2	1	$\frac{1}{\sqrt{6}}\left|\frac{3}{2},-\frac{1}{2}\right\rangle + \frac{1}{\sqrt{6}}(1-i)\left|\frac{3}{2},\frac{1}{2}\right\rangle + \frac{1}{\sqrt{2}}i\left|\frac{3}{2},\frac{3}{2}\right\rangle$
			2	$\frac{1}{\sqrt{2}}\left|\frac{3}{2},-\frac{3}{2}\right\rangle + \frac{1}{\sqrt{6}}(1-i)\left|\frac{3}{2},-\frac{1}{2}\right\rangle + \frac{1}{\sqrt{6}}i\left|\frac{3}{2},\frac{1}{2}\right\rangle$
F_1	$\frac{3}{2}$	1		$-\left(\frac{\sqrt{3}}{6}(1+i)+\frac{\sqrt{6}}{12}(1-i)\right)\left|\frac{3}{2},-\frac{3}{2}\right\rangle + \frac{1}{2}\left|\frac{3}{2},-\frac{1}{2}\right\rangle +$ $\frac{\sqrt{2}}{4}(1+i)\left|\frac{3}{2},\frac{1}{2}\right\rangle + \left(\frac{\sqrt{6}}{6}-\frac{\sqrt{3}}{6}i\right)\left|\frac{3}{2},\frac{3}{2}\right\rangle$
F_1	$\frac{3}{2}$	2		$-\left(\frac{\sqrt{3}}{6}(1+i)-\frac{\sqrt{6}}{12}(1-i)\right)\left|\frac{3}{2},-\frac{3}{2}\right\rangle + \frac{1}{2}\left|\frac{3}{2},-\frac{1}{2}\right\rangle -$ $\frac{\sqrt{2}}{4}(1+i)\left|\frac{3}{2},\frac{1}{2}\right\rangle - \left(\frac{\sqrt{6}}{6}+\frac{\sqrt{3}}{6}i\right)\left|\frac{3}{2},\frac{3}{2}\right\rangle$
F_2	$\frac{3}{2}$	1		$-\left(\frac{\sqrt{3}}{6}(1+i)-\frac{\sqrt{6}}{12}(1-i)\right)\left|\frac{3}{2},-\frac{3}{2}\right\rangle + \frac{1}{2}\left|\frac{3}{2},-\frac{1}{2}\right\rangle -$ $\frac{\sqrt{2}}{4}(1+i)\left|\frac{3}{2},\frac{1}{2}\right\rangle - \left(\frac{\sqrt{6}}{6}+\frac{\sqrt{3}}{6}i\right)\left|\frac{3}{2},\frac{3}{2}\right\rangle$
F_2	$\frac{3}{2}$	2		$-\left(\frac{\sqrt{3}}{6}(1+i)+\frac{\sqrt{6}}{12}(1-i)\right)\left|\frac{3}{2},-\frac{3}{2}\right\rangle + \frac{1}{2}\left|\frac{3}{2},-\frac{1}{2}\right\rangle +$ $\frac{\sqrt{2}}{4}(1+i)\left|\frac{3}{2},\frac{1}{2}\right\rangle + \left(\frac{\sqrt{6}}{6}-\frac{\sqrt{3}}{6}i\right)\left|\frac{3}{2},\frac{3}{2}\right\rangle$

Table 4.5 Basis vectors for irreducible representations G, F_1, F_2 of little group C_{3v}^D [70].

In this frame the symmetry group is C_{3v}^D and the relevant irreps are F_1, F_2 and G. The matrix $\mathcal{M}_{Jl\mu,J'l'\mu'}^{(1,1,1)}$ for this boosted frame is,

$$
\begin{array}{c}
\begin{array}{cccccc}
\frac{1}{2},0,\text{-}\frac{1}{2} & \frac{1}{2},0,\frac{1}{2} & \frac{3}{2},1,\text{-}\frac{3}{2} & \frac{3}{2},1,\text{-}\frac{1}{2} & \frac{3}{2},1,\frac{1}{2} & \frac{3}{2},1,\frac{3}{2}
\end{array} \\
\begin{array}{c}
\frac{1}{2},0,\text{-}\frac{1}{2} \\
\frac{1}{2},0,\ \frac{1}{2} \\
\frac{3}{2},1,\text{-}\frac{3}{2} \\
\frac{3}{2},1,\text{-}\frac{1}{2} \\
\frac{3}{2},1,\ \frac{1}{2} \\
\frac{3}{2},1,\ \frac{3}{2}
\end{array}
\left(
\begin{array}{cccccc}
w_{00} & 0 & (1-i)\sqrt{\frac{3}{2}}w_{10} & -i\sqrt{2}w_{10} & -ie^{\frac{i\pi}{4}}w_{10} & 0 \\
0 & w_{00} & 0 & 0 & -i\sqrt{2}w_{10} & (1+i)\sqrt{\frac{3}{2}}w_{10} \\
(1+i)\sqrt{\frac{3}{2}}w_{10} & 0 & w_{00} & -2e^{\frac{i\pi}{4}}w_{22} & \sqrt{2}w_{22} & 0 \\
i\sqrt{2}w_{10} & ie^{\frac{i\pi}{4}}w_{10} & 2e^{\frac{i\pi}{4}}w_{22} & w_{00} & 0 & \sqrt{2}w_{22} \\
-ie^{\frac{i\pi}{4}}w_{10} & i\sqrt{2}w_{10} & -\sqrt{2}w_{22} & 0 & w_{00} & 2e^{\frac{i\pi}{4}}w_{22} \\
0 & (1-i)\sqrt{\frac{3}{2}}w_{10} & 0 & -\sqrt{2}w_{22} & -2e^{\frac{i\pi}{4}}w_{22} & w_{00}
\end{array}
\right)
\end{array}
$$
(4.66)

and it block diagonalize in the irrep basis applying Eq. (4.50) and coefficients in Tab. 4.5.

We obtain the matrices $\mathcal{M}^\Lambda$ for the irrep G and F_1, F_2:

$$\left(\mathcal{M}^G_{Jl,J'l'}\right) = \begin{array}{c} \\ \frac{1}{2},0 \\ \frac{1}{2},1 \\ \frac{3}{2},1 \\ \frac{3}{2},2 \end{array} \overset{\begin{array}{cccc} \frac{1}{2},0 & \frac{1}{2},1 & \frac{3}{2},1 & \frac{3}{2},2 \end{array}}{\left(\begin{array}{cccc} w_{00} & 0 & i\sqrt{6}w_{10} & 0 \\ 0 & 0 & 0 & 0 \\ -i\sqrt{6}w_{10} & 0 & w_{00} - i\sqrt{6}w_{22} & 0 \\ 0 & 0 & 0 & 0 \end{array} \right)}, \tag{4.67}$$

$$\left(\mathcal{M}^{F_1,F_2}_{Jl,J'l'}\right) = \begin{array}{c} \\ \frac{3}{2},1 \\ \frac{3}{2},2 \end{array} \overset{\begin{array}{cc} \frac{3}{2},1 & \frac{3}{2},2 \end{array}}{\left(\begin{array}{cc} w_{00} + i\sqrt{6}w_{22} & 0 \\ 0 & 0 \end{array} \right)} \tag{4.68}$$

which result in the quantization condition for G:

$$- 6w_{10}^2 + (w_{00} - \cot\delta_{\frac{1}{2},0})(w_{00} - i\sqrt{6}w_{22} - \cot\delta_{\frac{3}{2},1}) = 0 \tag{4.69}$$

and the quantization condition for both irreps F_1, F_2:

$$- w_{00} - i\sqrt{6}w_{22} + \cot\delta_{\frac{3}{2},1} = 0 \tag{4.70}$$

Chapter Five

Results

Label	$N_s^3 \times N_t$	β	am_l	am_s	a (fm)	m_π (MeV)	$m_\pi L$	N_{conf}
A7	$24^3 \times 48$	3.31	-0.09530	-0.040	0.1163(4)	255.4(1.6)	3.61(2)	600

Table 5.1 Parameters of the lattice gauge-field ensemble A7.

In this section, we present results obtained on the ensemble outlined in Tab. 5.1 for 9600 measurements: 600 configurations with 16 source locations each.

5.1 Contractions and spectra analysis

In this work, we use a gauge-field ensemble (label A7) with a pion mass of ≈ 250 MeV and spatial lattice size $L \approx 2.8$ fm [87]. The parameters for this ensemble are given in Tab. 5.1.

The gluon action is a tree-level $O(a^2)$-improved Symanzik action [10] together with tree-level clover improved Wilson fermions [13]. The clover-improved Wilson action is also used for sea and valence quarks. The gauge links in the fermion action are smeared using two levels of HEX smearing [88]. Additional details on action and algorithm are provided in [88].

From the interpolators presented in Sec. 3.1, two-point functions are computed. The interpolators are the single hadrons pion (π), nucleon (N), delta (Δ), and the multi-hadron nucleon-pion ($N\pi$).

The first steps of the computational plan consist of:

- the solution of sparse linear systems (inversion of the Dirac matrix) producing point-to-all, sequential and stochastic timeslice-to-all quark propagators (more details in [89]).

- Wick contractions (generalized scalar products of tensor quantities) of propagators to produce 2-point correlation functions[1]. We follow the scheme outlined in [17, 3].

The correlators with single-baryon interpolator are constructed from point-to-all propagators, while the correlators with a single-hadron interpolator at the sink and a two-hadron

---

[1]also 3-point functions are produced for future studies
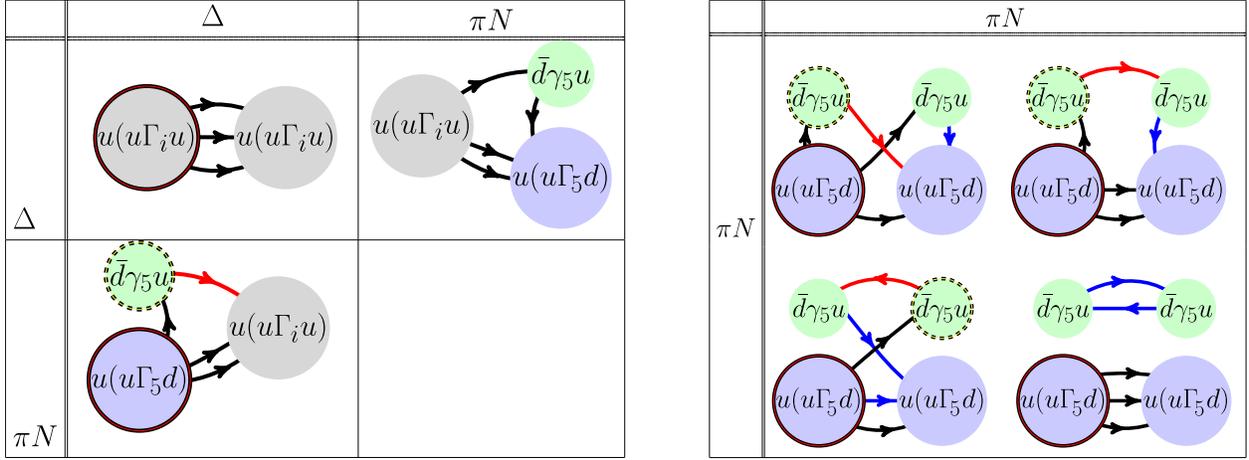
Figure 5.1 Left panel: Two-point function contractions containing the Δ interpolator. Grey circles represent the Δ, green circles represent the π, and blue circles represent the N. A circle with a black outline represents a point source, while the dotted outline represents a sequential source. Point-to-all propagators are represented by black arrow lines, and sequential propagators are indicated by red arrow lines. The contractions with the $N\pi$ operator at the sink and the Δ operator at the source are not computed directly but are obtained from the contraction with the Δ operator at the sink and the $N\pi$ operator at the source through conjugation. Right panel: Two-point function contractions for $\pi N - \pi N$. The blue arrow lines represent stochastic propagators, while the other elements are analogous to the left panel.

$N\pi$ interpolator at the source use in addition a sequential propagator, with sequential inversion through the pion vertex at source time. Fig. 5.1 shows, in the left panel, the topology of diagrams obtained from the $\Delta - \Delta$ and $\Delta - N\pi$ two-point correlation functions. On the right panel, we show the $N\pi - N\pi$ type correlators. To optimize the computational cost, the diagrams are split into two factors, separated at the source point and by using a stochastic source - propagator pair. For the latter, we use stochastic timeslice sources in the upper two diagrams of the right panel in Fig. 5.1. The lower diagrams employ spin-dilution and the one-end-trick [90] in addition to time dilution. The quark propagators of all types are Wuppertal-smeared [91] at source and sink with smearing parameters $\alpha_{\mathrm{Wup}} = 3.0$ and $N_{\mathrm{Wup}} = 45$; these parameters were originally optimized for the nucleon two-point functions in [87]. The gauge field deployed in the smearing kernel is again 2-level HEX-smeared [15, 16].

Once completed, these correlators are projected to the proper irrep Λ with the projection method (as outlined in Sec. 3.3). The two-point functions obtained are the building blocks of correlation matrices such as

$$C_{ij}^{\Lambda,\vec{P}} = \langle O_i^{\Lambda,\vec{P}}(t_{snk})\bar{O}_j^{\Lambda,\vec{P}}(t_{src})\rangle \tag{5.1}$$

where i, j label different operators, and t_{snk} is the sink time and t_{src} is the source time. For each irrep Λ a correlation matrix $C_{ij}^{\Lambda,\vec{P}}$ is constructed, for both the single nucleon N operators (listed in Tab. B.9), and the coupled system $\Delta - N\pi$ operators (listed in Tab. 3.7). The single pion has only one operator; thus, the correlation matrix is a single entry. To extract the energy levels $E_n^{\Lambda,\vec{P}}$ the generalized eigenvalue problem (GEVP) is used

$$C_{ij}^{\Lambda,\vec{P}}(t)u_j^n(t) = \lambda^n(t,t_0)C_{ij}^{\Lambda,\vec{P}}u_j^n(t) \tag{5.2}$$

where u_j^n are the right generalized eigenvectors that are clearest in the plateau region. We can write the full set of states in a finite volume as

$$I = \sum_n \frac{|n\rangle \langle n|}{2E_n} \tag{5.3}$$

with which we can rewrite the two-point functions as

$$C_{ij}^{\Lambda,\vec{P}} = \sum_n \frac{Z_i^n Z_j^{n*}}{2E_n}e^{-E_n t} \tag{5.4}$$

where the factors Z_i^n measure the overlaps of the interpolating operators with the states, i.e. how well the operator O_i described the $n-$th state of the spectrum. Early time slices close to the source location often include excited states of quantum numbers equal to the ground-state we aim to extract. Nonetheless, the higher the energy of the state the faster the exponential decay, leading, in the large time limit, to a single exponential surviving. In the plateau region, the pollution from higher energy states is reasonably small, thus the energies are then obtained from fits with a single exponential as

$$\lambda^n(t,t_0) \sim e^{-E_n^{\Lambda,\vec{P}}(t-t_0)} \tag{5.5}$$

55

where t_0 is a reference timeslice that does not affect the large-t behavior; we choose $t_0/a = 2$. Nevertheless, we also employ a two-exponential form (from the fit function of Eq. (4) of [92]) with contribution from the higher excited state of energy $E_n'^{\Lambda,\vec{P}}$ as

$$\lambda^n(t, t_0) \sim (1 - B)e^{-E_n^{\Lambda,\vec{P}}(t-t_0)} + Be^{-E_n'^{\Lambda,\vec{P}}(t-t_0)} \tag{5.6}$$

These fits usually give consistent results for $E_n^{\Lambda,\vec{P}}$, but the results for the parameter B are rather unstable under variations of t_{min}, suggesting that there is no suitable time region in which this model is appropriate. For this reason, we do not show the results of the two-exponential fits. In the following plots, we show the effective masses, defined as

$$aE_{eff}^n(t) = \ln \frac{\lambda_n(t, t_0)}{\lambda_n(t + a, t_0)} \tag{5.7}$$

along with fits over the generalized eigenvalues $\lambda^n(t, t_0)$. Using the extracted energy values, the center-of-mass energies $\sqrt{s_n}^{\vec{P},\Lambda}$ can be computed, which relate to the laboratory-frame energies $E_n^{\Lambda,\vec{P}}$ and scattering momentum p^* via

$$\begin{aligned} \sqrt{s_n}^{\vec{P},\Lambda} &= \sqrt{(E_n^{\Lambda,\vec{P}})^2 - (\vec{P})^2} \\ &= \sqrt{p^{*2} + m_1^2} + \sqrt{p^{*2} + m_2^2} \end{aligned} \tag{5.8}$$

5.2 Spectra results: Single Hadron

The Lüscher analysis necessitates the pion and nucleon masses to relate energies to scattering momenta. Here we outline the spectra analysis of the single-hadron correlation functions computed on the ensemble A7 (details in Tab. 5.1).
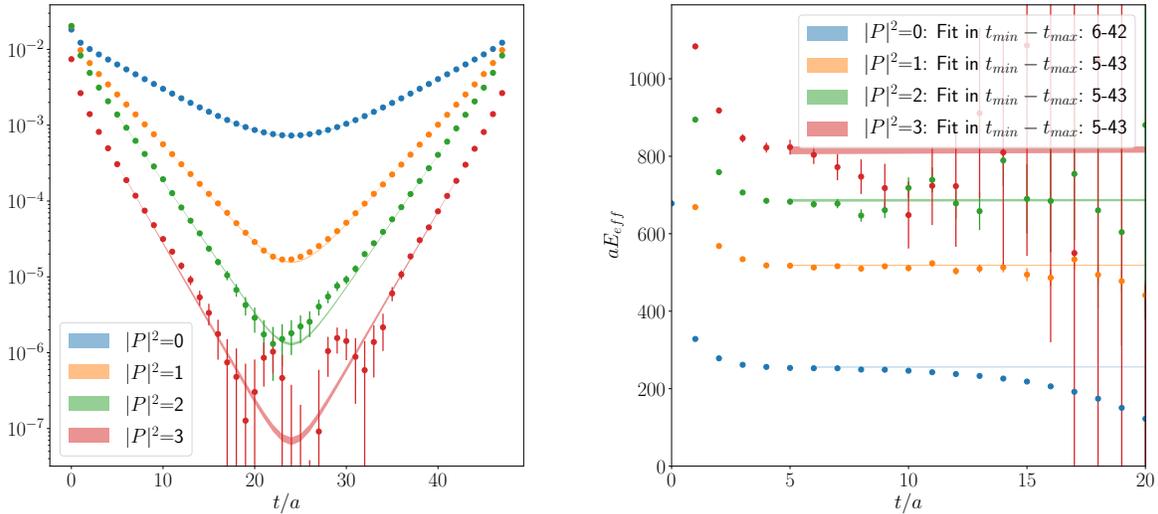
Figure 5.2 Left panel: pion correlators and fit results (fit function: cosh). Right panel: effective mass plot of the pion correlators with fit results (choice of time range shown in the legend).

5.2.1 Pion

The isospin $I = 1$, spin $S = 0$, parity $P = -1$ pion interpolator is outlined in Eq. (3.2). The internal gamma matrix structure of the interpolator is limited to γ_5. Given the simple spinless structure of the pseudoscalar particle, the interpolator is not affected by group projection and is used directly to build two-point functions.

Fig. 5.2 shows the correlators for the pion at rest and three different momenta $\vec{P}$. The pion correlator has a reasonably good signal-to-noise ratio, and, as expected, the precision of the correlators gradually diminish when going from rest-frame $|P|^2 = 0$ (blue points) to the highest momentum $|P|^2 = 3(2\pi/L)^2$ (red points). The same figure shows the correlators' fit using the *cosh* function, which generally described two exponentials with opposite signs in the exponent. The hyperbolic cosine describes the pion correlators on the lattice where the forward and backward (in time) propagator fall exponentially as it propagates away from the source location.

The search for an optimal time range for the fit is called stability fit and is shown in Fig. 5.3. For each momentum, we fit the correlators for different time ranges from t_{min} to $t_{max} = N_t - t_{min}$. The onset of a plateau signals the optimal range, for which the fit
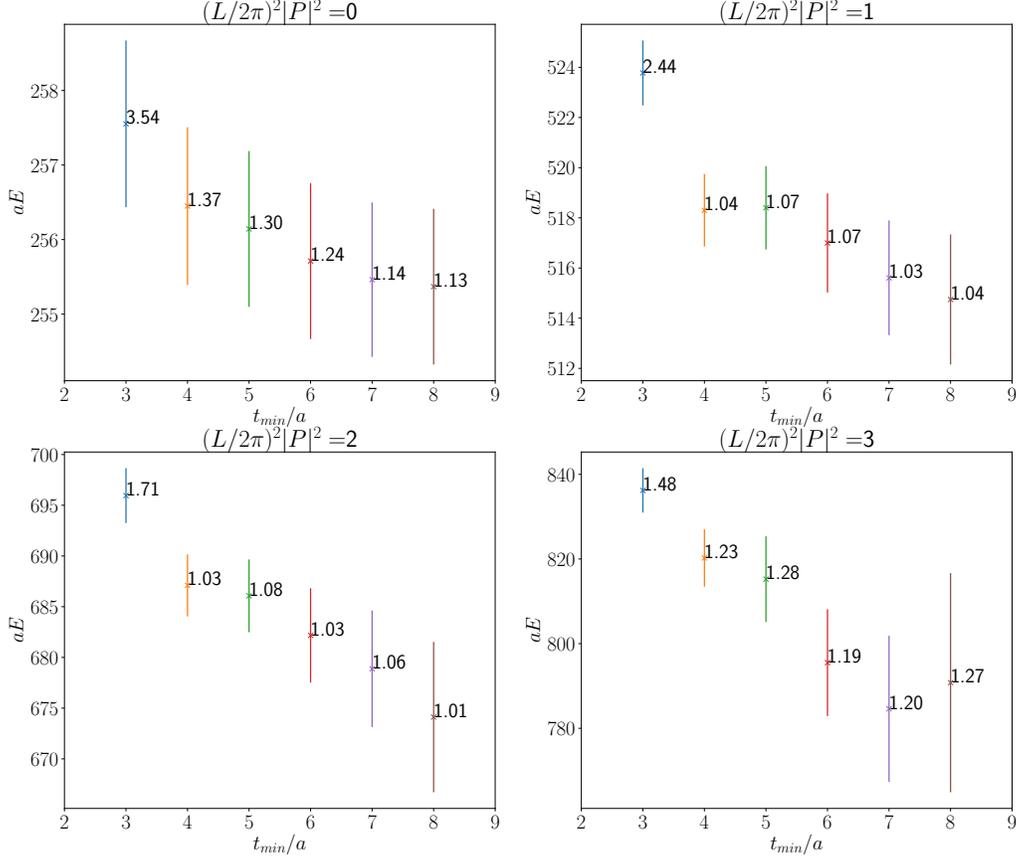
Figure 5.3 Stability fit for the pion correlators at various $(\frac{L}{2\pi}|P|)^2$. The fit function *cosh* is applied to the range from t_{min} to $t_{max} = N_t - t_{min}$. The result for each χ^2/ndf is listed at points.

maximally describes the ground state correlators uncontaminated from the higher energy states. Fig. 5.2 shows the effective mass for the pion along with the energies extracted from the stability fit analysis. We combine these energies and fit the points (using a least-square method) with the dispersion relation $(aE)^2 = (am_\pi)^2 + c^2(ap)^2$.

The results from the fit, visible in Fig. 5.4, are

- $am_\pi = 0.15052 \pm 0.00078$, $c = 1.0105 \pm 0.0023$, $\chi^2/ndf = 0.154$

The pion mass is used later in the phase shift's parametrization when fitting the energy points from the $N\pi$ system extracted from the lattice.
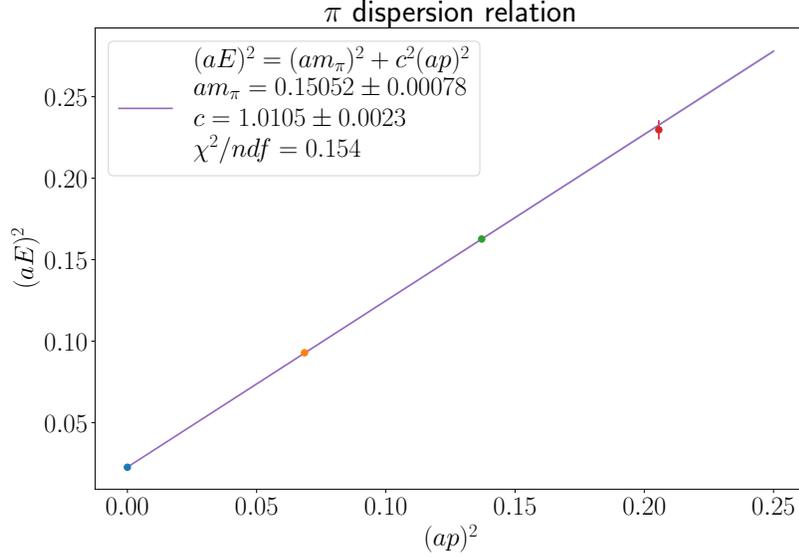
Figure 5.4 Dispersion relation of the pion.

5.2.2   Nucleon

We now look at the isospin $I = 1/2$, spin $S = 1/2$, parity $P = +1$ nucleon interpolator listed in Eq. (3.5). To correctly identify the $J = 1/2$ component, we project the hadron in the proper irrep. A summary of the relevant information about groups and irreps associated with the quantum numbers of the nucleon are listed in Tab. 3.5 (and visually in Fig. 3.1). In the rest frame, it belongs to the positive parity irrep G_{1g} (under the double group O_h^D) and it subsequently subduces to irrep G_1 of little groups C_{4v}, and irrep G in both groups C_{2v} and C_{3v}. The formulas and transformations implemented for the projection of the nucleon are outlined in Sec. 3.3.1. It is instructive to take a look at the actual form of a projected operator shown in Tab. B.9. Listed are examples of operators for each row and occurrence of irrep Λ. We list only one momentum direction for brevity, but we project on all momenta permutations and average the correlators to increase statistics in the actual computation.

As previously outlined in Sec. 3.1.2, we use two gamma matrix combinations to increase the number of operators that are used to construct correlation matrices. The labels for two nucleons are

- "A" $\rightarrow N_\mu^{(2)}(\vec{p}) = \sum_{\vec{x}} \epsilon_{abc}(u_a(\vec{x}))_\mu(u_b^T(\vec{x})C\gamma_0\gamma_5 d_c(\vec{x})) \, e^{i\vec{p}\cdot\vec{x}}$

- "B" $\rightarrow N_\mu^{(1)}(\vec{p}) = \sum_{\vec{x}} \epsilon_{abc}(u_a(\vec{x}))_\mu(u_b^T(\vec{x})C\gamma_5 d_c(\vec{x})) \, e^{i\vec{p}\cdot\vec{x}}$

The correlators for both operators are analyzed with a stability fit method (shown in Fig. 5.5) to identify the plateau area where the contribution from higher energy states becomes negligible. The fit function is a single exponential applied to the correlators, and, contrary to the pion case, the fit range is limited to the first half of the time range. In particular, once we choose an upper limit t_{max} large enough the fit result becomes independent
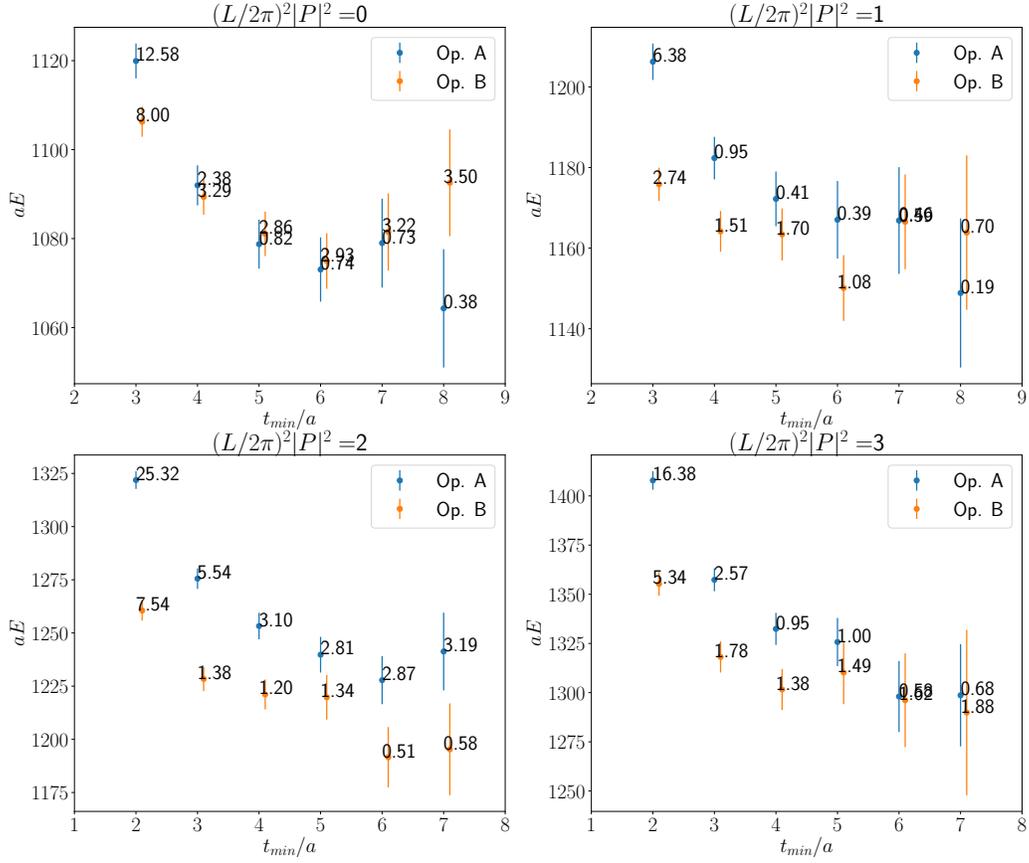
Figure 5.5 Stability fit for the 2 nucleon correlators type at various $(\frac{L}{2\pi}|P|)^2$. The fit function is a single exponential and is applied to the range from t_{min} to $t_{max} = 14$. χ^2/ndf is listed at points.
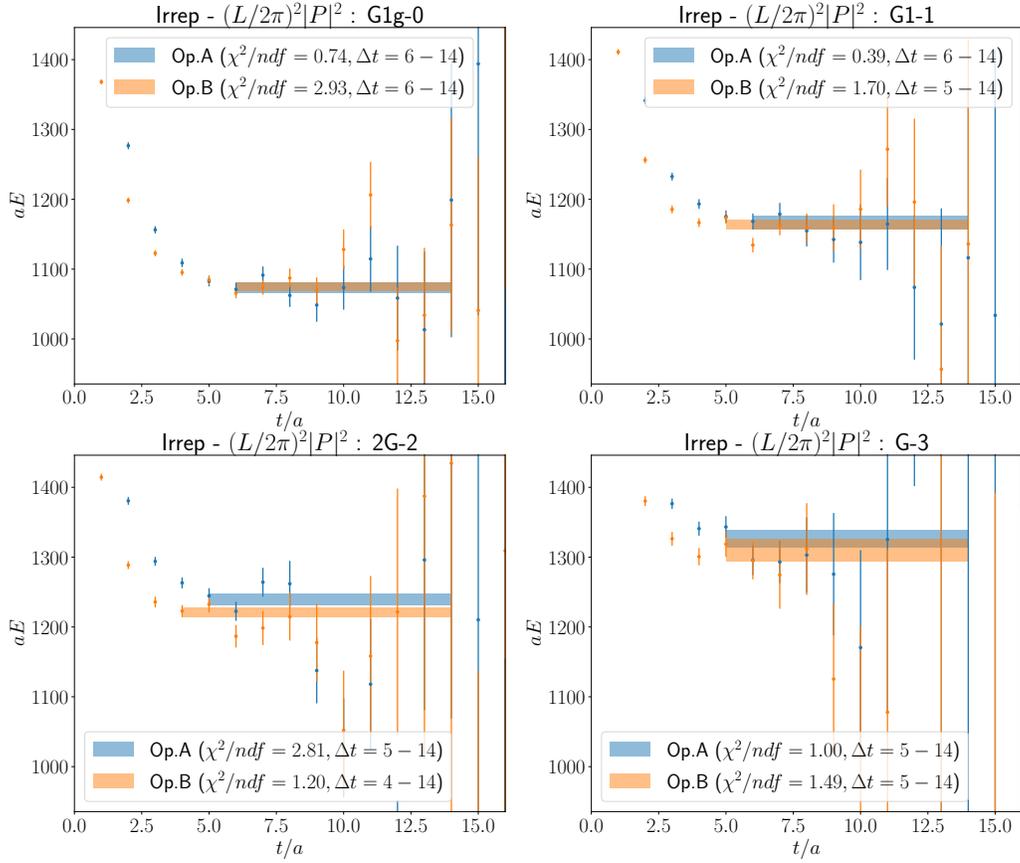
Figure 5.6 Effective mass of the nucleon correlators with fit result (choice of time range shown in the legend).
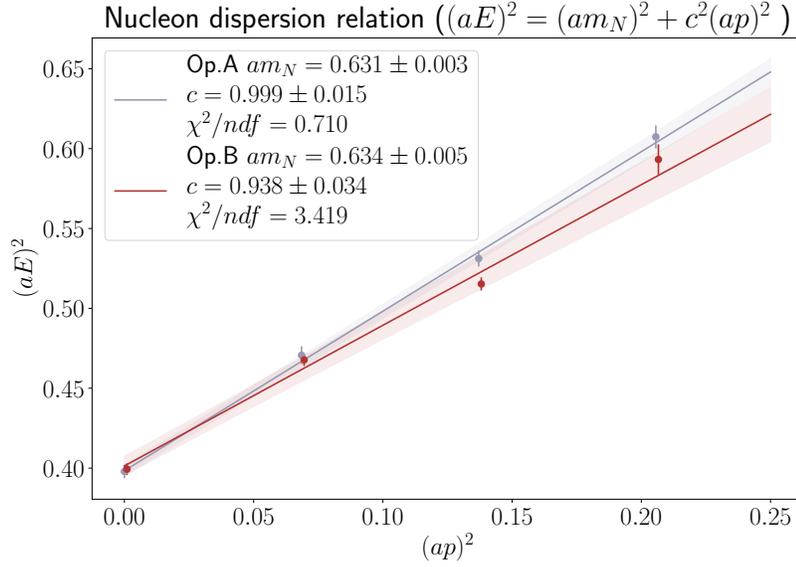
Figure 5.7 Dispersion relation of the nucleon for the two operators A and B.

of the chosen value. Thus, $t_{max} = 14$ for all fits, while limiting the variation of fit range to the lower limit t_{min}. The stability analysis shows the operator "B" having the plateau onset at earlier times, indicating smaller high-energy state pollution.

In Fig. 5.6 we show the effective mass plot for all correlators at different momenta with the fits superimposed. The energy points for both correlators are fitted with the dispersion relation $(aE)^2 = (am_N)^2 + c^2(ap)^2$, as shown in Fig. 5.7.

The results of the fits are:

- "A": $am_N = 0.631 \pm 0.003$, $c = 0.999 \pm 0.015$, $\chi^2/ndf = 0.710$

- "B": $am_N = 0.634 \pm 0.005$, $c = 0.938 \pm 0.034$, $\chi^2/ndf = 3.419$

where the nucleon mass is consistent among the two fits.

GEVP analysis of the nucleon

We also implement the Generalized Eigenvalue Problem method (GEVP) [93, 94] to improve the signal for the ground state. The two correlators of the nucleon are combined in 2-by-2 correlation matrices for each frame and run through a GEVP analysis. The choice of t_0 has a limited impact once it is chosen small enough; we set $t_0 = 2$. Applying the same analysis steps from the previous section, we run an exponential fit for multiple time range and search for a plateau. The stability fit is presented in Fig. 5.8, where we fix $t_{max} = 16$ and vary t_{min}. The fit choice for the time range gives the energy levels shown in the effective mass plot in Fig. 5.8. As previously, the energy levels extracted are used in the dispersion relation fit (shown in Fig. 5.9) for which we obtain the results:
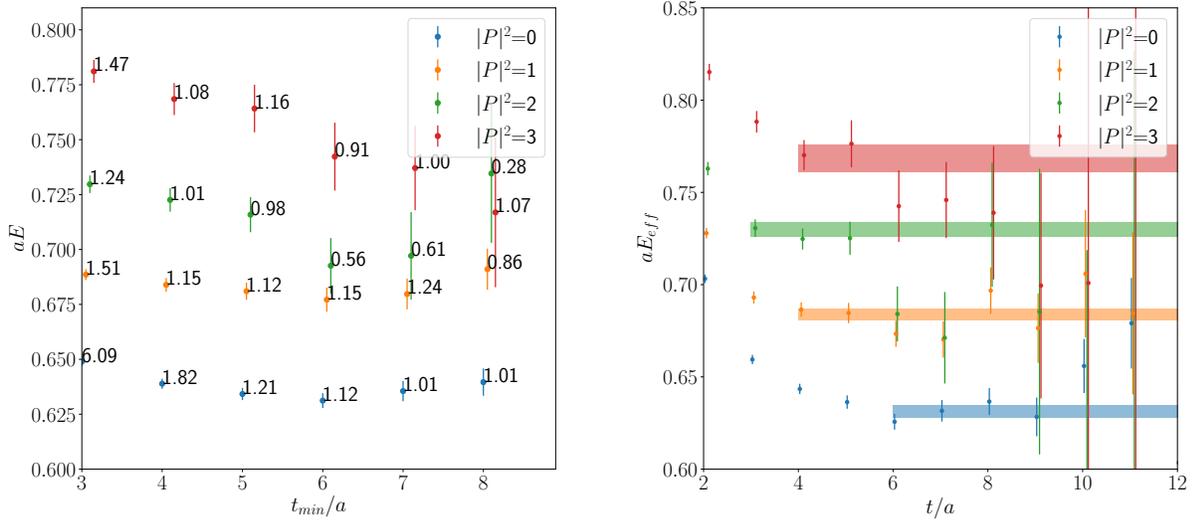
Figure 5.8 Left panel: (GEVP) stability fit for the nucleon correlators at various $(\frac{L}{2\pi}|P|)^2$. The fit function is a single exponential and is applied to the range from t_{min} to $t_{max} = 16$ (χ^2/ndf is listed at points). Right panel: effective mass of the nucleon correlators with fit result ($t_{max} = 16$).
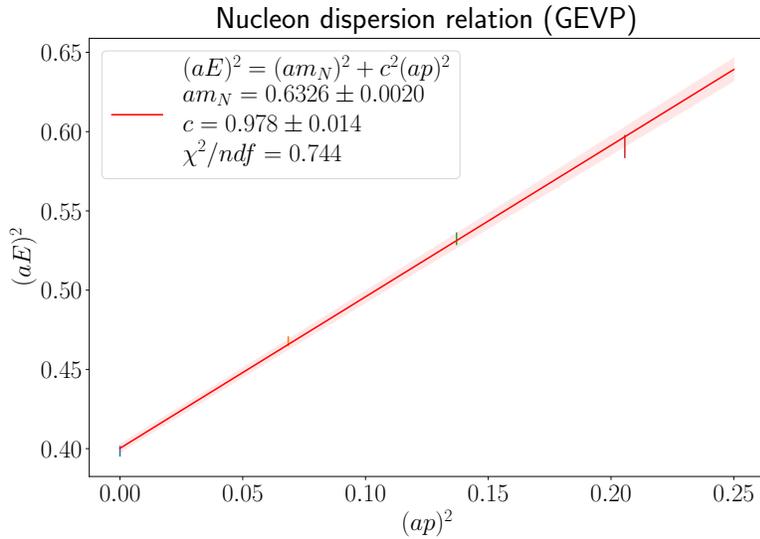
Figure 5.9 GEVP analysis: Dispersion relation of the nucleon.
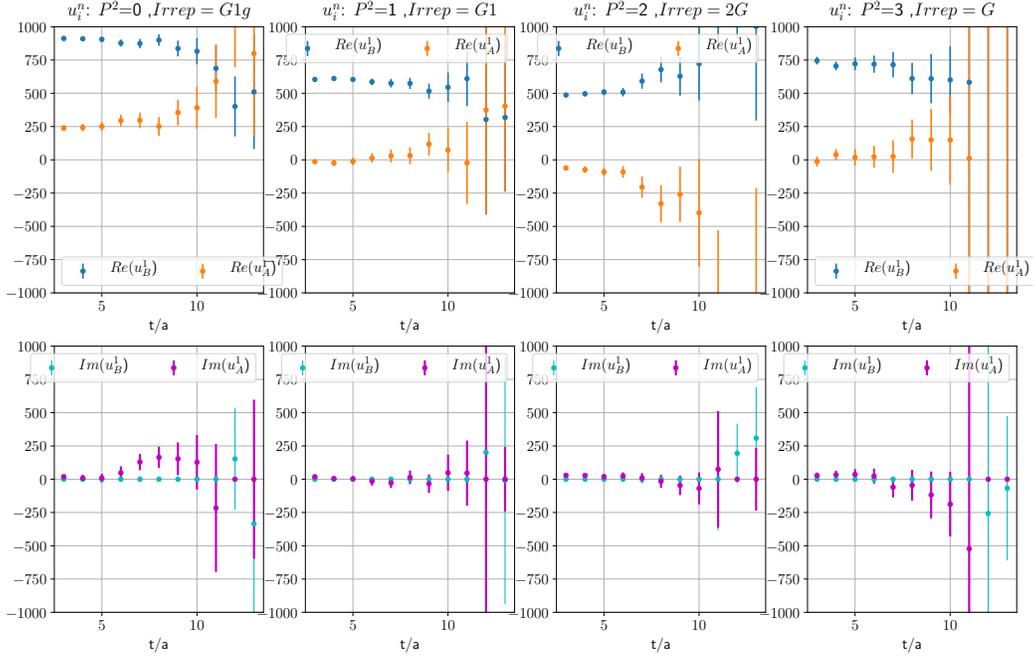
Figure 5.10 Real and imaginary parts of the eigenvectors u_i^n in each frame.

- $am_N = 0.6326 \pm 0.0020$, $c = 0.978 \pm 0.014$, $\chi^2/ndf = 0.744$,

consistent with the mass results from the previous nucleon fits. We then use this value for the nucleon mass in the parametrization of the phase shift fit.

Optimized interpolator for the Nucleon

From the projected nucleon operators $N_i^{\Lambda,r,n}(\vec{P})$ we implement an optimal interpolator [95, 93, 96, 94],

$$\mathcal{N}^{\Lambda,r,n}(\vec{P}) = \sum_i u_i^{n,\Lambda,\vec{P}}(t) N_i^{\Lambda,r,n}(\vec{P}) \tag{5.9}$$

where the generalized eigenvectors $u_i^{n,\Lambda,\vec{P}}$ (for $t/a = 4$) derive from the generalized eigenvalue problem,

$$C_{ij}^{\Lambda,\vec{P}}(t) u_j^n(t) = \lambda^n(t,t_0) C_{ij}^{\Lambda,\vec{P}} u_j^n(t) \tag{5.10}$$

of the correlation matrix from two nucleon operator $N^{(1,2)}$. The chosen eigenvectors u_i^n (at $t/a = 4$ in Fig. 5.10), respect the orthogonalities relations,

$$(u_i^{n*} Z_i^m) e^{-E_n t_0/2}/\sqrt{2E_n} = \delta_{nm} \tag{5.11}$$

and

$$\sum_m (u_i^{n*} Z_i^m) \frac{e^{-E_m t_0}}{2E_m} (Z_j^{m*} u_j^k) = \delta_{nk} \tag{5.12}$$

where $Z_i^n = \sqrt{2E_n}e^{E_n t_0/2}C_{ij}(t_0)u_j^n$ are the overlap factors.

This makes for an optimized multi-hadron $\mathcal{N}\pi$ interpolator that has a dominant overlap to a single well-defined state labeled with $(n, \vec{P}, \Lambda, r)$ [97], while also halving the number of nucleon-pion operators employed in the correlation matrices.

5.3 Spectra results: $\Delta - N\pi$

The central part of the analysis deals with the extraction of the energies from the matrix of correlators of single-hadron Δ and multi-hadron $N\pi$ through variational methods [98]. The Δ and N operators come with two different types of gamma structures. For the nucleon, we employ a linear combination (outlined in Sec. 5.2.2) of the two N operators to improve the $N\pi$ overlap of the multi-hadron states.

The first step is to project the Δ single-hadron correlators as outlined in Sec. 3.3.1 and multi-hadron correlators, as explained in Sec. 3.3.2. A clear difference between the two types arises in the degrees of freedom when it comes to momentum content. For a given total momentum P_{tot}, the multi-hadron operator can vary within the momenta combination of the two particles, with a fixed modulus of each momentum $|\vec{p}_\pi|$ and $|\vec{p}_N|$ (and also $\vec{p}_\pi + \vec{p}_N = \vec{P}_{tot}$). The Lüscher quantization condition works best for elastic processes, and we aim to measure spectra in the energy region between the $N\pi$ and $N\pi\pi$ thresholds, as well as nearly above. From the energy location of the non-interacting energy levels, we choose to limit the multi-hadrons' momenta content to not significantly exceed the upper threshold ($N\pi\pi$). In general, the energy levels from the non-interacting spectra loosely map the location of the interacting ones. Nevertheless, it can be used to outline a hierarchy of levels, allowing us to choose a momentum content that locates the operators in (or near) the region of interest. As a general rule, we set the $N\pi$ momenta limited to $|\vec{p}_\pi| + |\vec{p}_N| \leq \sqrt{3}\frac{2\pi}{L}$. The cut-off saves us machine time and reduces the operator's list to a reasonable size for the GEVP analysis step. Tab. 3.7 lists the momenta content used for the nucleon-pion operators in each frame (and irrep). For each irrep, correlation matrices are computed for each row r and total momentum of the system $\vec{P}_{tot}$ and subsequently averaged to increase statistic [99].

Given the relatively large number of operators employed, we try to reduce the list of operators in the basis without losing energy levels in the spectra with respect to the full basis. For every correlation matrix, various subsets of the full basis of operators are analyzed via GEVP and Singular Value Decomposition (SVD). Through SVD the correlation matrices $C_{ij}^{\Lambda,\vec{P}}$ can be decomposed in eigenvalues (singular values) and eigenvectors of CC^* and C^*C. While differing from an eigenvalue decomposition of $C_{ij}^{\Lambda,\vec{P}}$, this can nevertheless help us in assessing the operators contributing to the largest singular values and thus exploring sub-basis of the full list of operators that can have reduced noise on the correlators while maintaining the complete spectra. In other words, the use of the SVD method helps identify the more relevant operators overlapping with each energy level and, thus, discarding the less important ones.

The remainder of the section presents the spectra results for the correlation matrices from each of the irreps relevant to this study. Our spectra results are obtained from single-exponential fits to the principal correlators and are listed in Table 5.2. In addition, we

estimate a systematic uncertainty for each energy level as the shift in the fitted energy when increasing $t_{\min}/a$ by $+1$. These uncertainties have been added in quadrature in the lighter-shaded outer bands shown in Figs. 5.11, 5.12, 5.13, 5.14, 5.15, 5.16, 5.17, and will also be propagated to the scattering amplitudes.

5.3.1 Group: O_h^D , Irrep: G_{1u}
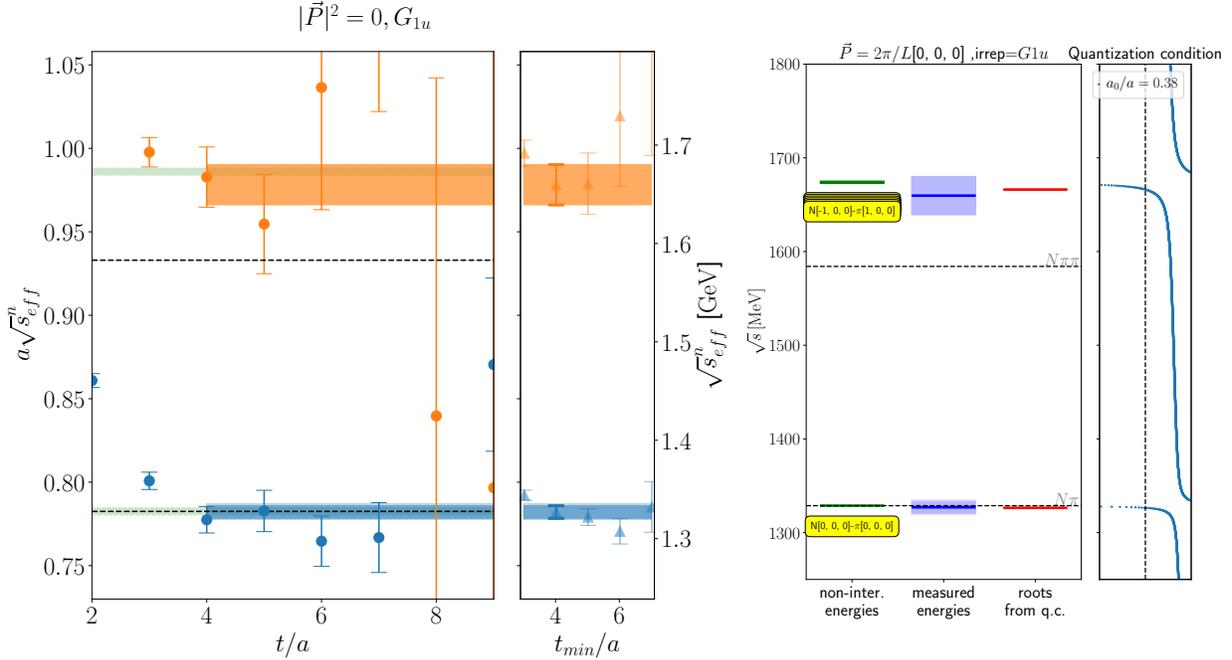
(a) Effective energies and stability fits in single-exp. **(b)** Spectra for irrep G_{1u}.

Figure 5.11 Irrep G_{1u}: (a) Effective energies of the principal correlators as a function of t/a (left), and the energies obtained from single-exponential fits to these correlators as a function of t_{min}/a ($t_{max}/a = 15$). (b) Non-interacting energies compared to the measured energies from fits to the principal correlators, and roots in the quantization condition for this irrep (shown on the right panel) for the global multi-irrep phase shift fit **G(a)**.

As shown in Tab. 3.3, this irrep is the only one that has an S-wave ($J = 1/2$) contribution without the P-wave ($J = 3/2$) (higher partial waves are not considered here). Given the parity quantum number for nucleon-pion in S-wave, the only irrep able to measure such contribution would be the odd parity (*ungerade*). It is expected to be populated only by $N\pi$ levels (in our region of interest) for which a shift in the energy of the non-interacting levels parametrizes a phase shift contribution from a distant resonance with $J = 1/2$ (at physical pion mass this resonance would locate at ~ 1620 MeV). The correlation matrix is composed of a total of three optimized $N\pi$ operators. We apply the GEVP method to the correlation matrix (with $t_0 = 2$) and subsequently fit the principal correlators for various

t_{min} using single-exponential functions in Eq. (5.5) (we show the values of E_n in Fig. 5.11).
Fig. 5.11(a) also shows the two (lowest) non-interacting $N\pi$ energy levels, which largely
overlap with the "interacting" energies measured. This can be interpreted as a sign of small
(or no) contribution from the phase shift belonging to this irrep. In Fig. 5.11(b) we show the
roots from the quantization condition for the global phase shift fit compared to the energy
levels extracted from correlator fits. Also visible are the non-interacting energies computed
from the momenta of the $N\pi$ system.

5.3.2 Group: O_h^D , Irrep: H_g
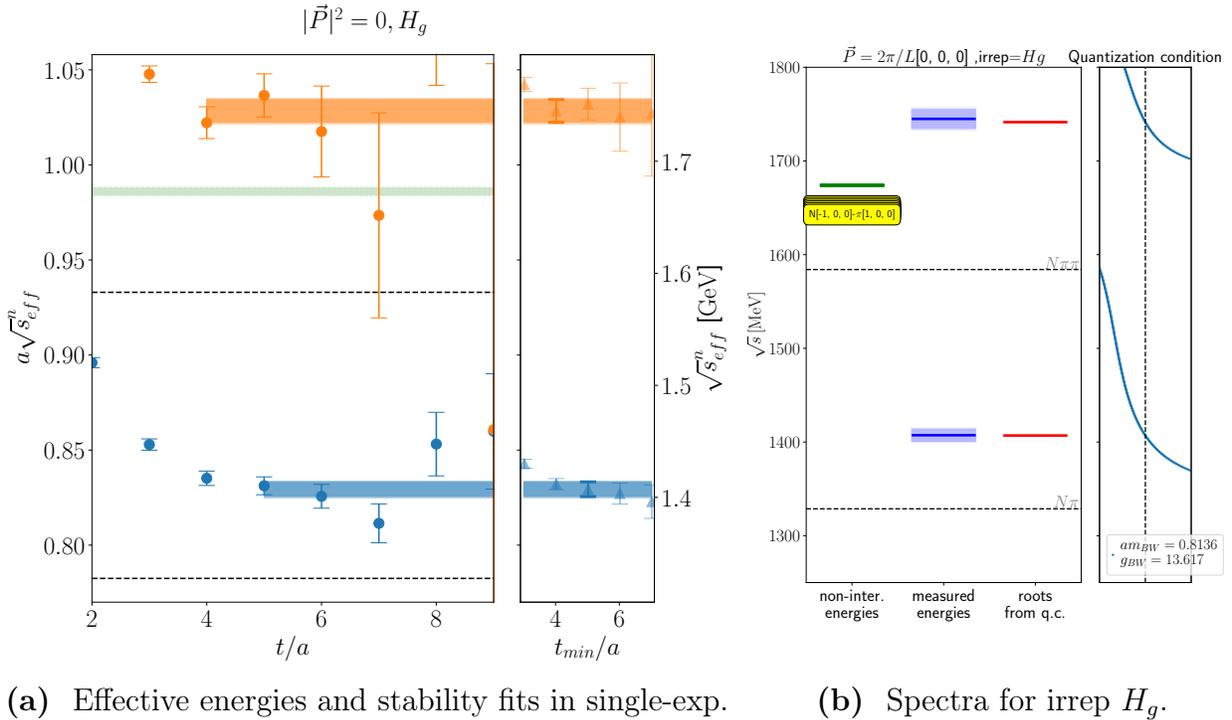
(a) Effective energies and stability fits in single-exp.

(b) Spectra for irrep H_g.

Figure 5.12 Irrep H_g: (a) Effective energies of the principal correlators as a func-
tion of t/a (left), and the energies obtained from single-exponential fits to these
correlators as a function of t_{min}/a ($t_{max}/a = 15$). (b) Non-interacting energies com-
pared to the measured energies from fits to the principal correlators, and roots in
the quantization condition for this irrep (shown on the right panel) for the global
multi-irrep phase shift fit **G(a)**.

In general, the rest frame offers the clearest distinction between angular momenta J
among different irreps, and the main focus of this study, the $J = 3/2$ contribution, lies in
the irrep H_g (also H_u, but it is of opposite parity of what we are interested). In contrast
with the previous irrep G_{1u}, the multi-hadron operator $N\pi$ projected in this irrep does not
appear at rest, i.e. both momentum for nucleon-pion at zero, due to the dynamics of the
system in the context of parity. Following the upper limit on momentum onto the individual

particles, this leaves us with a single momentum configuration for the two-hadron system $N\pi$, i.e., $|\vec{p}_\pi| = |\vec{p}_N| = 2\pi/L$.

The correlation matrix that connects all operators of this irrep is run through the GEVP method for a fixed $t_0 = 2$. We fit over the principal correlators on various time ranges using the single exponential function of Eq. (5.5), as shown in Fig. 5.12(a). The two levels measured appear relatively stable among the different sets of fit ranges. As expected, the rest frame yields the most precise signals among the different frames. The ground state clearly shows remarkable stability and a large plateau, especially considered that we are dealing with baryons. The final choice for t_{min}/a in the fit is shown in Fig. 5.12(a) along with the values in energies extracted for each level . In Fig. 5.12(b) the roots from the quantization condition for the global phase shift fit are compared to the energy levels extracted from correlator fits and the non-interacting energies.

5.3.3 Group: C_{4v}^D , Irrep: G_1
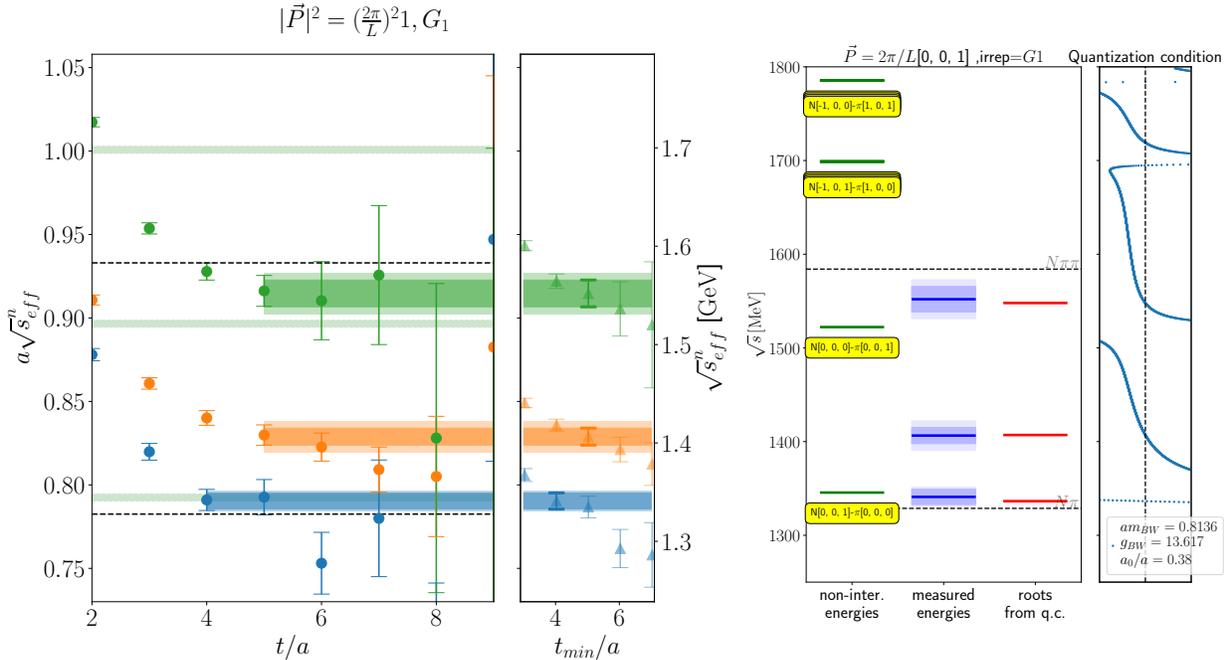
(a) Effective energies and stability fits in single-exp.

(b) Spectra for irrep G_1.

Figure 5.13 Irrep G_1: (a) Effective energies of the principal correlators as a function of t/a (left), and the energies obtained from single-exponential fits to these correlators as a function of t_{min}/a ($t_{max}/a = 15$). (b) Non-interacting energies compared to the measured energies from fits to the principal correlators, and roots in the quantization condition for this irrep (shown on the right panel) for the global multi-irrep phase shift fit **G(a)**.

The moving frame with total momentum of $\vec{P}_{tot} = 2\pi/L$ is described by the symmetry group C_{4v}^D. The irrep G_1 originates from the subduction of the (rest frame) irreps $H_{g/u}$ and

$G_{1g/u}$. Thus, it inherits both angular momenta: $J = 3/2$ and $J = 1/2$. As listed in Tab. 3.7 for the two hadron operator $N\pi$, we implement a set of four momenta combinations. Also, the operators projected in this irrep have a high multiplicity, resulting in four occurrences for each of the two types of single hadron Δ operators and up to 12 for $N\pi$ (see Tab. 3.7). As a result, even after combining the two N operators with different gamma structures in a single optimized operator for $N\pi$, we have a correlation matrix of size 20 by 20. We run a GEVP analysis for several different subsets of operators from this fairly large correlation matrix, looking for an optimal signal in the principal correlators. We do this analysis while comparing each subset result with the full-basis of correlators, aiming to extract a good signal with low noise while keeping the number of levels extracted equals to the full-basis. The stability fit analysis results are shown in Fig. 5.13(a) for the three levels extracted. The final choice of t_{min} for each fit is shown in the effective mass plot in Fig. 5.13(a) with the associated energies, and compared in Fig. 5.13(b) to the roots of the quantization condition computed from the global phase shift fit results.

5.3.4   Group: C_{4v}^D , Irrep: G_2
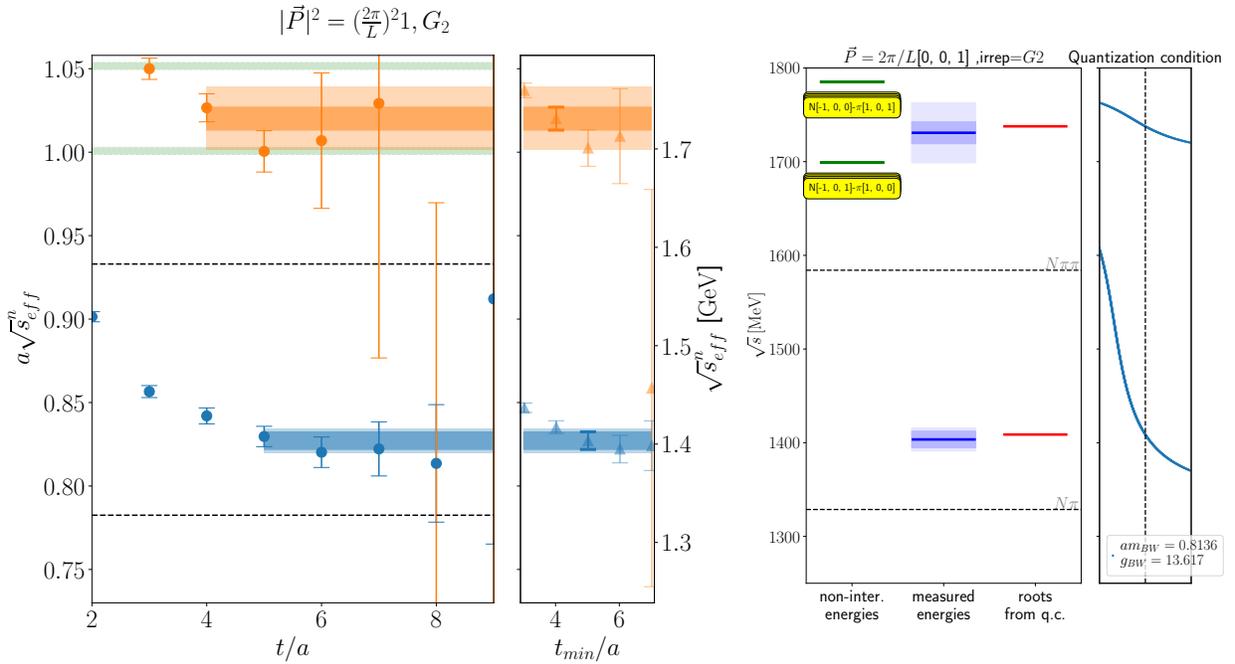
(a) Effective energies and stability fits in single-exp.   **(b)** Spectra for irrep G_2.

Figure 5.14 Irrep G_2: (a) Effective energies of the principal correlators as a function of t/a (left), and the energies obtained from single-exponential fits to these correlators as a function of t_{min}/a ($t_{max}/a = 15$). (b) Non-interacting energies compared to the measured energies from fits to the principal correlators, and roots in the quantization condition for this irrep (shown on the right panel) for the global multi-irrep phase shift fit **G(a)**.

The irrep G_2 belongs to the same group of G_1 but differs in the subduction from the rest frame's irreps. The critical difference is that it is subduced only from H_g, as shown in Tab. 3.4. This makes G_2 a "cleaner" irreps because it contains $J = 3/2$ spin without $J = 1/2$ (the same is true for H_g, F_1, F_2). This absence makes it a suitable candidate for an initial phase shift fit that would try to parametrize the $J = 3/2$ contribution alone (without $J = 1/2$). The multiplicity is double for the single Δ operator and quadruple for each $N\pi$ operator (shown in Tab. 3.7). A 12 by 12 correlation matrix is analyzed with the GEVP method to find the operators' optimal sublist that yields a cleaner signal. The correlators provided by this subgroup are then fitted using single exponential stability fit analysis, as shown in Fig. 5.14(a) for two energy levels. Once again, the comparison with the roots from quantization condition from global fit is shown in Fig. 5.14(b).

5.3.5 Group: C_{2v}^D , Irrep: $(2)G$
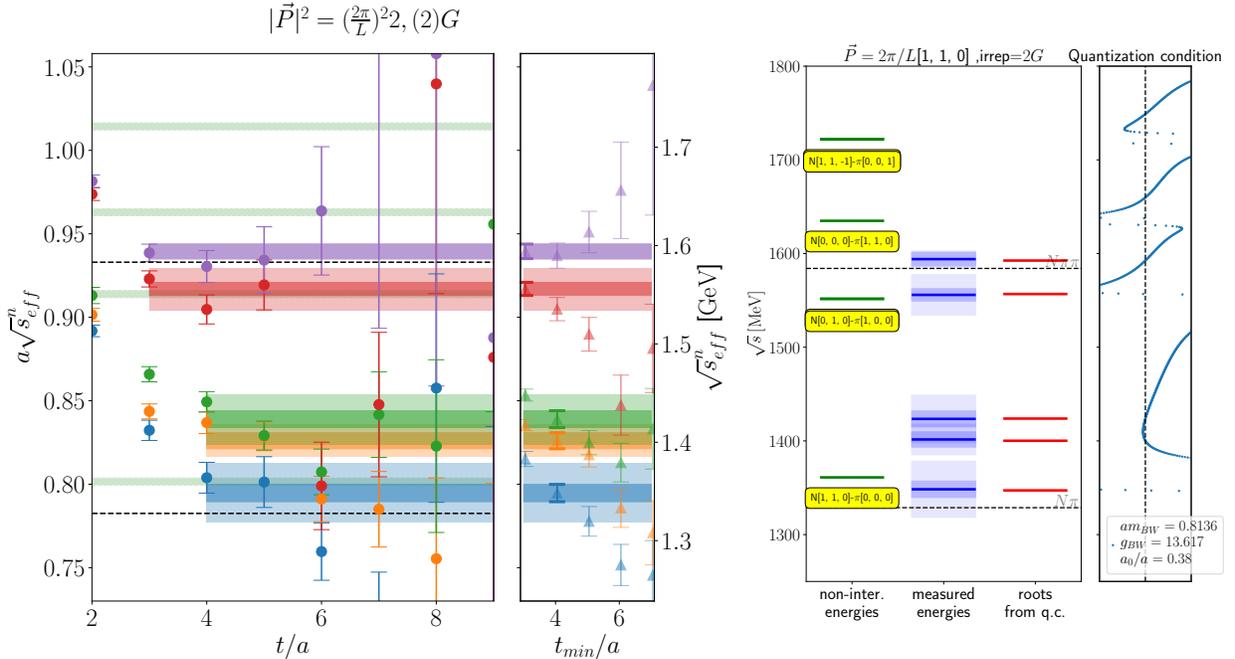
(a) Effective energies and stability fits in single-exp.   **(b)** Spectra for irrep G.

Figure 5.15 Irrep $(2)G$: (a) Effective energies of the principal correlators as a function of t/a (left), and the energies obtained from single-exponential fits to these correlators as a function of t_{min}/a ($t_{max}/a = 15$). (b) Non-interacting energies compared to the measured energies from fits to the principal correlators, and roots in the quantization condition for this irrep (shown on the right panel) for the global multi-irrep phase shift fit **G(a)**.

For the boosted frame with $|\vec{P}| = (2\pi/L)\sqrt{2}$, the double group associated with half-integer spin is C_{2v}^D. There is only the irrep $(2)G$ in this group, which contains all half-integer

angular momenta J. The presence of only a single irrep results from the low symmetry of the boosted grid, also compared to the other frames (boosted or at rest). The presence of a single irrep maximizes the number of occurrences for the projected operators. As an example, the single-hadron Δ for a fixed row projects to six independent occurrences. Also, the multihadron $N\pi$ shows double or quadruple occurrences among different momenta combination. The correlation matrix averaged over momenta direction, rows, and optimized nucleon interpolator is a 20 by 20 matrix. For this irrep, we observe in the range of energies of interest a high number of levels, and, through the GEVP method, we extract five. Shown in Fig. 5.15(a) is the stability fit analysis for these five levels in the clearest sub-group of operators extracted. Given the high number of levels and the higher total momentum associated, the plateau regions become harder to pin and start to move at earlier times. The fit range choices are plotted in the effective mass plot in Fig. 5.15(a), where for the two highest levels, we choose to set the lower bound of the range to $t_{min}/a = 3$.

5.3.6   Group: C_{3v}^D , Irrep: G
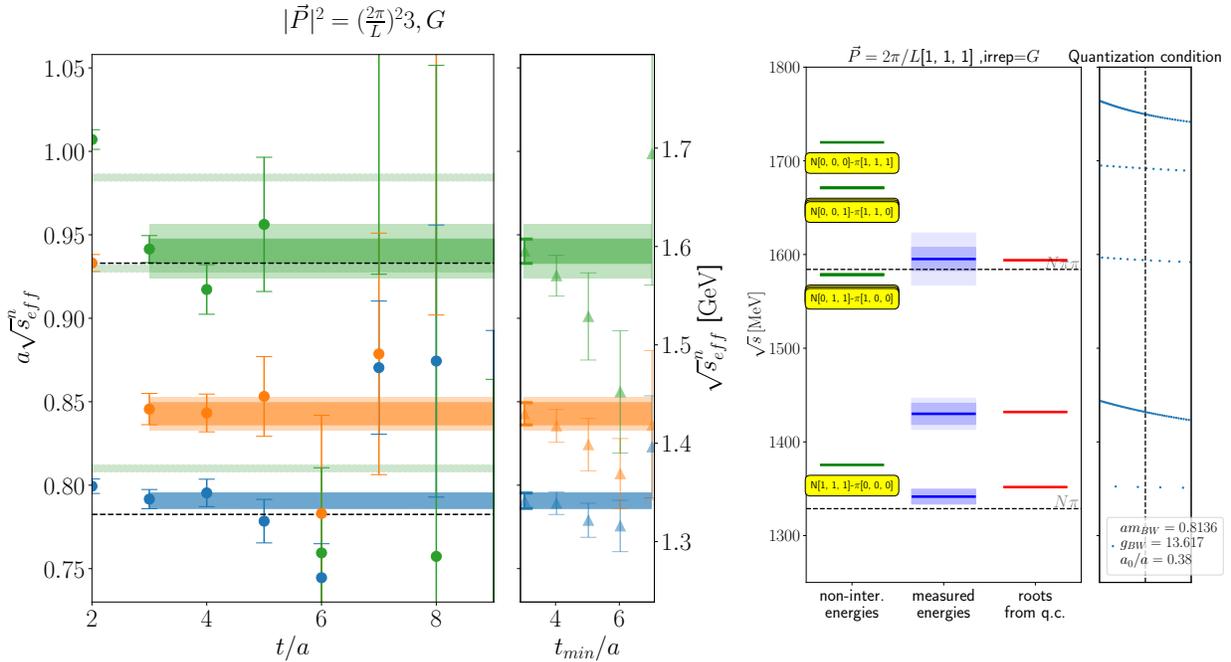
(a) Effective energies and stability fits in single-exp.

(b) Spectra for irrep G.

Figure 5.16 Irrep G: (a) Effective energies of the principal correlators as a function of t/a (left), and the energies obtained from single-exponential fits to these correlators as a function of t_{min}/a ($t_{max}/a = 15$). (b) Non-interacting energies compared to the measured energies from fits to the principal correlators, and roots in the quantization condition for this irrep (shown on the right panel) for the global multi-irrep phase shift fit **G(a)**.

The highest boosted frame we consider has $|\vec{P}| = (2\pi/L)\sqrt{3}$, and the group C_{3v}^D contains

71

three irreps for half-integers spin. Here we consider the 2-dimensional irrep G. The single Δ operator has multiplicity $m = 4$, and the $N\pi$ operators have double or quadruple occurrences for different momenta combinations, as listed in Tab. 3.7. After averaging over rows and total momentum direction, we run the 20 by 20 correlation matrix in the GEVP analysis, once again with the pursuit of identifying a good operators basis among the vast choice available. The results of this investigation are then analyzed with stability fits, shown in Fig. 5.16(a), for various t_{min}/a and a fixed $t_{max}/a = 15$. The final range choices are set to $t_{min}/a = 3$ for the three levels. Fig. 5.16(a) shows the measured energy levels alongside the correlators effective mass. These high-momentum frame shows, as predicted, an increase in statistical noise.

5.3.7 Group: C_{3v}^D , Irrep: F_1, F_2

The irreps F_1 and F_2 both belong to the double group C_{3v}^D and are both unidimensional, i.e., they have a single row. Subduced from irrep $H_{g/u}$ in the rest frame, they possess the same spin content, free of $J = 1/2$ (as in the case of G_2). They are also used to perform the initial phase shift fit for a $\delta_{3/2,1}$ together with the levels extracted from H_g and G_2. There is a double occurrence for both the single Δ and the two-hadron $N\pi$ operator. From the list of operators outlined in Tab. 3.7, we have an eight by eight correlation matrix for every total momentum direction $\vec{P}$. After averaging over momentum directions, we repeat the GEVP analysis for several operators' sub-sets to find the most stable signal for the principal correlators. As in every other irrep, the final choice is then analyzed through single exponential fits of the principal correlators, as outlined in the left panels of Fig. 5.17 for irrep F_1 and F_2. The irrep F_2 shows a slightly better behavior, clearly visible in more stable fits over different choice of t_{min}/a. The effective energies plot together with the final fits are also shown in the left panels. Panels on the right of Fig. 5.17, shows the comparison between non-interacting energies, measured energies, and roots of the quantization condition. The roots for the irreps (in red) are found from the quantization condition computed from the multi-irrep global phase shift fit results $\mathbf{G(a)}$, shown in Tab. 5.3. The measured energies (blue) represent the value of E_n from the chosen single exponential fit of the principal correlators from the GEVP analysis.
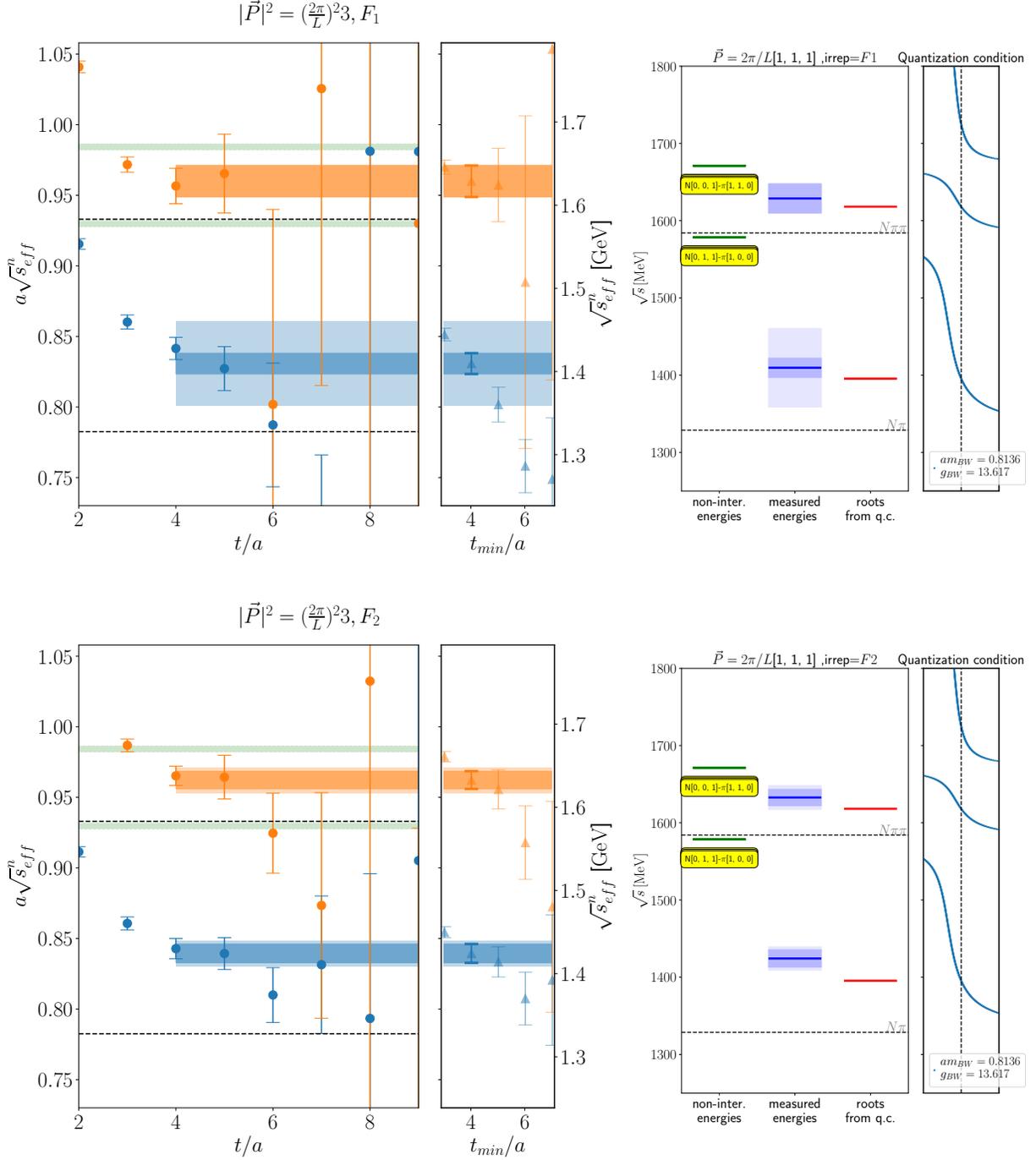
Figure 5.17 Irreps F_1, F_2: (Left panels) Effective energies of the principal correlators as a function of t/a (left), and the energies obtained from single-exponential fits to these correlators as a function of t_{min}/a ($t_{max}/a = 15$). (Right panels) Non-interacting energies compared to the measured energies from fits to the principal correlators, and roots in the quantization condition for this irrep (shown on the right panel) for the global multi-irrep phase shift fit **G(a)**.

73

5.4 Results for the scattering amplitudes
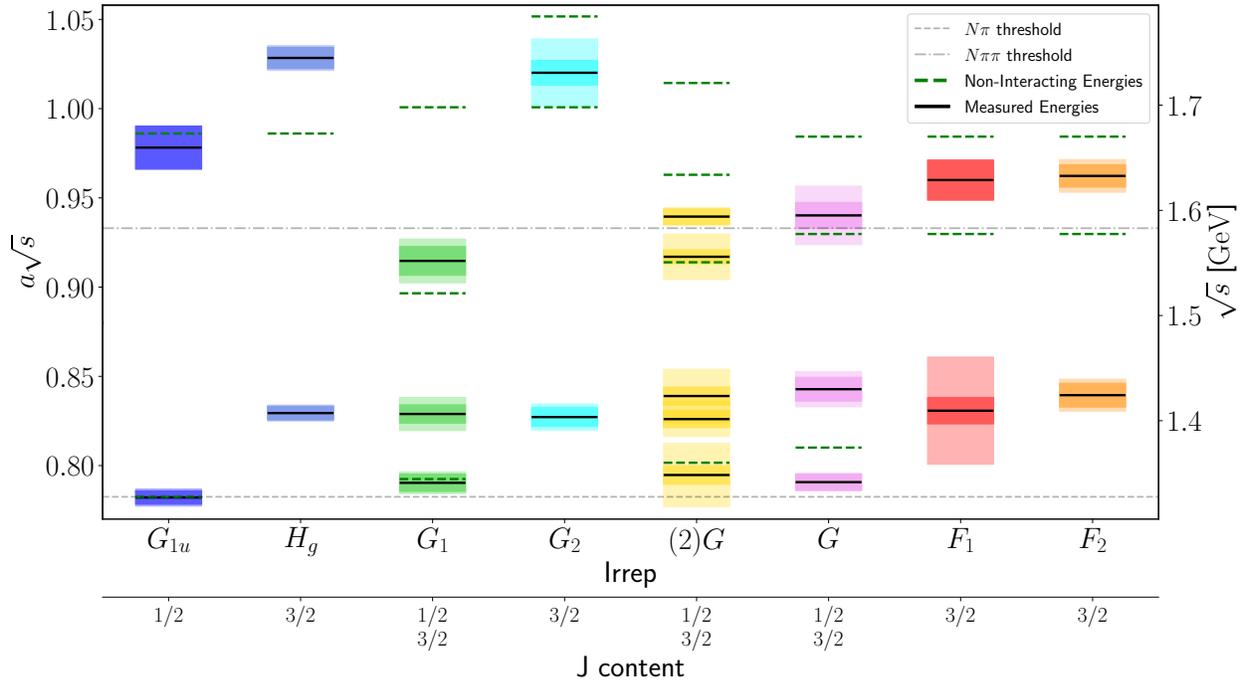
Figure 5.18 Center of mass energies from all irreps used, alongside the $N\pi$ non-interacting energy levels. Also, $J \leq 3/2$ content is listed for each irrep. The inner bands indicate the statistical and scale-setting uncertainties. The outer, lighter-shaded bands include an estimate of the systematic uncertainty asssociated with the choice of fit range, calculated from the change in the fitted energy when increasing t_{min}/a by $+1$.

Fig. 5.18 shows a summary of all CMF energy levels obtained from the correlators, divided into irreps, as well as the J content for each irrep that guides the choice for the phase shift fits. In Tab. 5.2 we list the CMF energies from the correlator fits with fit range and χ^2/dof for all energy levels.

In principle, there are infinitely many values of total angular momentum J and therefore also infinitely many partial waves l in each irrep, but, as the higher waves have an increasingly smaller contribution, we consider only the dominant partial waves. In particular, we assume the contributions from partial waves in $J > 3/2$ to be negligible and exclude them from the analysis.

The primary goal of the phase shift fit is to measure the $J = 3/2$ contribution (in P-wave), but since some irreps mix with $J = 1/2$, the latter is also included in the quantization conditions used in the fits. In particular, for partial wave $J = 1/2$ the contribution in S-wave ($l = 0$) is expected to be dominant over the P-wave ($l = 1$). At our level of precision, we find the former to be consistent with zero, and thus, decide to not include the latter.

To summarize, we proceed to parametrize two contributions in the phase shift fit: the resonant P_{33} wave[2] (also called $\delta_{3/2,1}$) and the non-resonant S_{31} wave (or $\delta_{1/2,0}$).

In the region of interest, we expect the P_{33} wave to measure mainly the onset of the resonance $\Delta(1232)$ and for the S_{31} wave to measure a small phase shift from the distant $\Delta(1620)$.

Breit-Wigner

In general, if the resonance is narrow (as it is for the $\Delta(1232)$), it is useful to express the transition amplitude $T^{(l)}$ through the Breit-Wigner parametrization.

$$T^{(l)} = \frac{\sqrt{s}\,\Gamma(s)}{m_{\text{BW}}^2 - s + i\sqrt{s}\,\Gamma(s)} \tag{5.13}$$

where $\Gamma(s)$ is the decay width and m_{BW} represents the (Breit-Wigner) resonance mass. This parametrization is generally used only in the vicinity of the resonances. We use the Breit-Wigner model to describe the phase shift $\delta_{3/2,1}$ ($J = 3/2, l = 1$) that measure the onset of the resonance $\Delta(1232)$.

In particular, we implement the K-matrix formalism (Sec. 2.5), for which the Breit-Wigner has the form,

$$\hat{K}_{ij}^{(3/2,1)} = \frac{\sqrt{s}\,\Gamma(s)}{(m_{\text{BW}}^2 - s)\sqrt{\rho_{ii}\rho_{jj}}}, \tag{5.14}$$

where ρ_{ij} represents the phase space matrix outlined in Eq. (2.39). For our case of only one channel we have $i, j = 0$ and it reads,

$$\rho_{00} = \sqrt{\left(1 - \left(\frac{m_\pi + m_N}{\sqrt{s}}\right)^2\right)\left(1 - \left(\frac{m_\pi - m_N}{\sqrt{s}}\right)^2\right)} \tag{5.15}$$

Also, $\Gamma(s)$ is defined as:

$$\Gamma(s) = \frac{g_{\text{BW}}^2}{6\pi}\frac{k^3}{s}, \tag{5.16}$$

with g_{BW} representing the coupling.

Effective Range Expansion

The other phase shift we aim to extrat, i.e. $\delta_{1/2,0}$ (($J = 1/2, l = 0$)), is expected to be non-resonant in the region of interest. We can parametrize it with the effective range expansion (ERE) at order 0,

$$\hat{K}_{00}^{(1/2,0)} = \frac{k}{\rho_{00}}(a_0), \tag{5.17}$$

where a_0 is the zero-energy scattering length.

---

[2]the nomenclature indicates the type of wave S, P, D, etc, and the values for $I \times 2$ and $J \times 2$

$(\frac{L}{2\pi})^2|\vec{P}|^2$	Λ	n	Fit Range	$\frac{\chi^2}{\text{dof}}$	$a\sqrt{s_n^{\Lambda,\vec{P}}}$
0	G_{1u}	1	$4-15$	1.90	0.782(4)(3)
0	G_{1u}	2	$4-15$	0.80	0.978(12)(1)
0	H_g	1	$5-15$	1.79	0.829(4)(2)
0	H_g	2	$4-15$	0.43	1.028(6)(4)
1	G_1	1	$4-15$	1.97	0.790(5)(4)
1	G_1	2	$5-15$	1.14	0.829(5)(8)
1	G_1	3	$5-15$	0.72	0.914(8)(9)
1	G_2	1	$5-15$	0.48	0.827(5)(5)
1	G_2	2	$4-15$	0.89	1.020(7)(18)
2	$(2)G$	1	$4-15$	1.73	0.795(5)(17)
2	$(2)G$	2	$4-15$	1.72	0.826(5)(8)
2	$(2)G$	3	$4-15$	1.60	0.839(5)(14)
2	$(2)G$	4	$3-15$	1.87	0.917(4)(12)
2	$(2)G$	5	$3-15$	0.71	0.939(4)(3)
3	G	1	$3-15$	1.32	0.791(5)(2)
3	G	2	$3-15$	0.68	0.843(7)(7)
3	G	3	$3-15$	2.01	0.940(7)(15)
3	F_1	1	$4-15$	1.46	0.831(7)(29)
3	F_1	2	$4-15$	0.27	0.960(11)(3)
3	F_2	1	$4-15$	0.45	0.839(7)(6)
3	F_2	2	$4-15$	0.56	0.962(6)(7)

Table 5.2 Center-of-mass energies results in the $\Delta - N\pi$ sector from single-exponential fits to the principal correlators, for the total momenta $\vec{P}$, and irreps Λ. The first uncertainty is statistical and the second uncertainty is systematic, given by the shift in the fitted energy when increasing t_{min} by one unit.

Label	Fit (J,l)	irreps Λ	points	Breit-Wigner	ERE a_0	χ^2/dof
S	$(1/2,0)$	G_{1u}	2	-	0.51(96)	0.16
P	$(3/2,1)$	H_g, G_2, F_1, F_2	8	$g_{\mathrm{BW}} = 13.36(80)$ $m_{\mathrm{BW}} = 0.8158(31)$ $corr(am_{\mathrm{BW}},g_{\mathrm{BW}})=-0.279$	-	1.35
G(a)	$(1/2,0)$ $(3/2,1)$	$G_{1u}, H_g, G_1, G_2,$ $(2)G, G, F_1, F_2$	21	$g_{\mathrm{BW}} = 13.62(50)$ $m_{\mathrm{BW}} = 0.8136(29)$ $corr(am_{\mathrm{BW}},g_{\mathrm{BW}})=-0.375$	0.38(44)	0.85
G(a+1)	$(1/2,0)$ $(3/2,1)$	$G_{1u}, H_g, G_1, G_2,$ $(2)G, G, F_1, F_2$	21	$g_{\mathrm{BW}} = 14.05(83)$ $m_{\mathrm{BW}} = 0.8088(43)$ $corr(am_{\mathrm{BW}},g_{\mathrm{BW}})=-0.442$	0.46(80)	0.99
G(b)	$(1/2,0)$ $(3/2,1)$	$G_{1u}, H_g, G_1, G_2,$ $(2)G, G, F_1, F_2$	21	$g_{\mathrm{BW}} = 13.54(59)$ $m_{\mathrm{BW}} = 0.8161(30)$ $corr(am_{\mathrm{BW}},g_{\mathrm{BW}})=-0.324$	0.34(57)	1.56
G(c)	$(1/2,0)$ $(3/2,1)$	$G_{1u}, H_g, G_1, G_2,$ G, F_1, F_2	15	$g_{\mathrm{BW}} = 13.67(57)$ $m_{\mathrm{BW}} = 0.8146(30)$ $corr(am_{\mathrm{BW}},g_{\mathrm{BW}})=-0.372$	0.68(49)	0.99
G(d)	$(1/2,0)$ $(3/2,1)$	$H_g, G_1, G_2,$ $(2)G, G, F_1, F_2$	19	$g_{\mathrm{BW}} = 13.65(52)$ $m_{\mathrm{BW}} = 0.8137(29)$ $corr(am_{\mathrm{BW}},g_{\mathrm{BW}})=-0.360$	0.52(85)	0.93

Table 5.3 Phase shift fits: on top of the list are the fits of irreps containing a single S- and P-wave. For the global fits (**G**) different combinations are performed as explained in the text.

5.4.1 Phase shift fit procedure and results

The K-matrix is related to the phase shift as

$$K^{(Jl)} = \tan(\delta_{Jl}) \quad \text{and} \quad \hat{K}^{(Jl)} = \frac{1}{\rho}\tan(\delta_{Jl}) \tag{5.18}$$

The fit procedure we follow [100], parametrizes the phase shifts $\delta_{3/2,1}$ and $\delta_{1/2,0}$ using the Breit-Wigner and ERE K-matrix models above, and perform a global fit of the model parameters to all energy levels by minimizing the following χ^2 function:

$$\chi^2 = \sum_{\vec{P},\Lambda,n} \sum_{\vec{P}',\Lambda',n'} [C^{-1}]_{\vec{P},\Lambda,n;\vec{P}',\Lambda',n'} \left(\sqrt{s_n^{\Lambda,\vec{P}}}^{[\text{data}]} - \sqrt{s_n^{\Lambda,\vec{P}}}^{[\text{model}]} \right) \left(\sqrt{s_{n'}^{\Lambda',\vec{P}'}}^{[\text{data}]} - \sqrt{s_{n'}^{\Lambda',\vec{P}'}}^{[\text{model}]} \right) \tag{5.19}$$

where $\sqrt{s_n^{\Lambda,\vec{P}}}^{[\text{data}]}$ and $\sqrt{s_n^{\Lambda,\vec{P}}}^{[\text{model}]}$ are, respectively, the CMF energy points measured from the single exponential fit (listed in Tab. 5.2), and the roots of the Lüscher quantization conditions obtained for each parameter guess. Also, C^{-1} is the covariance matrix of the CMF energy levels measured on the lattice (label "data").

There are 21 energy levels from eight irreps available for the fit, as shown in Fig. 5.18. Before performing a fit over all energy points, we consider separately the irreps that include

either $J = 1/2$ or $J = 3/2$ exclusively. In particular, the inclusion of the irrep G_{1u} is dictated by the fact that it is the only irrep we can access that has only spin $J = 1/2$. It can help assess the contribution of the S_{31} phase shift freed from the P_{33} resonant contribution (in fact, in Tab. 3.7, the operators of G_{1u} are only from the $N\pi$ system). Also, within the scattering amplitude in $J = 1/2$, we do not include the P_{31} phase shift as it is suppressed with respect to S_{31}, and we later find the latter to be consistent with zero. On the other hand, multiple irreps that have a $J = 3/2$ content freed from $J = 1/2$: H_g, G_2, F_1 and F_2. We proceed to fit those irreps as well. These initial two fits enable us to obtain a good initial guess for the final global fit parameters and assess the stability of the fit over the choice of irreps included. The results for these two fits are listed in Tab. 5.3 with labels **S** and **P**. The fit **S** over irrep G_{1u} results in a very low χ^2/ndf caused by having only two levels available. The partial fit **P** for $(J = 3/2, l = 1)$ shows a much higher χ^2, which is reduced once we move to the global fit.

We then include all energy levels available in global fits (label **G**) with different combinations to assess the stability of the results. From the partials to the global fits, there is a slightly reduction in all parameters' uncertainties. For the global fit **G**, we implement five different combinations of levels included and choices of t_{min}/a to test the stability of the results. For the initial choice of levels listed in Tab. 5.2, the phase shift fit results are listed as **G(a)** and the simultaneous increase of t_{min}/a of one unit across the same levels yields the result **G(a+1)**. More focused choices among the noisiest levels are made in the fit **G(b)** where we vary t_{min}/a in selected levels according to the single and double exponential stability fits of the correlators. In particular, we have $+1$ shift on t_{min}/a on all levels of irreps $G_2, (2)G, F_1, F_2$, the ground state of G_1, the first excited of G, and $+2$ on the first excited of G. Additionally, we perform the global fit **G(c)** removing problematic levels from the list in Tab. 5.2: the highest level of irrep G and all levels in irrep $(2)G$. Furthermore, we fit the levels from **G(a)** excluding irrep G_{1u} in the global fit labeled **G(d)**. Overall, the results indicate that the fits provide compatibles results and are very stable across several choices.

We select fit **G(a)** to report the central values and statistical uncertainties of the fit parameters and derived quantities, but then estimate a systematic uncertainty from the maximum variation in the central values between **G(a)** and the other four global fits **G** listed in Table 5.3, i.e., for a parameter or derived quantity y, we calculate the systematic uncertainty associated with the fit choices as

$$\sigma_y^{sys} = \max_i(|y_{\mathbf{G}(i)} - y_{\mathbf{G}(\mathbf{a})}|) \ , \ \ i \in \{\mathbf{a+1}, \mathbf{b}, \mathbf{c}, \mathbf{d}\}. \tag{5.20}$$

Our final results for the Breit-Wigner parameters and scattering length in lattice units are then

$$
\begin{aligned}
am_{\mathrm{BW}} &= 0.8136 \pm 0.0029 \pm 0.0048, \\
g_{\mathrm{BW}} &= 13.62 \pm 0.50 \pm 0.43, \\
a_0/a &= 0.38 \pm 0.44 \pm 0.30.
\end{aligned}
\tag{5.21}
$$

A clear P_{33} ($\delta_{1/2,0}$) phase shift is shown in Fig. 5.19 from results of the fit **G(a)** with the parameters from the Breit-Wigner parametrization in Eq. (5.14). Because the P-wave
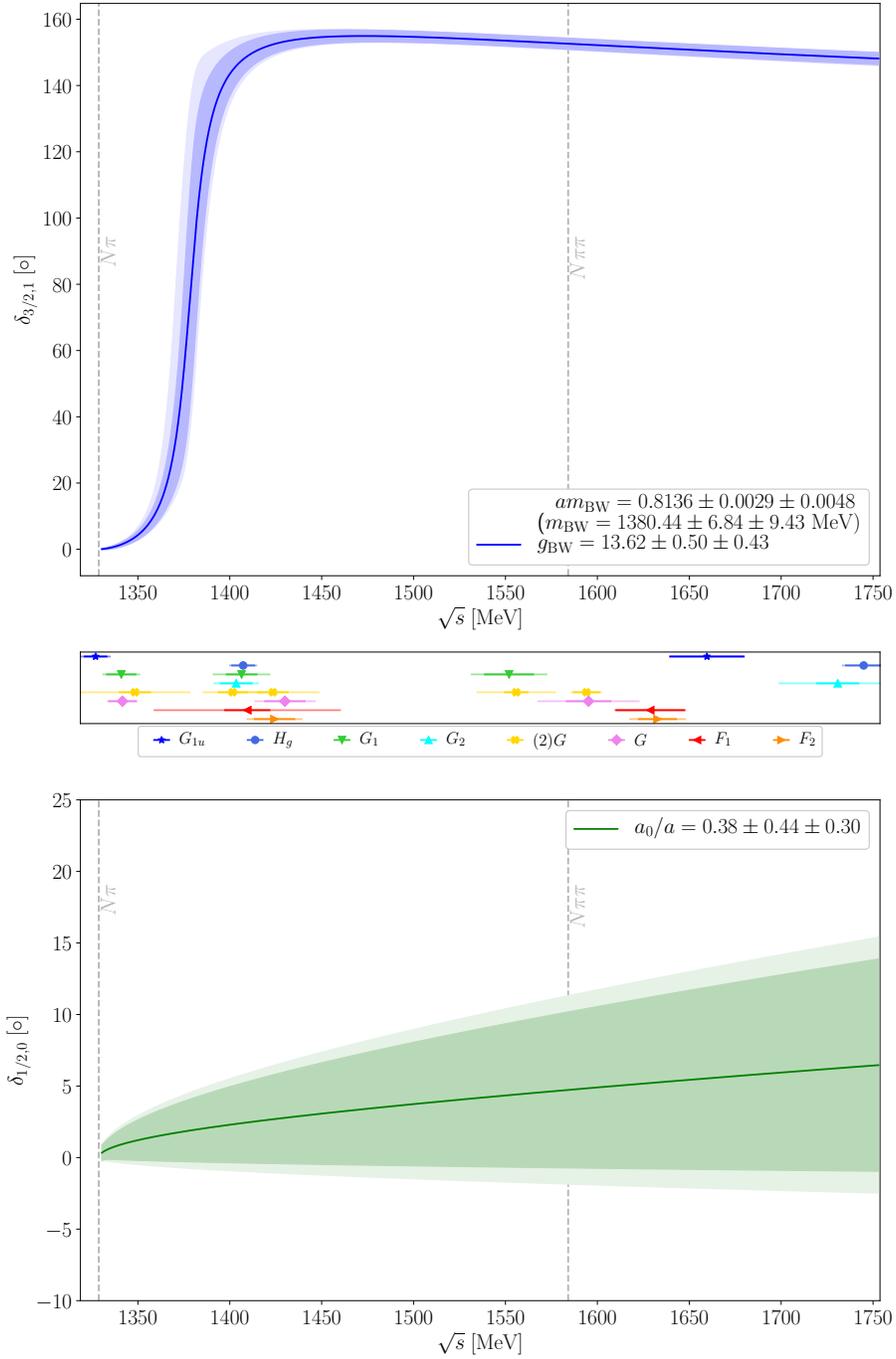
Figure 5.19 Energy dependence of the P_{33} (upper) and S_{31} (lower) phase shifts from the global fit **G(a)** alongside the energy points from the irreps (center). The darker inner bands show the statistical uncertainty. The lighter outer bands include our estimate of the systematic uncertainty associated with the fit ranges.

phase shift rises rapidly in the region of the resonance, we evaluated separate upper and lower systematic uncertainties that are included in the outer band in Fig. 5.19, using the asymmetric generalization of Eq. (5.20) corresponding to the largest shift in each direction

The scattering length a_0 results show large uncertainties that do not yet allow for a clear identification of the phase shift S_{31} ($\delta_{1/2,0}$), as shown in Fig. 5.19.

Additionally, we determine the closest T-matrix pole position in the complex $\sqrt{s}$ plane, associated with the $\Delta(1232)$ resonance. From Eq. (5.13) we solve the pole equation:

$$0 = m_{\mathrm{BW}}^2 - s_0 - i\sqrt{s_0}\Gamma(s_0). \tag{5.22}$$

The pole s_0 can be parametrized as $m_\Delta - i\Gamma/2$ and results in:

- m_Δ (real part): $0.8124 \pm 0.0027 \pm 0.0045$ ($1378.3 \pm 6.6 \pm 9.0$ MeV)

- $\Gamma/2$ (imag. part) : $0.00484 \pm 0.00061 \pm 0.00084$ ($8.2 \pm 1.0 \pm 1.4$ MeV)

Once we have obtained the decay width Γ from the imaginary part of the pole, we also determine the coupling $g_{\Delta-\pi N}$ from the definition of the decay width Γ provided by the leading-order chiral effective theory [101],

$$\Gamma_{EFT}^{LO} = \frac{g_{\Delta-\pi N}^2}{48\pi} \frac{E_N + m_N}{E_N + E_\pi} \frac{k^3}{m_N^2}, \tag{5.23}$$

for which we obtain

$$g_{\Delta-\pi N} = 23.8 \pm 2.7 \pm 0.9. \tag{5.24}$$

The results for the scattering length a_0 from ERE parametrization are generally consistent with zero within the uncertainties. The scattering length from global fit **G(a)** in the combination $a_0 m_{\pi^+}$,

$$a_0 m_{\pi^+} = 0.057 \pm 0.067 \pm 0.045, \tag{5.25}$$

can be compared with the values extracted from experimental data, -0.0785 ± 0.0032 in [102], -0.0894 ± 0.0017 in [103], and -0.101 ± 0.004 in [104].

To conclude, the extracted values for the resonance mass m_Δ and coupling $g_{\Delta-\pi N}$, are listed in Tab. 5.4 with other similar studies. In Refs. [39, 41] the authors used the Micheal and McNeile method [108] to determine the coupling $g_{\Delta-\pi N}$ at two different pion masses - one of which is very close to the physical pion mass. The Michael and McNeile method is based on the mixing of hadronic states on the lattice when the initial state energy is close to the final state energy and evaluating the corresponding transition matrix element $\langle\Delta|N\pi\rangle$. The coupling values seem sensible and compare reasonably our and the experimental value.

While the Michael and McNeile method is computationally more efficient, it suffers from systematical effects [109]. The Lüscher method, on the other hand, does not suffer from similar effects as has been demonstrated by the multitude of recent calculations [83]. However, the Lüscher method for baryon-meson scattering is significantly more challenging than for meson-meson, and so far, only limited results are available. The study in [105] was an exploratory study using the Lüscher method in 3 different (J, I) channels of the nucleon pion system at $m_\pi = 266$ MeV. Among those was the Δ, where the authors determined the phase

Collaboration	m_π [MeV]	Methodology	m_Δ [MeV]	$g_{\Delta-\pi N}$
Verduci (2014) [105]	266(3)	Distillation, Lüscher	$1396(19)_{\mathrm{BW}}$	19.90(83)
Alexandrou et.al. (2013) [39]	360	Michael, McNeile	1535(25)	27.0(0.6)(1.5)
Alexandrou et.al. (2016) [41]	180	Michael, McNeile	1350(50)	23.7(0.7)(1.1)
Andersen et.al. (2018) [38]	280	Stoch. distillation, Lüscher	$1344(20)_{\mathrm{BW}}$	37.1(9.2)
Our result	255.4(1.6)	Smeared sources, Lüscher	$1380(7)(9)_{\mathrm{BW}}$, $1378(7)(9)_{\mathrm{pole}}$	23.8(2.7)(0.9)
Physical value [106, 101, 107]	139.57	phenomenology, K-matrix	$1232(1)_{\mathrm{BW}}$, $1210(1)_{\mathrm{pole}}$	29.4(3), 28.6(3)

Table 5.4 Comparison of results for m_Δ and $g_{\Delta-\pi N}$. The uncertainties given for the lattice results are statistical/fitting only

shifts directly from few moving frames using both ground and excited states. The coupling determined in that study deviates slightly from our determination, yet remains statistically compatible. The more recent work presented in [38] also makes use of the Lüscher method; however, they elect to use only the ground state energies in a set of irreps and moving frames where partial waves do not mix. This reduces the difficulty of the analysis and allows the authors of [38] to determine the mass and coupling of the Δ at $m_\pi = 280$ MeV. In [38] the pion mass appears to be such that the mass of the Δ lies directly on the $N\pi$ threshold making a reliable extraction of the pole very difficult. On the other hand, the coupling can be determined quite well, and the authors found a central value that is quite a bit larger than ours, but due to the considerable statistical uncertainty, it remains compatible.

While these pioneering studies provide valuable insight into the Δ resonance, it remained unclear so far if a precise amplitude can be determined from the lattice. In this work, we have demonstrated that by using standard techniques in lattice QCD, i.e., using smeared forward, stochastic and sequential sources, it is possible to determine both ground and higher energy states in a multitude of irreps and momentum frames. Using advanced group-theoretical constructions, we built the interpolators and correlation matrices for eight irreps in four momentum frames, from which we extracted 21 energy levels. As some of these irreps mix J and l we used the minimization technique proposed in [100] in combination with the Lüscher method to determine the $(J = 3/2, l = 1)$ and $(J = 1/2, l = 0)$ scattering amplitudes. From those, we were able to find the $\Delta(1232)$ pole position and extract the pole mass and coupling. Our result is highlighted in Tab. 5.4 and is the most precise so far. Expecting little pion mass dependence on the coupling [17] we can compare it to experiment, and we see that, within uncertainties, we match well.

5.5 Discussion and Conclusions

This work addressed problems related to hadrons resonances and their study in the context of Lattice QCD. This aspect of the theory is interested in the development of techniques to simulates QCD on a finite volume and connect the energy spectrum of single and multi-hadron states to the resonance's observables.

In particular, we studied the baryon resonance $\Delta(1232)$ with quantum numbers $I = 3/2, J^P = 3/2^+$, expected to appear in the P_{33} wave (or phase shift $\delta_{3/2,1}$) in the $N\pi$ channels for the elastic scattering up to 1.6 GeV for a pion mass $m_\pi \approx 256$ MeV. Using state-of-the-art techniques and extensive group-theoretical considerations we were able to extract the parameters of the resonance including its pole position.

The central connection between lattice spectra and infinite-volume phase shifts is provided by the Lüscher method, and it relies on parametrizing the shift in energy between the interacting energies and the non-interacting counterparts. The tools that provide the parametrization are the quantization conditions; computable for each irrep. To reliably extract the spectra, we first projected single and multi-hadron operators in the various irreps of the lattice. Using just a single volume, we included moving frames to increase the number of energy points available to constrain the phase shift fit. For each irrep considered, we were able to compute correlation matrices in the $\Delta - N\pi$ system, averaged over different momentum direction and rows of the irrep. The energy points extracted from the correlation matrices were simultanueously fit using the quantization conditions in the K-matrix parametrization of the phase shifts $\delta_{3/2,1}$ and $\delta_{1/2,0}$. The second phase shift $\delta_{1/2,0}$ (S_{31}) was included in the analysis as many irreps mix angular momentum $J = 3/2$ and $J = 1/2$. The S_{31} wave was parametrized in the effective range potential framework and obtained a value for the scattering length of $a_0 = (0.057 \pm 0.067 \pm 0.045)/m_{\pi^+}$.

For the primary phase shift $\delta_{3/2,1}$, corresponding to the resonance $\Delta(1232)$, we extracted mass $m_{\mathrm{BW}} = 1380(7)(9)$ MeV and coupling $g_{\mathrm{BW}} = 13.6(5)(4)$ in the elastic energy region through a Breit-Wigner parametrization. We also extracted its T-matrix pole position in the scattering amplitudes, from which we were able to determine the decay width Γ. From the alternative definition of the decay width provided by the chiral effective field theory in Eq. (5.23), we determined the coupling $g_{\Delta-\pi N} = 23.8(2.7)(0.9)$, compared to other recent studies in Tab. 5.4. In this comparison our study stands out as the first where excited-state levels are successfully used in a boosted baryon system. To conclude, the extracted parameters related to the $\Delta(1232)$ show small uncertainties while being compatibles with other studies of similar pion mass, confirming a clear identification of the resonance and the righteousness of the theoretical approach employed.

Future work will include lattice ensembles with different spatial volumes and lower pion mass that will provide more energy points to better constrain the phase shifts extracted and, at the same time, expand on the partial wave contributions included in the analysis. Using multiple lattice ensembles will also enable us to measure systematic errors associated with finite volume and unphysical quark masses.

Chapter Six

Roberge-Weiss endpoint and chiral symmetry restoration in $N_f = 2 + 1$ QCD

The results described in this chapter have been published as [4]. The sign problem is a well-known obstacle that prevents numerical simulation to probe the QCD phase at finite chemical potential μ. The problems that arise with the introduction of a finite chemical potential μ in Monte Carlo calculations can be understood considering QCD at non-zero temperature and baryon density. We have the baryon number coupled to chemical potential μ, and we have the grand canonical partition function of the form

$$Z = \text{Tr} e^{-(H-\mu N)/T} = e^{-F/T} \tag{6.1}$$

where N is the quark number and F is the free energy. A possible way to think about chemical potential is that it corresponds to the energy required to add a new particle to the system. The chemical potential enters in the probability weight of the Monte Carlo algorithm through the fermionic determinant. Explicitly:

$$Z = \int DU e^{-S_G[U]} \det M(\mu) \tag{6.2}$$

At non-zero chemical potential, the fermion determinant turns out to be not real and positive, but complex,

$$[\det M(\mu)]^* = \det M(-\mu^*) \in \mathbb{C} \tag{6.3}$$

as a result, the integrand in Eq. (6.2) is complex as well and importance sampling is no more applicable. This sign problem is not specific for fermions, and in particular, is not due to the Grassmann nature of the fermion, but it is also present in bosonic theories [110].

The use of the imaginary chemical potential is a partial workaround to the sign problem subject of several studies [111, 112, 113, 114, 115, 116, 117, 118, 119, 120, 121, 122, 123, 124, 125, 126, 127, 128, 129, 130]. While this method does not represent a solution, it provides access to the analytical continuation of the QCD phase diagram, obtaining information about QCD at finite baryon density partially avoiding the sign problem. Furthermore, the imaginary chemical potential provides an interesting extension of the QCD phase diagram where, for particular choices of the chemical potential, one recovers exact symmetries even in the presence of finite quark masses. This in turn leads to phase transitions and critical points that could be relevant for the physical region of the phase diagram.
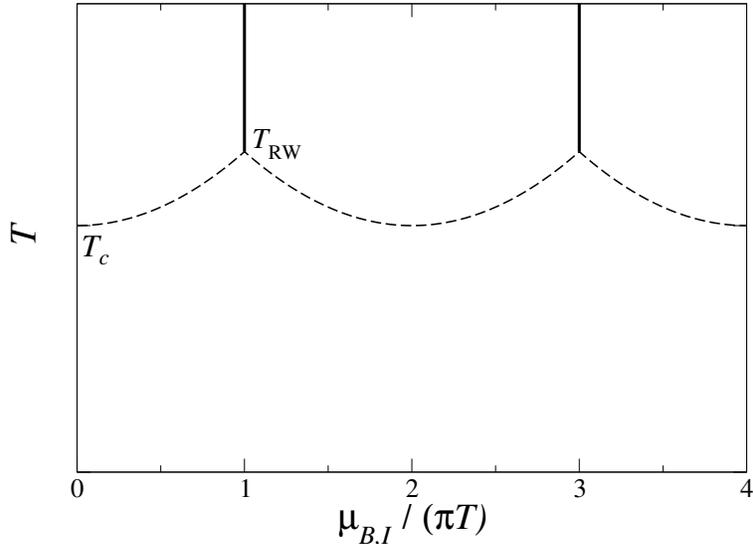
Figure 6.1 Sketch of the phase diagram of QCD in the $T - \mu_{B,I}$ plane. The vertical lines are the RW transitions, the dashed lines are the analytic continuation of the pseudo-critical line.

Considering the case of QCD with an imaginary chemical potential μ_B, it is observed that for certain values known as Roberge-Weiss (RW) points [131], at $\mu_B = i\mu_{B,I} = ik\pi T$ where k is an odd integer, there is an exact Z_2 symmetry from a remnant of the original Z_3 symmetry associated to the pure gauge case. This symmetry is spontaneously broken at a critical temperature T_{RW} which fixes the endpoint (RW endpoint) of first-order transition lines; those are present at fixed μ_B in the high-T region of the phase diagram (see Fig. 6.1).

There are many studies that have investigated RW transition lines, in both lattice simulations [112, 113, 114, 115, 116, 117, 125, 126, 127, 128, 129, 130] and effective models [132, 133, 134, 135, 136, 137]. Early studies have shown particular features of the RW endpoints for both $N_f = 2$ and $N_f = 3$ degenerate flavors: the transition is first order for small quark masses, likely down to the chiral limit, second order for intermediate masses, and first order again for large quark masses; the three regions are separated by tricritical points [138, 139, 140]. A study at physical pion mass with stout improved staggered fermions reported in [141] with $N_f = 2 + 1$ QCD shows a reliable continuum extrapolation of the endpoint transition temperature $T_{RW} \simeq 208(5)$ MeV, corresponding to $T_{RW}/T_c \simeq 1.34(7)$ where T_c is the pseudo-critical chiral crossover temperature at zero baryon chemical potential. In the study a finite size scaling (FSS) has being performed only for $N_t = 4, 6$ providing evidence for a second order transition. This suggests that the chiral tricritical pion mass, if any, is lower than the physical pion mass $m_\pi \simeq 135$ MeV.

In this study, we extend the analysis of RW endpoint below physical quark masses down to a pion mass of order 50 MeV with the same improved discretization of [141]. The purpose of this study is to locate the tricritical point, even though, various studies have provided evidence of a general shrinking of the first order regions as the continuum limit is approached. Therefore, there is no guarantee that a first order RW endpoint transition can be found in the chiral and continuum limit of $N_f = 2 + 1$ QCD. It is important to point out that the

task itself is highly non-trivial, as to have a reliable extrapolation once should get close enough to the chiral limit; close enough to the continuum limit so that the chiral properties of dynamical fermions are effective (in the present context of staggered fermions, that means that taste symmetry breaking is negligible and all pions become effectively light); and keep the physical volume large enough, i.e. $Lm_\pi \gg 1$ as $m_\pi \to 0$. All these conditions can't be satisfied by present computing resources. This study presents a calculation for only $N_t = 4$, and represents a small step in the direction of a more complete calculation.

6.1   Numerical Setup

We employ a rooted stout staggered discretization of $N_f = 2 + 1$ QCD in the presence of imaginary quark chemical potentials $\mu_{f,I}$, its partition function reads:

$$Z \;\; = \;\; \int \mathcal{D}U \, e^{-\mathcal{S}_{YM}} \prod_{f=u,\,d,\,s} \det\left(M_{\mathrm{st}}^f[U,\mu_{f,I}] \right)^{1/4}, \tag{6.4}$$

$$\mathcal{S}_{YM} \;\; = \;\; -\frac{\beta}{3} \sum_{i,\mu \neq \nu} \left(\frac{5}{6} W_{i;\,\mu\nu}^{1\times1} - \frac{1}{12} W_{i;\,\mu\nu}^{1\times2} \right), \tag{6.5}$$

$$(M_{\mathrm{st}}^f)_{i,j} \;\; = \;\; am_f \delta_{i,j} + \sum_{\nu=1}^{4} \frac{\eta_{i;\nu}}{2} \left[e^{ia\mu_{f,I}\delta_{\nu,4}} U_{i;\nu}^{(2)} \delta_{i,j-\hat\nu} - e^{-ia\mu_{f,I}\delta_{\nu,4}} U_{i-\hat\nu;\nu}^{(2)\dagger} \delta_{i,j+\hat\nu} \right], \tag{6.6}$$

$\mathcal{S}_{YM}$ is a tree level Symanzik improved gauge action [9] constructed from the original link variables, $W_{i;\,\mu\nu}^{n\times m}$ being the trace of a $n \times m$ rectangular loop, while the staggered fermion matrix $(M_{\mathrm{st}}^f)_{i,j}$ is built up in terms of the two times stout-smeared[16] links $U_{i;\nu}^{(2)}$, with an isotropic smearing parameter $\rho = 0.15$. With thermal boundary conditions (periodic/anti-periodic in Euclidean time for boson/fermion fields), the temperature is given by $T = 1/(N_t a)$. Also, we fix $N_t = 4$ in all simulations, while the lattice spacing a is a function of β and of the bare quark masses. The previous study in Ref. [141] where computation were performed using a line of constant physics (LCP), i.e. the tuning of the parameter β to keep the masses of physical states approximately equal to the physical values. In contrast, in this study, we decide to fix quark masses keeping $m_u = m_d \equiv m_l$ and $m_s/m_l = 28.15$ (which correspond to the physical mass ratio). The advantage of this choice is reflected in the fact that the simulations of this study differ only in the choice of β, thus enabling us to make use of standard reweighting methods [142], whereas in the previous study [141] this was not feasible.

We decided to use three different values of quark masses, namely $am_l = 0.003$, $am_l = 0.0015$, and $am_l = 0.00075$. For each mass value, the pseudo-critical coupling $\beta_{RW}(am_l, N_t)$ has been located. Also, we have performed a series of run at different values of β around β_{RW}, used for reweighting. For each case, computations were performed on lattices $L_s^3 \times 4$ for different values of the spatial extent L_s (in the range $16 \to 32$) to perform an FSS analysis. A complete list of the finite-T runs performed can be found in Tab. 6.1; statistics reach up to 50K Rational Hybrid Monte-Carlo unit length trajectories for simulation points around the transition.

For some values of β additional runs at zero temperature have been performed to be used for renormalization and scale setting purposes. The lowest mass values for the quarks have

am_l	β	$L_s^3 \times 4$ lattices
0.003	3.3900	16
	3.3950	16
	3.4000	16, 20, 24
	3.4050	16, 20, 24, 28
	3.4080	28
	3.4100	16, 20, 24
	3.4110	28
	3.4140	28
	3.4150	16, 20, 24
	3.4170	32
	3.4175	28
	3.4200	16, 20, 24, 28
	3.4250	16, 20, 24
	3.4300	16, 20, 24
	3.4350	20, 24
	3.4400	20, 24

am_l	β	$L_s^3 \times 4$ lattices
0.0015	3.3500	16
	3.3550	16
	3.3600	16, 20, 24
	3.3650	16, 20, 24
	3.3700	16, 20, 24
	3.3750	16, 20, 24, 28
	3.3800	16, 20, 24, 28
	3.3820	32
	3.3825	24, 28
	3.3835	32
	3.3850	16, 20, 24, 28, 32
	3.3865	32
	3.3875	24, 28
	3.3900	16, 20, 24, 28
	3.3925	24, 28
	3.3950	16, 20, 24, 28
	3.4000	16, 20, 24

am_l	β	$L_s^3 \times 4$ lattices
0.00075	3.3400	16
	3.3450	16
	3.3500	16
	3.3550	16, 20, 24
	3.3575	20, 24
	3.3600	16, 20, 24, 28
	3.3625	16, 20, 24, 28
	3.3650	16, 20, 24, 28
	3.3675	20, 24, 28
	3.3700	16, 20, 24, 28
	3.3725	20, 24, 28
	3.3750	16, 20, 24, 28
	3.3775	20, 24, 28
	3.3800	16, 20, 24, 28
	3.3850	20, 24

Table 6.1 Simulation details for all finite temperature runs.

am_l	β	a [fm]	m_π[MeV]	$m_\pi^{(1)}$[MeV]
0.00075	3.340	0.29039(5)	48.23(6)	437(17)
0.00075	3.370	0.28332(5)	49.40(7)	433(11)
0.00075	3.400	0.27330(7)	51.07(6)	418(22)
0.0015	3.36	0.28815(4)	68.58(3)	435(4)
0.0015	3.385	0.28078(4)	70.27(3)	431(4)
0.0015	3.42	0.26831(5)	73.25(3)	408(3)
0.003	3.38	0.28616(4)	97.24(2)	444.5(4)
0.003	3.415	0.27502(5)	100.86(3)	425(2)
0.003	3.440	0.26539(12)	104.00(6)	410.6(1.3)

Table 6.2 Scale setting determinations, obtained from zero temperature runs performed on a $32^3 \times 48$ lattice; m_π stands for the pseudo-Goldstone pion mass, while $m_\pi^{(1)}$ corresponds to the first excited pion.

been chosen to approximately equal to $m_\pi = m_\pi^{(phys)} \times \sqrt{0.00075/0.00558} \simeq 50$ MeV around the transition point. Nonetheless, this does not represent a quantitative estimate, and for this reason, we perform computations at $T \simeq 0$, with the purpose to directly determine both m_π and lattice spacing. The latter can be determined using a technique based on the gradient flow [143] and in particular the so-called w_0 parameter [144].

All scale setting and pion mass determinations are shown in Tab. 6.2: all computations have been performed on a $32^3 \times 48$ lattice for each quark mass, with statistics of the order of one thousand Rational Hybrid Monte-Carlo unit length trajectories for each simulation point. We obtained pion masses from standard Euclidean time correlators of staggered quark operators (see, e.g., Refs. [145]) for both the ground (pseudo-Goldstone) and first excited state. The latter is expected to be higher, at finite lattice spacing, because of the taste
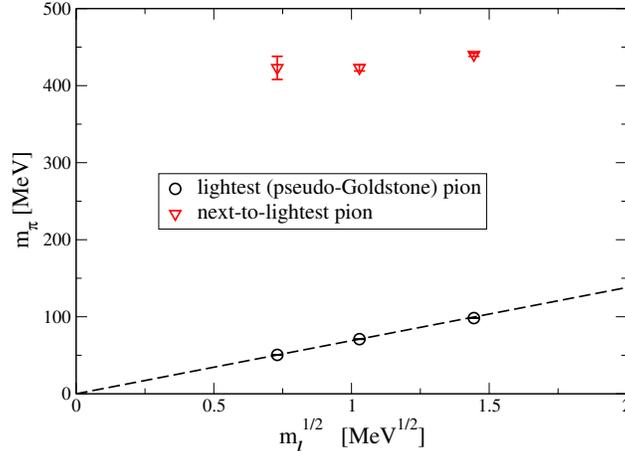
Figure 6.2 Pion masses at $\beta = 3.39$ for the three values of the bare light mass m_l we explored, expressed in physical units. The dashed line is the result of a best fit to the expected $m_\pi \propto \sqrt{m_l}$ dependence.

violations of the staggered discretization.

The quality of our approach to the chiral limit can be estimated by the severity of such taste violations; to this end, we outline in Tab. 6.2 the mass $m_\pi^{(1)}$ of the first excited pion. In Fig. 6.2 we show for a fixed value of the bare gauge coupling $\beta = 3.39$, the values obtained for the pseudo-Goldstone pion and $m_\pi^{(1)}$ as a function of the square root of the light bare quark mass (in physical units). This helps to assess the quality of our approach to the chiral limit and it can be seen that while m_π approaches zero as $m_l \to 0$ following quite closely the prediction of chiral perturbation theory, $m_\pi \propto \sqrt{m_l}$, the first excited state is much less affected by the change in am_l. This suggests that in our approach to the chiral limit we are effectively considering a theory with no more than one light pion: that is quite different from the physical theory and, eventually, one would like to understand how this fact may bias the results obtained for the order of the phase transition.

To realize a simply baryonic chemical potential (i.e. $\mu_Q = \mu_S = 0$) we set $\mu_u = \mu_d = \mu_s \equiv \mu_q = \mu_B/3$. The idea behind an imaginary μ_q is that it corresponds to a rotation of fermionic temporal boundary conditions by an angle $\theta_q = \text{Im}\,(\mu_q)/T$; it suggests periodicity in θ_q of $2\pi/N_c$ (instead of 2π), which can be exactly canceled by a center transformation on gauge fields. Considering the temperature range, this periodicity is smoothly realized at low T, while at high T the value of θ_q chooses one of three different values, i.e. the minima of the Polyakov loop effective potential. This, in turn, leads to a first order phase transition occurring as the θ_q traverses the boundary between two center sectors. These transition lines (RW lines) characterize the phase diagram at high T as sketched in Fig. 6.1. Located at $\theta_q = (2k + 1)\pi/N_c$ for an integer k they terminate with an endpoint at temperature T_{RW}, where an exact Z_2 symmetry breaks spontaneously. Moving across these lines one can then expect to encounter a second order critical point in the 3D-Ising universality class or a first order transition; in the latter case, the endpoint is a triple point.

We proceed to focus on one particular RW line, $\theta_q = \pi$, and employ the Polyakov loop as the order parameter. To assess the universality class of the endpoint a finite size scaling

	ν	γ	γ/ν	$1/\nu$
$3D$ Ising	0.6301(4)	1.2372(5)	~ 1.963	~ 1.587
Tricritical	$1/2$	1	2	2
1st Order	$1/3$	1	3	3

Table 6.3 Critical exponents relevant to our finite size scaling analysis (see, e.g., Refs. [146, 147]).

(FSS) analysis is used for the susceptibility of the order parameter

$$\chi_L \equiv N_t L_s^3 \left(\langle (\mathrm{Im}(L))^2 \rangle - \langle |\mathrm{Im}(L)| \rangle^2 \right), \tag{6.7}$$

Alternatively, one could take as an order parameter any of the quark number densities (where $q = u, d, s$)

$$\langle n_q \rangle \equiv \frac{1}{(L_s^3 N_t)} \frac{\partial \log Z}{\partial \mu_q} \tag{6.8}$$

which should vanish for $\theta_q = (2k+1)\pi/N_c$ (because of the mentioned periodicity and because they are odd in θ_q) unless the Z_2 symmetry (which is equivalent to charge conjugation) is spontaneously broken. However, our analysis will be based exclusively on the Polyakov loop.

Numerical simulations have been performed on the COKA cluster, using 5 computing nodes, each with 8 NVIDIA K80 dual-GPU boards and two 56 Gb/s FDR InfiniBand network interfaces. Our parallel code (OpenStaPLE) is a single [6] and multi [5] GPU implementation of a standard Rational Hybrid Monte-Carlo algorithm. It is an evolution of a previous CUDA code [148], developed using the OpenACC and OpenMPI frameworks to manage respectively parallelism on the GPUs and among the nodes. The multi-GPU implementation [6] has been essential to perform some of the zero temperature runs, which otherwise would have not fitted on a single GPU for memory reasons.

The most expensive simulations have been those regarding the lowest explored quark mass, $am_l = 0.00075$. Overall, a rough estimate of the total computational cost of our investigation is 3×10^5 equivalent run-hours on a K80 GPU.

6.2 Finite size scaling analysis and order of the transition

In Eq. (6.7) we have defined the susceptibility χ_L, which is expected to scale as

$$\chi_L = L_s^{\gamma/\nu} \, \phi(t L_s^{1/\nu}), \tag{6.9}$$

for which $t = (T - T_{\mathrm{RW}})/T_{\mathrm{RW}}$ is the reduced temperature and one has $t \propto \beta - \beta_{RW}$ close enough to T_{RW}. The way to interpret Eq. (6.9) is that $\chi_L/L_s^{\gamma/\nu}$, when plotted as a function of $(\beta - \beta_{RW})L_s^{1/\nu}$ and measured on different spatial sizes, would scale according to the critical exponents ν and γ representing the universal behavior associated. We report the values of indices in Tab. 6.3; along with the critical exponents for the first order and 3D-Ising we also report tricritical indices. The latter describes the critical behavior exactly at the separation between the first order and second order region. Nonetheless, before the thermodynamic
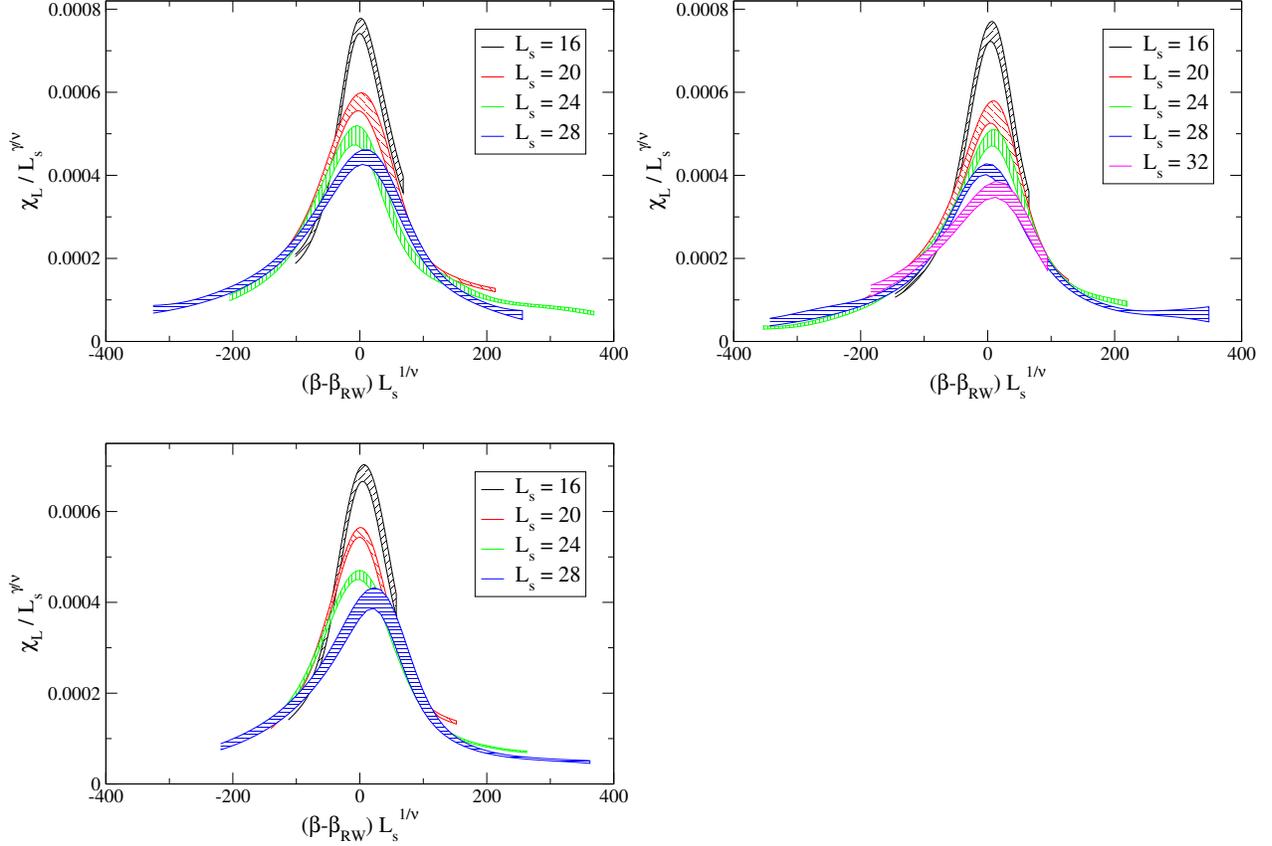
Figure 6.3 Finite size scaling for the susceptibility of the Polyakov loop according to first order critical indexes. Listed for the masses: (a) $am_l = 0.003$,(b) $am_l = 0.0015$ and (c) $am_l = 0.00075$.

limit is reached, they could describe the critical behavior in a finite neighborhood of the tricritical point [149].

In Fig. 6.3, Fig. 6.4 and Fig. 6.5 is shown the plots for $\chi_L/L_s^{\gamma/\nu}$ vs. $(\beta - \beta_{RW})L_s^{1/\nu}$ for the three different values of masses, respectively for first order, 3D-Ising and tricritical indexes. Looking at the plots it can be ruled out a first order transition for all masses, while both the 3D-Ising and the tricritical behavior show a reasonable scaling.

To further corroborate the dismiss of a first order transition on all masses, we show in Fig. 6.6 for the lowest mass, $am_l = 0.00075$, the probability distribution of the plaquette and the unrenormalized quark condensate for different lattice volumes. A dubious double-peak structure appears only in the chiral condensate distribution at small lattices, and it tends to disappear when approaching the thermodynamic limit.

These results suggest that a region with a first order transition, if present, is limited to pion masses below 50 MeV. Nonetheless, before reaching a definite conclusion there are many systematics to consider. As previously discussed, our chiral limit approach corresponds to only one pion becoming massless, while the others stay above 400 MeV. An improvement to tackle this problem would be to repeat this study with larger values of N_t (smaller lattice
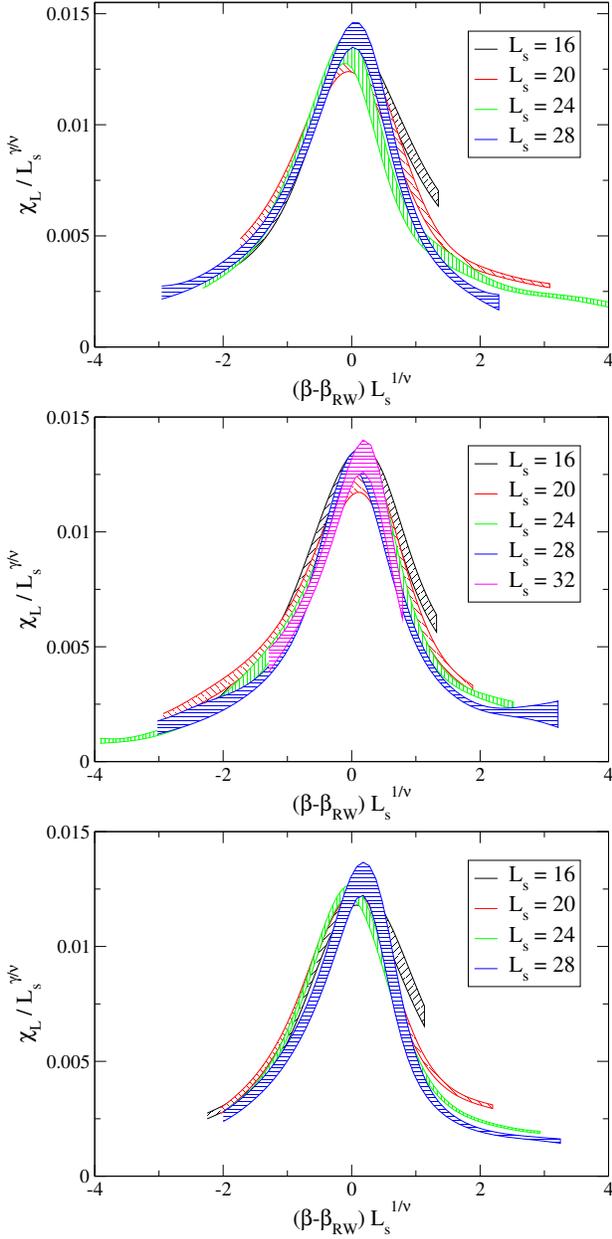
Figure 6.4 Finite size scaling for the susceptibility of the Polyakov loop according to 3D-Ising critical indexes. Listed for the masses: (a) $am_l = 0.003$,(b) $am_l = 0.0015$ and (c) $am_l = 0.00075$.
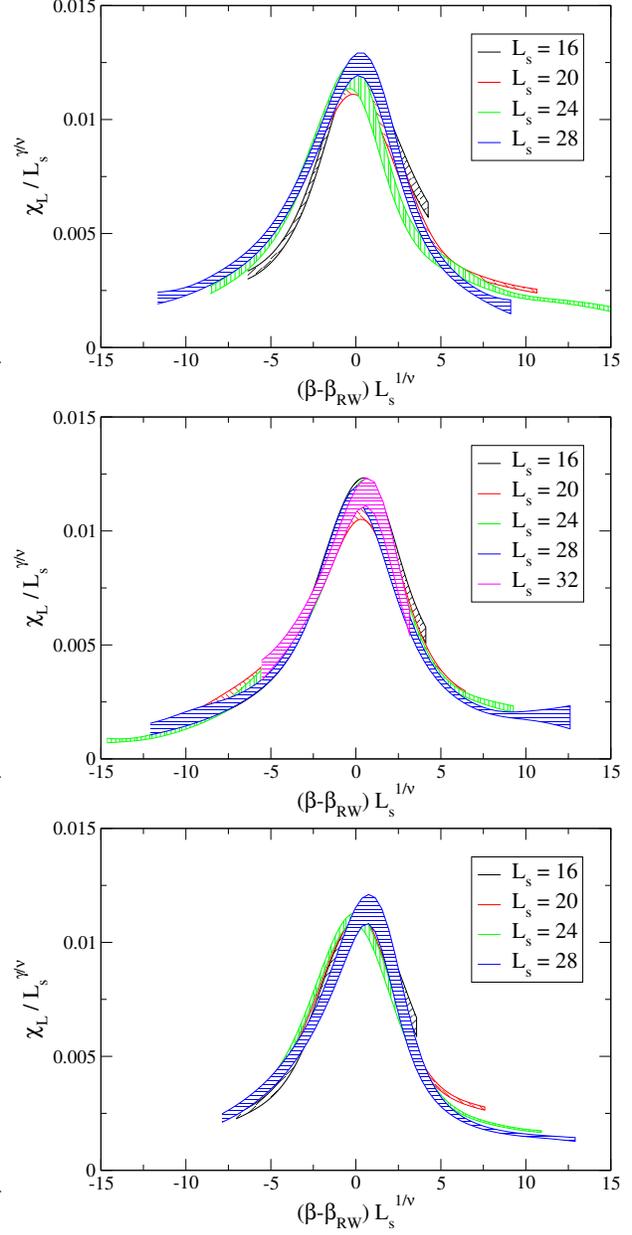
Figure 6.5 Finite size scaling for the susceptibility of the Polyakov loop according to tricritical indexes. Listed for the masses: (a) $am_l = 0.003$,(b) $am_l = 0.0015$ and (c) $am_l = 0.00075$.
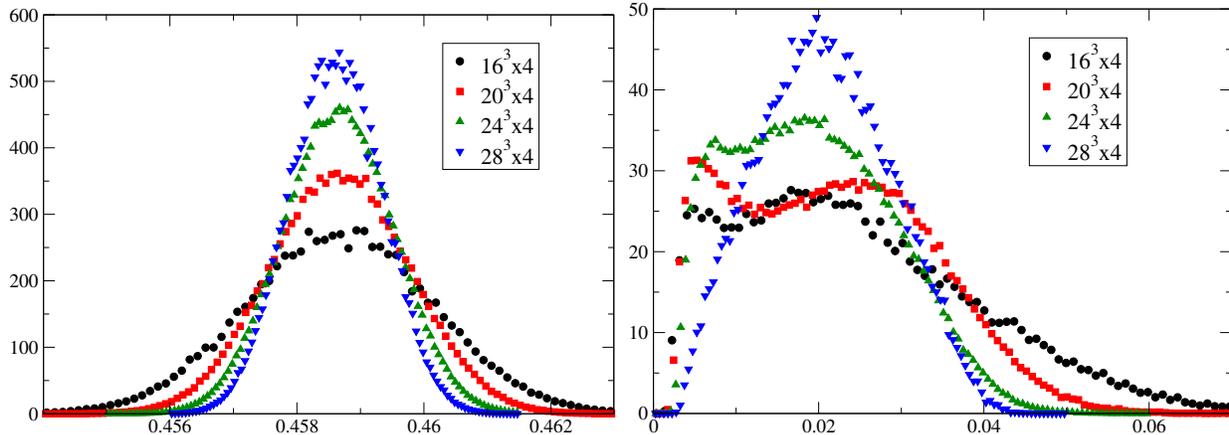
Figure 6.6 Probability distribution of the plaquette (top) and of the unrenormalized chiral condensate (bottom) at the transition point for different values of the spatial size L_s.

spacings), for which one would expect the other pions to become lighter. Additional chiral degrees of freedom could, in principle, change the outcome and enlarge the first order region, even if this is at odds with the common experience of shrinking of first order regions as the continuum limit is approached. Unfortunately, at the present level of computational resources, going to significantly larger values of N_t is not feasible, and is thus left for future work.

An additional remark addresses the lattice sizes employed in this study. The maximum values of aL_sm_π that we have reached are 2, 3, and 4 respectively for $am_l = 0.00075$, $am_l = 0.0015$ and $am_l = 0.003$. These values are generally considered not particularly large, in particular for the lowest quark mass. Nonetheless, signs of deviation from a second order scaling are not visible and the development of a double-peak structure in the chiral condensate, if any, is weakly present for small volumes and quickly disappearing when going to larger sizes.

6.3 Discussion and Conclusions

This study has presented an investigation of the Roberge-Weiss (RW) transition endpoint. We used lattices with $N_t = 4$ sites in the temporal direction, at different spatial sizes and three different light quark masses, $am_l = 0.003, 0.0015$, and 0.00075, corresponding respectively to pseudo-Goldstone pion masses $m_\pi \simeq 100, 70$, and 50 MeV around the transition. The values of masses maintain a fixed physical strange-to-light mass ratio ($m_s/m_l = 28.15$), making the simulations differ only in the values of β, enabling us to exploit multi-histogram methods. The simulation used a stout staggered discretization for the fermion sector and the tree-level Symanzik improved action for the pure gauge sector.

The chemical potential has been fixed to an imaginary value of $\mu_{f,I}/T = \pi$ for all flavors so that the imaginary part of the Polyakov loop would serve as an order parameter for the RW

transition. The analysis conducted over its susceptibility has ruled out the presence of a first order transition at all masses surveyed. A confirmation of this assessment came also from the probability distribution of the plaquette and of the chiral condensate at the transition points, which showed no sign of a double peak structure emerging as the thermodynamic limit is approached. On the contrary, we observed a clear confirmation of scaling according to the second order critical behavior, i.e. that of the three dimensional Z_2 (Ising) universality class.

Therefore, our results don't show evidence of a first order region around the chiral point for the RW transition, which for $N_f = 2$ unimproved staggered fermions was located below $m_\pi \simeq 400$ MeV [138] for $N_t = 4$. A strong cutoff dependence of the tricritical pion mass has been found also in studies with Wilson fermions [150, 151], however, it is puzzling that the tricritical pion mass can go down at least one order of magnitude (or disappear at all) by just improving the discretization at fixed N_t.

Clearly, our results need further refinement in some respects. Because of the taste symmetry breaking, as we approach the chiral limit only the lowest pion mass (pseudo-Goldstone) is directly linked to the residual staggered chiral symmetry, while the others maintain their mass above 400 MeV with little sign of dependence on the quark masses (see Fig. 6.2). Thus, even if counter-intuitive, it cannot be excluded that approaching the continuum limit the critical behavior changes and the first order region around the chiral point enlarges again.

Therefore, approaching the chiral limit for larger values of N_t will require additional computational resources that are presently not available to us.

Chapter Seven

Conclusions

In this thesis, we have presented two studies exploring QCD topics at zero and finite temperature: a determination of the $\Delta(1232)$ resonance parameters, and an investigation of the Roberge-Weiss endpoint, both using Lattice QCD.

In the former case, we addressed problems related to hadron resonances using Lattice QCD and the Lüscher method. We presented a determination of the properties of the low-lying baryon $\Delta(1232)$, measuring the elastic pion-nucleon scattering amplitude for isospin $I = 3/2$ in P-wave with $J^P = 3/2^+$, where the resonance emerges as the dominant contribution. Our calculation was performed with $N_f = 2 + 1$ Wilson clover fermions on an ensemble of spatial lattice size $L \approx 2.8$ fm. The pion and nucleon masses are $m_\pi = 255.4(1.6)$ MeV and $m_N = 1073(5)$ Mev, and the strong decay channel $\Delta \to N\pi$ is found to be above threshold. The Lüscher method is exploited to connect the lattice spectra to the infinite-volume scattering amplitudes through the quantization condition. Finite volume energy spectra are extracted from the GEVP analysis of correlation matrices built from Δ and $N\pi$ operators. Lattice states are classified by irreducible representations (irreps), which map to the infinite-volume irreps J^P. Thus, correlation matrices are composed of operators projected in the relevant lattice irreps, for which we used the projection method. To gain additional energy points on a single ensemble, we analyzed multiple moving frames for a total momentum up to $\vec{P} = \frac{2\pi}{L}(1,1,1)$. For each frame, we computed the spectra and quantization condition in all relevant irreps, including those that mix $J = 3/2$ and $J = 1/2$. In total, we considered eight irreps in four momentum frames, that provided 21 energy levels from which we extracted the scattering phase shift for $J = 3/2$ and $J = 1/2$ (we neglected mixing with $J > 3/2$). Each J receives contributions from two values of orbital angular momentum l, but at the present level of precision, we can access only the dominant value of l for each: $l = 1$ for $J = 3/2$ (P_{33}) and $l = 0$ for $J = 1/2$ (S_{31}). The P_{33} phase shift is parametrized with a Breit-Wigner model, while the leading-order effective-range expansion (ERE) is used for S_{31} phase shift. Additionally, we determined the pole position $m_\Delta - i\Gamma/2$ and coupling $g_{\Delta - N\pi}$ associated with the $\Delta(1232)$ resonance. These parameters are listed in Tab. 5.4 with previous similar studies. For our pion mass (and non-zero lattice spacing), the Δ mass is approximately 170 MeV higher than in nature. The coupling $g_{\Delta - N\pi}$ agrees with the experimental value at the 2σ level and is consistent with other lattice determinations within our uncertainties. The determination for the S-wave scattering length a_0 is consistent with zero and is also consistent with phenomenological determination, given our uncertainties. Additional work is already

ongoing using a second ensemble with larger spatial volume to gain additional points. The new spectra will help constrain the phase shift determination, expand on the partial-wave contributions included in the analysis, and provide information on remaining finite-volume systematic errors. Another planned ensemble will further help investigate the dependence on the pion mass and on the lattice spacing.

The second study presented explored the QCD phase diagram in the analytic continuation of imaginary chemical potential. As the sign problem poses a fundamental obstacle to probe the QCD phase at finite chemical potential μ, the use of an imaginary chemical potential offers a partial workaround that can provide information about the physical QCD phase diagram. For certain values of the imaginary chemical potential, knowns as Roberge-Weiss endpoint, there is an exact Z_2 symmetry, which gets spontaneously broken at a critical temperature T_{RW}. We investigated the fate of the Roberge-Weiss endpoint as we approach the chiral limit. We employed three different values of light quark masses corresponding to pseudo-Goldstone pion masses $m_\pi \simeq 100, 70$, and 50 MeV around the transition while maintaining a constant physical value of the strange-to-light mass ratio. We adopted a $N_f = 2+1$ stout staggered discretization on lattices with $N_t = 4$ sites in the temporal direction. To assess the order of the transition we used various ensembles at different spatial volumes and used a finite-size scaling analysis applied to the susceptibility of the Polyakov loop. In all explored mass ranges the results strongly indicate a second-order transition in the 3D Ising universality class. This is also confirmed by a subsequent analysis of the probability distribution of the plaquette lacking a clear double-peak structure. These considerations leave the premises for future investigations which will have to focus on the directions of excluding finite-size contamination and exploring larger N_t (smaller lattice spacing).

While these two studies differ in their focus and approach, they have demonstrated reliable methods to study hadrons and their properties, as well as exploring the phase diagrams, from first principles of QCD. They have successfully provided new insight and extended the results from previous studies, confirming the soundness of the lattice QCD framework as a tool to investigate the quantum chromodynamics theory.

REFERENCES

[1] Giorgio Silvi et al. "P-wave nucleon-pion scattering amplitude in the $\Delta(1232)$ channel from lattice QCD". In: *Phys. Rev. D* 103 (9 May 2021), p. 094508. DOI: 10.1103/PhysRevD.103.094508. URL: https://link.aps.org/doi/10.1103/PhysRevD.103.094508.

[2] Srijit Paul et al. "Towards the P-wave nucleon-pion scattering amplitude in the $\Delta(1232)$ channel". In: *arXiv preprint arXiv:1812.01059* (2018).

[3] Gumaro Rendon et al. "I= 1/2 S-wave and P-wave K π scattering and the κ and K* resonances from lattice QCD". In: *Physical Review D* 102.11 (2020), p. 114520.

[4] Claudio Bonati et al. "Roberge-Weiss endpoint and chiral symmetry restoration in $Nf = 2 + 1$ QCD". In: *Physical Review D* 99.1 (2019), p. 014502.

[5] Claudio Bonati et al. "Portable multi-node LQCD Monte Carlo simulations using OpenACC". In: *International Journal of Modern Physics C* 29.01 (2018), p. 1850010.

[6] Claudio Bonati et al. "Design and optimization of a portable LQCD Monte Carlo code using OpenACC". In: *International Journal of Modern Physics C* 28.05 (2017), p. 1750063.

[7] Christof Gattringer and Christian Lang. *Quantum chromodynamics on the lattice: an introductory presentation.* Vol. 788. Springer Science & Business Media, 2009.

[8] Heinz J Rothe. *Lattice Gauge Theories: An Introduction Third Edition.* Vol. 74. World Scientific Publishing Company, 2005.

[9] P Weisz. "Continuum limit improved lattice action for pure yang-mills theory (i)". In: *Nuclear Physics B* 212.1 (1983), pp. 1–17.

[10] Martin Lüscher and Peter Weisz. "Computation of the action for on-shell improved lattice gauge theories at weak coupling". In: *Physics Letters B* 158.3 (1985), pp. 250–254.

[11] K. Symanzik. "Mathematical problems in theoretical physics, Lecture Notes in Physics". In: 153 (1982).

[12] Kurt Symanzik. "Continuum limit and improved action in lattice theories:(I). Principles and $\varphi 4$ theory". In: *Nuclear Physics B* 226.1 (1983), pp. 187–204.

[13] Bijan Sheikholeslami and Ralf Wohlert. "Improved continuum limit lattice action for QCD with Wilson fermions". In: *Nuclear Physics B* 259.4 (1985), pp. 572–596.

[14] Stefano Capitani, Stephan Dürr, and Christian Hoelbling. "Rationale for UV-filtered clover fermions". In: *Journal of High Energy Physics* 2006.11 (2006), p. 028.

[15] Anna Hasenfratz and Francesco Knechtli. "Flavor symmetry and the static potential with hypercubic blocking". In: *Physical Review D* 64.3 (2001), p. 034504.

[16] Colin Morningstar and Mike Peardon. "Analytic smearing of SU (3) link variables in lattice QCD". In: *Physical Review D* 69.5 (2004), p. 054501.

[17] Marcus Petschlies et al. "P-wave $\pi\pi$ scattering and the ρ resonance from lattice QCD". In: (2017).

[18] Steven Gottlieb et al. "Hadronic coupling constants in lattice gauge theory". In: *Nuclear Physics B* 263.3-4 (1986), pp. 704–730.

[19] Craig McNeile, Christopher Michael, Ukqcd Collaboration, et al. "Hadronic decay of a vector meson from the lattice". In: *Physics Letters B* 556.3-4 (2003), pp. 177–184.

[20] Sinya Aoki et al. "Lattice QCD calculation of the ρ meson decay width". In: *Physical Review D* 76.9 (2007), p. 094506.

[21] Meinulf Göckeler et al. "Extracting the rho resonance from lattice QCD simulations at small quark masses". In: *arXiv preprint arXiv:0810.5337* (2008).

[22] Karl Jansen et al. "Meson masses and decay constants from unquenched lattice QCD". In: *Physical Review D* 80.5 (2009), p. 054510.

[23] Xu Feng et al. "Resonance parameters of the ρ meson from lattice QCD". In: *Physical Review D* 83.9 (2011), p. 094505.

[24] Julien Frison et al. "Rho decay width from the lattice". In: *arXiv preprint arXiv:1011.3413* (2010).

[25] CB Lang et al. "Coupled channel analysis of the ρ meson decay in lattice QCD". In: *Physical Review D* 84.5 (2011), p. 054503.

[26] PACS-CS Collaboratin et al. "ρ meson decay in 2+ 1 flavor lattice QCD". In: *Physical Review D* 84.9 (2011), p. 094505.

[27] Craig Pelissier and Andrei Alexandru. "Resonance parameters of the rho-meson from asymmetrical lattices". In: *Physical Review D* 87.1 (2013), p. 014503.

[28]   Jozef J Dudek et al. "Energy dependence of the ρ resonance in $\pi\,\pi$ elastic scattering from lattice QCD". In: *Physical Review D* 87.3 (2013), p. 034505.

[29]   David J Wilson et al. "Coupled $\pi\,\pi$, K K⁻ scattering in P-wave and the ρ resonance from lattice QCD". In: *Physical Review D* 92.9 (2015), p. 094502.

[30]   John Bulava et al. "I= 1 and I= 2 π–π scattering phase shifts from Nf= 2+ 1 lattice QCD". In: *Nuclear Physics B* 910 (2016), pp. 842–867.

[31]   Bin Hu et al. "Two-Flavor Simulations of ρ (770) and the Role of the K K⁻ Channel". In: *Physical review letters* 117.12 (2016), p. 122001.

[32]   Dehua Guo et al. "Rho resonance parameters from lattice QCD". In: *Physical Review D* 94.3 (2016), p. 034501.

[33]   Ziwen Fu and Lingyun Wang. "Studying the ρ resonance parameters with staggered fermions". In: *Physical Review D* 94.3 (2016), p. 034505.

[34]   Christian Andersen et al. "The I= 1 pion–pion scattering amplitude and timelike pion form factor from Nf= 2+ 1 lattice QCD". In: *Nuclear Physics B* 939 (2019), pp. 145–173.

[35]   Jozef J Dudek and Robert G Edwards. "Hybrid baryons in QCD". In: *Physical Review D* 85.5 (2012), p. 054016.

[36]   CB Lang and V Verduci. "Scattering in the π N negative parity channel in lattice QCD". In: *Physical Review D* 87.5 (2013), p. 054502.

[37]   Christian B Lang et al. "Pion-nucleon scattering in the Roper channel from lattice QCD". In: *Physical Review D* 95.1 (2017), p. 014510.

[38]   Christian Walther Andersen et al. "Elastic I= 3/2 p-wave nucleon-pion scattering amplitude and the Δ (1232) resonance from N f= 2+ 1 lattice QCD". In: *Physical Review D* 97.1 (2018), p. 014506.

[39]   Constantia Alexandrou et al. "Determination of Δ-resonance parameters from lattice QCD". In: *Physical Review D* 88.3 (2013), p. 031501.

[40]   Valentina Verduci and Christian B Lang. "Baryon resonances coupled to Pion-Nucleon states in lattice QCD". In: *arXiv preprint arXiv:1412.0701* (2014).

[41]   Constantia Alexandrou et al. "Study of decuplet baryon resonances from lattice QCD". In: *Physical Review D* 93.11 (2016), p. 114515.

[42]   Christian Walther Andersen et al. "I= 3/2 nucleon-pion scattering and the Delta (1232) resonance on 2+ 1 flavor CLS ensembles using the stochastic LapH method". In: *arXiv preprint arXiv:1911.10021* (2019).

[43] Craig McNeile. "Meson and baryon spectroscopy on a lattice". In: *Hadronic Physics from Lattice QCD*. World Scientific, 2004, pp. 1–101.

[44] Michael L Wagman, Martin J Savage, Nplqcd Collaboration, et al. "Statistics of baryon correlation functions in lattice QCD". In: *Physical Review D* 96.11 (2017), p. 114508.

[45] Silas R Beane et al. "High statistics analysis using anisotropic clover lattices: Single hadron correlation functions". In: *Physical Review D* 79.11 (2009), p. 114502.

[46] Colin Morningstar et al. "Extended hadron and two-hadron operators of definite momentum for spectrum calculations in lattice QCD". In: *Physical Review D* 88.1 (2013), p. 014511.

[47] Ulf-G Meißner. "Progress in Meson-Nucleon Physics: Status and Perspectives". In: *arXiv preprint hep-ph/0108133* (2001).

[48] Manoj Shrestha and D Mark Manley. "Multichannel parametrization of π N scattering amplitudes and extraction of resonance parameters". In: *Physical Review C* 86.5 (2012), p. 055203.

[49] Ulf-G Meißner. "The Beauty of Spin". In: *Journal of Physics: Conference Series*. Vol. 295. 1. IOP Publishing. 2011, p. 012001.

[50] L Alvarez-Ruso et al. "NuSTEC White Paper: Status and challenges of neutrino–nucleus scattering". In: *Progress in Particle and Nuclear Physics* 100 (2018), pp. 1–68.

[51] Claudia Patrignani et al. "Review of particle physics, 2016-2017". In: *Chin. Phys. C* 40 (2016), p. 100001.

[52] L David Roper, Robert M Wright, and Bernard T Feld. "Energy-dependent pion-nucleon phase-shift analysis". In: *Physical Review* 138.1B (1965), B190.

[53] *Scattering Theory 1*. URL: https://www.asc.ohio-state.edu/physics/ntg/8805/notes/section_3_Scattering_1.pdf. 2014.

[54] Jun John Sakurai and Eugene D Commins. *Modern quantum mechanics, revised edition*. 1995.

[55] Lev Davidovich Landau and Evgenii Mikhailovich Lifshitz. *Quantum mechanics: non-relativistic theory*. Vol. 3. Elsevier, 2013.

[56] John R Taylor. *Scattering theory: the quantum theory of nonrelativistic collisions*. Courier Corporation, 2006.

[57] M Döring et al. "Analytic properties of the scattering amplitude and resonances parameters in a meson exchange model". In: *arXiv preprint arXiv:0903.4337* (2009).

[58] Masaharu Tanabashi et al. "Review of particle physics". In: *Physical Review D* 98.3 (2018), p. 030001.

[59] SU Chung et al. "Partial wave analysis in K-matrix formalism". In: *Annalen der Physik* 507.5 (1995), pp. 404–430.

[60] Eugene P Wigner. "Resonance reactions and anomalous scattering". In: *Physical Review* 70.1-2 (1946), p. 15.

[61] Eugene Paul Wigner and Leonard Eisenbud. "Higher angular momenta and long range interaction in resonance reactions". In: *Physical Review* 72.1 (1947), p. 29.

[62] David J Wilson et al. "Resonances in coupled π K, η K scattering from lattice QCD". In: *Physical Review D* 91.5 (2015), p. 054008.

[63] Suh Urk Chung. *Spin formalisms*. Tech. rep. CERN, 1971.

[64] Derek B Leinweber, Terrence Draper, and RM Woloshyn. "Decuplet baryon structure from lattice QCD". In: *Physical Review D* 46.7 (1992), p. 3067.

[65] Huey-Wen Lin, Harvey B Meyer, and David Richards. *Lattice QCD for Nuclear Physics*. Springer, 2015.

[66] Subhasish Basak et al. "Group-theoretical construction of extended baryon operators in lattice QCD". In: *Physical Review D* 72.9 (2005), p. 094506.

[67] F Albert Cotton. *Chemical applications of group theory*. John Wiley & Sons, 2003.

[68] Simon L Altmann. *Rotations, quaternions, and double groups*. Courier Corporation, 2005.

[69] Kari Rummukainen and Steven Gottlieb. "Resonance scattering phase shifts on a non-rest frame lattice". In: *arXiv preprint hep-lat/9503028* (1995).

[70] Meinulf Göckeler et al. "Scattering phases for meson and baryon resonances on general moving-frame lattices". In: *Physical Review D* 86.9 (2012), p. 094513.

[71] Sasa Prelovsek, U Skerbis, and CB Lang. "Lattice operators for scattering of particles with spin". In: *Journal of High Energy Physics* 2017.1 (2017), p. 129.

[72] Dmitrii Aleksandrovich Varshalovich, Anatoli Nikolaevitch Moskalev, and Valerii Kel'manovich Khersonskii. *Quantum theory of angular momentum*. World Scientific, 1988.

[73] Veronique Bernard et al. "Resonance properties from the finite-volume energy spectrum". In: *Journal of high energy physics* 2008.08 (2008), p. 024.

[74] RC Johnson. "Angular momentum on a lattice". In: *Physics Letters B* 114.2-3 (1982), pp. 147–151.

[75] Adam C Lichtl. "Quantum operator design for lattice baryon spectroscopy". In: *arXiv preprint hep-lat/0609019* (2006).

[76] Ikuro Sato. "Lattice QCD Simulations of Baryon Spectra and Development of Improved Interpolating Field Operators". PhD thesis. 2005.

[77] Luciano Maiani and Marianna Testa. "Final state interactions from Euclidean correlation functions". In: *Physics Letters B* 245.3-4 (1990), pp. 585–590.

[78] Martin Lüscher. "Two-particle states on a torus and their relation to the scattering matrix". In: *Nuclear Physics B* 354.2-3 (1991), pp. 531–578.

[79] Xu Feng, Karl Jansen, and Dru B Renner. "A new moving frame to extract scattering phases in lattice QCD". In: *arXiv preprint arXiv:1104.0058* (2011).

[80] Zohreh Davoudi and Martin J Savage. "Improving the volume dependence of two-body binding energies calculated with lattice QCD". In: *Physical Review D* 84.11 (2011), p. 114502.

[81] Ziwen Fu. "Rummukainen-Gottlieb formula on a two-particle system with different masses". In: *Physical Review D* 85.1 (2012), p. 014506.

[82] Luka Leskovec and Sasa Prelovsek. "Scattering phase shifts for two particles of different mass and nonzero total momentum in lattice qcd". In: *Physical Review D* 85.11 (2012), p. 114507.

[83] Raúl A Briceno, Jozef J Dudek, and Ross D Young. "Scattering processes and resonances from lattice QCD". In: *Reviews of Modern Physics* 90.2 (2018), p. 025001.

[84] Albert Messiah. *Quantum mechanics: volume II*. North-Holland Publishing Company Amsterdam, 1962.

[85] M Weissbluth. *Static Fields in Atoms and Molecules*. 1978.

[86] Guenther Gsaller. *"Molecular Point Groups"*. Wolfram Demonstrations Project. URL: http://demonstrations.wolfram.com/MolecularPointGroups/.

[87] JR Green et al. "Nucleon electromagnetic form factors from lattice QCD using a nearly physical pion mass". In: *Physical Review D* 90.7 (2014), p. 074507.

[88] S Dürr et al. "Lattice QCD at the physical point: Simulation and analysis details". In: *Journal of high energy physics* 2011.8 (2011), p. 148.

[89] Constantia Alexandrou et al. "P-wave $\pi \pi$ scattering and the ρ resonance from lattice QCD". In: *Physical Review D* 96.3 (2017), p. 034525.

[90] C McNeile and Christopher Michael. "Decay width of light quark hybrid meson from the lattice". In: *Physical Review D* 73.7 (2006), p. 074506.

[91] Stefan Güsken et al. "Non-singlet axial vector couplings of the baryon octet in lattice QCD". In: *Phys. Lett. B* 227.WU-B-89-9 (1989), pp. 266–269.

[92] Jozef J Dudek et al. "Toward the excited meson spectrum of dynamical QCD". In: *Physical Review D* 82.3 (2010), p. 034508.

[93] Martin Lüscher and Ulli Wolff. "How to calculate the elastic scattering matrix in two-dimensional quantum field theories by numerical simulation". In: *Nuclear Physics B* 339.1 (1990), pp. 222–252.

[94] Benoit Blossier et al. "On the generalized eigenvalue method for energies and matrix elements in lattice field theory". In: *Journal of High Energy Physics* 2009.04 (2009), p. 094.

[95] Christopher Michael. "Adjoint sources in lattice gauge theory". In: *Nuclear Physics B* 259.1 (1985), pp. 58–76.

[96] Kostas Orginos and David Richards. "Improved methods for the study of hadronic physics from lattice QCD". In: *Journal of Physics G: Nuclear and Particle Physics* 42.3 (2015), p. 034011.

[97] Constantia Alexandrou et al. "$\pi \gamma \to \pi \pi$ transition and the ρ radiative decay width from lattice QCD". In: *Physical Review D* 98.7 (2018), p. 074502.

[98] Derek B Leinweber et al. "Baryon spectroscopy in lattice QCD". In: *Lattice Hadron Physics*. Springer, 2005, pp. 71–112.

[99] Subhasish Basak et al. "Lattice QCD determination of patterns of excited baryon states". In: *Physical Review D* 76.7 (2007), p. 074504.

[100] Peng Guo et al. "Coupled-channel scattering on a torus". In: *Physical Review D* 88.1 (2013), p. 014501.

[101] Vladimir Pascalutsa and Marc Vanderhaeghen. "Chiral effective-field theory in the Δ (1232) region: Pion electroproduction on the nucleon". In: *Physical Review D* 73.3 (2006), p. 034003.

[102] V Baru et al. "Precision calculation of the π- d scattering length and its impact on threshold πN scattering". In: *Physics Letters B* 694.4-5 (2011), pp. 473–477.

[103] Peter C Bruns, Maxim Mai, and Ulf-G Meißner. "Chiral dynamics of the S11 (1535) and S11 (1650) resonances revisited". In: *Physics Letters B* 697.3 (2011), pp. 254–259.

[104] G Höhler. "Pion nucleon scattering. Part 2: Methods and results of phenomenological analyses". In: *Landolt–Börnstein* 9 (1983).

[105] Valentina Verduci and Sasa Prelovsek. "Pion-nucleon scattering in lattice QCD". PhD thesis. PhD thesis, Graz U, 2014.

[106] KA Olive. "Review of particle physics". In: *Chinese Physics. C, High Energy Physics and Nuclear Physics* 40.FERMILAB-PUB-16-568 (2016).

[107] Thomas R Hemmert, Barry R Holstein, and Nimai C Mukhopadhyay. "NN, NΔ couplings and the quark model". In: *Physical Review D* 51.1 (1995), p. 158.

[108] Craig McNeile, Christopher Michael, and Petrus Pennanen. "Hybrid meson decay from the lattice". In: *Physical Review D* 65.9 (2002), p. 094505.

[109] Gunnar S Bali et al. "ρ and K* resonances on the lattice at nearly physical quark masses and N f= 2". In: *Physical Review D* 93.5 (2016), p. 054509.

[110] Gert Aarts. "Introductory lectures on lattice QCD at nonzero baryon number". In: *arXiv preprint arXiv:1512.05145* (2015).

[111] Mark Alford, Anton Kapustin, and Frank Wilczek. "Imaginary chemical potential and finite fermion density on the lattice". In: *Physical Review D* 59.5 (1999), p. 054502.

[112] Philippe de Forcrand and Owe Philipsen. "The QCD phase diagram for small densities from imaginary chemical potential". In: *Nuclear Physics B* 642.1-2 (2002), pp. 290–306. ISSN: 0550-3213. DOI: 10.1016/s0550-3213(02)00626-0. URL: http://dx.doi.org/10.1016/S0550-3213(02)00626-0.

[113] Philippe De Forcrand and Owe Philipsen. "The QCD phase diagram for three degenerate flavors and small baryon density". In: *Nuclear Physics B* 673.1-2 (2003), pp. 170–186.

[114] Philippe de Forcrand and Owe Philipsen. "The chiral critical line ofNf= 2+1 QCD at zero and non-zero baryon density". In: *Journal of High Energy Physics* 2007.01 (2007), pp. 077–077. ISSN: 1029-8479. DOI: 10.1088/1126-6708/2007/01/077. URL: http://dx.doi.org/10.1088/1126-6708/2007/01/077.

[115] Philippe De Forcrand and Owe Philipsen. "The chiral critical point of Nf= 3 QCD at finite density to the order (μ/T) 4". In: *Journal of High Energy Physics* 2008.11 (2008), p. 012.

[116] Massimo D'Elia and Maria-Paola Lombardo. "Finite density QCD via an imaginary chemical potential". In: *Physical Review D* 67.1 (2003), p. 014505.

[117] Massimo D'Elia and Maria-Paola Lombardo. "QCD thermodynamics from an imaginary μ B: results on the four flavor lattice model". In: *Physical Review D* 70.7 (2004), p. 074509.

[118] Vicente Azcoiti et al. "Phase diagram of QCD with four quark flavors at finite temperature and baryon density". In: *Nuclear Physics B* 723.1-2 (2005), pp. 77–90.

[119] He-Sheng Chen and Xiang-Qian Luo. "Phase diagram of QCD at finite temperature and chemical potential from lattice simulations with dynamical Wilson quarks". In: *Physical Review D* 72.3 (2005), p. 034504.

[120] Felix Karbstein and Michael Thies. "How to get from imaginary to real chemical potential". In: *Physical Review D* 75.2 (2007), p. 025003.

[121] Paolo Cea et al. "Analytic continuation from imaginary to real chemical potential in two-color QCD". In: *Journal of High Energy Physics* 2007.02 (2007), p. 066.

[122] Paolo Cea et al. "Phase diagram of QCD with four degenerate quarks". In: *Physical Review D* 81.9 (2010), p. 094502.

[123] Liang-Kai Wu, Xiang-Qian Luo, and He-Sheng Chen. "Phase structure of lattice QCD with two flavors of Wilson quarks at finite temperature and chemical potential". In: *Physical Review D* 76.3 (2007), p. 034505.

[124] Keitaro Nagata and Atsushi Nakamura. "Imaginary chemical potential approach for the pseudocritical line in the QCD phase diagram with clover-improved Wilson fermions". In: *Physical Review D* 83.11 (2011), p. 114507.

[125] Massimo D'Elia, Francesco Di Renzo, and Maria Paola Lombardo. "Strongly interacting quark-gluon plasma, and the critical behavior of QCD at imaginary μ". In: *Physical Review D* 76.11 (2007), p. 114509.

[126] Paolo Cea et al. "Analytic continuation of the critical line: suggestions for QCD". In: *Physical Review D* 80.3 (2009), p. 034501.

[127] Andrei Alexandru and Anyi Li. "QCD at imaginary chemical potential with Wilson fermions". In: *arXiv preprint arXiv:1312.1201* (2013).

[128] Paolo Cea et al. "Critical line of two-flavor QCD at finite isospin or baryon densities from imaginary chemical potentials". In: *Physical Review D* 85.9 (2012), p. 094512.

[129] Claudio Bonati et al. "Chiral phase transition in two-flavor QCD from an imaginary chemical potential". In: *Physical Review D* 90.7 (2014), p. 074030.

[130] Michele Andreoli et al. "Gauge-invariant screening masses and static quark free energies in N f= 2+ 1 QCD at nonzero baryon density". In: *Physical Review D* 97.5 (2018), p. 054515.

[131] Andre Roberge and Nathan Weiss. "Gauge theories with imaginary chemical potential and the phases of QCD". In: *Nuclear Physics B* 275.4 (1986), pp. 734–745.

[132] Hiroaki Kouno et al. "The Roberge–Weiss phase transition and its endpoint". In: *Journal of Physics G: Nuclear and Particle Physics* 36.11 (2009), p. 115010.

[133] Yuji Sakai et al. "Determination of QCD phase diagram from the imaginary chemical potential region". In: *Physical Review D* 79.9 (2009), p. 096001.

[134] Yuji Sakai et al. "Entanglement between deconfinement transition and chiral symmetry restoration". In: *Physical Review D* 82.7 (2010), p. 076003.

[135] Takahiro Sasaki et al. "Quark-mass dependence of the three-flavor QCD phase diagram at zero and imaginary chemical potential: Model prediction". In: *Physical Review D* 84.9 (2011), p. 091901.

[136] Hiroaki Kouno et al. "Spontaneous parity and charge-conjugation violations at real isospin and imaginary baryon chemical potentials". In: *Physical Review D* 85.1 (2012), p. 016001.

[137] Gert Aarts, S Prem Kumar, and James Rafferty. "Holographic Roberge-Weiss transitions". In: *Journal of High Energy Physics* 2010.7 (2010), pp. 1–33.

[138] Claudio Bonati et al. "Roberge-Weiss endpoint in N f= 2 QCD". In: *Physical Review D* 83.5 (2011), p. 054505.

[139] Massimo D'Elia and Francesco Sanfilippo. "Order of the Roberge-Weiss endpoint (finite size transition) in QCD". In: *Physical Review D* 80.11 (2009), p. 111501.

[140] Philippe de Forcrand and Owe Philipsen. "Constraining the QCD phase diagram by tricritical lines at imaginary chemical potential". In: *Physical review letters* 105.15 (2010), p. 152001.

[141] Claudio Bonati et al. "Roberge-Weiss endpoint at the physical point of N f= 2+ 1 QCD". In: *Physical Review D* 93.7 (2016), p. 074504.

[142] Alan M Ferrenberg and Robert H Swendsen. "New Monte Carlo technique for studying phase transitions". In: *Physical review letters* 61.23 (1988), p. 2635.

[143] Martin Lüscher. "Properties and uses of the Wilson flow in lattice QCD". In: *Journal of High Energy Physics* 2010.8 (2010), p. 71.

[144] Szabolcs Borsanyi et al. "High-precision scale setting in lattice QCD". In: *Journal of High Energy Physics* 2012.9 (2012), pp. 1–15.

[145] Maarten FL Golterman and Jan Smit. "Lattice baryons with staggered fermions". In: *Nuclear Physics B* 255 (1985), pp. 328–340.

[146] Andrea Pelissetto and Ettore Vicari. "Critical phenomena and renormalization-group theory". In: *Physics Reports* 368.6 (2002), pp. 549–727.

[147] HWJ Blote, Erik Luijten, and Jouke R Heringa. "Ising universality in three dimensions: a Monte Carlo study". In: *Journal of Physics A: Mathematical and General* 28.22 (1995), p. 6289.

[148] Claudio Bonati et al. "QCD simulations with staggered fermions on GPUs". In: *Computer Physics Communications* 183.4 (2012), pp. 853–863.

[149] Claudio Bonati and Massimo D'Elia. "Three-dimensional, three-state Potts model in a negative external field". In: *Physical Review D* 82.11 (2010), p. 114515.

[150] Owe Philipsen and Christopher Pinke. "Nature of the Roberge-Weiss transition in N f= 2 QCD with Wilson fermions". In: *Physical Review D* 89.9 (2014), p. 094504.

[151] Christopher Czaban et al. "Roberge-Weiss transition in N f= 2 QCD with Wilson fermions and N τ= 6". In: *Physical Review D* 93.5 (2016), p. 054507.

APPENDIX

Appendix A

Gamma matrices

The Euclidean DeGrand-Rossi γ-matrices in use in this work are listed:

$$\gamma_x = \begin{pmatrix} 0 & 0 & 0 & i \\ 0 & 0 & i & 0 \\ 0 & -i & 0 & 0 \\ -i & 0 & 0 & 0 \end{pmatrix} = \begin{pmatrix} 0 & i\sigma_x \\ -i\sigma_x & 0 \end{pmatrix} \tag{A.1}$$

$$\gamma_y = \begin{pmatrix} 0 & 0 & 0 & -1 \\ 0 & 0 & 1 & 0 \\ 0 & 1 & 0 & 0 \\ -1 & 0 & 0 & 0 \end{pmatrix} = \begin{pmatrix} 0 & -i\sigma_y \\ i\sigma_y & 0 \end{pmatrix} \tag{A.2}$$

$$\gamma_z = \begin{pmatrix} 0 & 0 & i & 0 \\ 0 & 0 & 0 & -i \\ -i & 0 & 0 & 0 \\ 0 & i & 0 & 0 \end{pmatrix} = \begin{pmatrix} 0 & i\sigma_z \\ -i\sigma_z & 0 \end{pmatrix} \tag{A.3}$$

$$\gamma_t = \begin{pmatrix} 0 & 0 & 1 & 0 \\ 0 & 0 & 0 & 1 \\ 1 & 0 & 0 & 0 \\ 0 & 1 & 0 & 0 \end{pmatrix} = \begin{pmatrix} 0 & \mathbb{1} \\ \mathbb{1} & 0 \end{pmatrix} \tag{A.4}$$

where σ_i are the Pauli matrices.

Appendix B
Additional tables

Group	O_h^D	C_{4v}^D	C_{2v}^D	C_{3v}^D
P_{ref}	$(0,0,0)$	$(0,0,1)$	$(0,1,1)$	$(1,1,1)$
		$(1,0,0)$	$(0,1,-1)$	$(1,1,-1)$
		$(0,-1,0)$	$(1,0,1)$	$(1,-1,1)$
			$(1,0,-1)$	$(1,-1,-1)$
			$(1,1,0)$	
			$(1,-1,0)$	
$\#P_{ref}$	1	3	6	4
$\#P_{init}$, $\#P_{final}$	27	18	12	8
$\#P_{init}\times \#P_{final} = \#P_{frame}$	729	324	144	64
$\#P_{frame}\times \#P_{ref}$	729	972	864	256
$\#P_{init}^{cut}$, $\#P_{final}^{cut}$	7	10	6	8
$\#P_{init}^{cut}\times \#P_{final}^{cut} = \#P_{frame}^{cut}$	49	100	36	64
$\#P_{frame}^{cut}\times \#P_{ref}$	49	300	216	256

Table B.1 List of reference momentum directions used in this work. Also listed are the numbers of momentum combinations for each frame combining initial and final states, without and with the cut on high momentum ($|\vec{p}_\pi| + |\vec{p}_N| \leq \sqrt{3}\frac{2\pi}{L}$).

Label	Axes	Rotation of $2\pi/n$:C_{nl}
Ox	$[1,0,0]$	$C_{2x} = C_{4y}C_{4y}C_{4z}C_{4z}$
Oy	$[0,1,0]$	$C_{2y} = C_{4y}C_{4y}$
Oz	$[0,0,1]$	$C_{2z} = C_{4z}C_{4z}$
Oa	$[1,1,0]$	$C_{2a} = C_{2y}C_{4z}$
Ob	$[1,-1,0]$	$C_{2b} = C_{2x}C_{4z}$
Oc	$[1,0,1]$	$C_{2c} = C_{4y}C_{2z}$
Od	$[-1,0,1]$	$C_{2d} = C_{2z}C_{4y}$
Oe	$[0,1,1]$	$C_{2e} = C_{2z}C_{4x}$
Of	$[0,1,-1]$	$C_{2f} = C_{2y}C_{4x}$
$O\alpha$	$[-1,-1,-1]$	$C_{3\alpha} = C_{4y}^{-1}C_{4z}$
$O\beta$	$[-1,1,-1]$	$C_{3\beta} = C_{4y}^{-1}C_{4z}C_{2y}$
$O\gamma$	$[1,-1,-1]$	$C_{3\gamma} = C_{2y}C_{4x}C_{4y}C_{2z}$
$O\delta$	$[1,1,1]$	$C_{3\delta} = C_{4y}C_{4z}$

Table B.2 Label and axes of symmetry (following convention in [46]). On the right side are the definitions of the rotations from two given initial rotation element: C_{4y} and C_{4z}.

$\mathcal{C}_1$	$\mathcal{C}_2$	$\mathcal{C}_3$	$\mathcal{C}_4$	$\mathcal{C}_5$	$\mathcal{C}_6$	$\mathcal{C}_7$	$\mathcal{C}_8$
E	$C_{3\alpha}$	C_{2x}	C_{4x}	C_{2a}	$\overline{E}$	$\overline{C}_{3\alpha}$	$\overline{C}_{4x}$
	$C_{3\beta}$	C_{2y}	C_{4y}	C_{2b}		$\overline{C}_{3\beta}$	$\overline{C}_{4y}$
	$C_{3\gamma}$	C_{2z}	C_{4z}	C_{2c}		$\overline{C}_{3\gamma}$	$\overline{C}_{4z}$
	$C_{3\delta}$	$\overline{C}_{2x}$	C_{4x}^{-1}	C_{2d}		$\overline{C}_{3\delta}$	$\overline{C}_{4x}^{-1}$
	$C_{3\alpha}^{-1}$	$\overline{C}_{2y}$	C_{4y}^{-1}	C_{2e}		$\overline{C}_{3\alpha}^{-1}$	$\overline{C}_{4y}^{-1}$
	$C_{3\beta}^{-1}$	$\overline{C}_{2z}$	C_{4z}^{-1}	C_{2f}		$\overline{C}_{3\beta}^{-1}$	$\overline{C}_{4z}^{-1}$
	$C_{3\gamma}^{-1}$			$\overline{C}_{2a}$		$\overline{C}_{3\gamma}^{-1}$	
	$C_{3\delta}^{-1}$			$\overline{C}_{2b}$		$\overline{C}_{3\delta}^{-1}$	
				$\overline{C}_{2c}$			
				$\overline{C}_{2d}$			
				$\overline{C}_{2e}$			
				$\overline{C}_{2f}$			

Table B.3 Elements of the double group O_h^D (rest Frame) divided into conjugacy classes. E represents the identity element, while $\overline{E}$ is a rotation of 2π by any axis.

109

$\mathcal{C}_1$	$\mathcal{C}_2$	$\mathcal{C}_3$	$\mathcal{C}_4$	$\mathcal{C}_5$	$\mathcal{C}_6$	$\mathcal{C}_7$
E	C_{2z}	C_{4z}	I_sC_{2x}	I_sC_{2a}	$\overline{E}$	$\overline{C}_{4z}$
	$\overline{C}_{2z}$	C_{4z}^{-1}	I_sC_{2y}	I_sC_{2b}		$\overline{C}_{4z}^{-1}$
			$I_s\overline{C}_{2x}$	$I_s\overline{C}_{2a}$		
			$I_s\overline{C}_{2y}$	$I_s\overline{C}_{2b}$		

Table B.4 Elements of the group C_{4v}^D in momentum frame $\vec{P} = \frac{2\pi}{L}[0,0,1]$, divided into conjugacy classes. E is the identity element, and $\overline{E}$ represents a rotation by 2π on any axis.

$\mathcal{C}_1$	$\mathcal{C}_2$	$\mathcal{C}_3$	$\mathcal{C}_4$	$\mathcal{C}_5$
E	C_{2e}	I_sC_{2f}	I_sC_{2x}	$\overline{E}$
	$\overline{C}_{2e}$	$I_s\overline{C}_{2f}$	$I_s\overline{C}_{2x}$	

Table B.5 Elements of the group C_{2v}^D in momentum frame $\vec{P} = \frac{2\pi}{L}[0,1,1]$, divided into conjugacy classes. E is the identity element, and $\overline{E}$ represents a rotation by 2π on any axis.

$\mathcal{C}_1$	$\mathcal{C}_2$	$\mathcal{C}_3$	$\mathcal{C}_4$	$\mathcal{C}_5$	$\mathcal{C}_6$
E	$C_{3\delta}$	I_sC_{2b}	$\overline{E}$	$\overline{C}_{3\delta}$	$I_s\overline{C}_{2b}$
	$C_{3\delta}^{-1}$	I_sC_{2d}		$\overline{C}_{3\delta}^{-1}$	$I_s\overline{C}_{2d}$
		I_sC_{2f}			$I_s\overline{C}_{2f}$

Table B.6 Elements of the group C_{3v}^D in momentum frame $\vec{P} = \frac{2\pi}{L}[1,1,1]$, divided into conjugacy classes. E is the identity element, and $\overline{E}$ represents a rotation by 2π on any axis.

Irrep $\Lambda(dim)$	$F(1)$	$G(2)$	$G_{g/u}(2)$	$H_{g/u}(4)$
$\Gamma^\Lambda(I_s)$	$\mathbb{1}$	$\mathbb{1}$	$\pm\mathbb{1}$	$\pm\mathbb{1}$
$\Gamma^\Lambda(\bar{E})$	$-\mathbb{1}$	$-\mathbb{1}$	$-\mathbb{1}$	$-\mathbb{1}$

Table B.7 Representation matrices for the spatial inversion element and 2π rotation $\bar{E}$ in various irreps Λ.

J^P(used for)	$J^P = 1^-(\vec{p})$	$J^P = 1^+(\Delta)$	$J^P = 1/2^+(N,\Delta)$	$J^P = 0^-(\pi)$
I_s	$-\mathbb{1}$	$\mathbb{1}$	γ_t	$-\mathbb{1}$
$\bar{E}$	$\mathbb{1}$	$\mathbb{1}$	$-\mathbb{1}$	$\mathbb{1}$

Table B.8 Elements for the spatial inversion I_s and 2π rotation $\bar{E}$ for states with quantum numbers $J^P = 1^-, 1^+, 1/2^+, 0^-$.

GROUP	IRREP	OCC.	Row 1	Row 2
O_h^D	G_{1g}	1	$\frac{1}{2}(N_2[0,0,0] + N_4[0,0,0])$	$\frac{1}{2}(N_1[0,0,0] + N_3[0,0,0])$
	G_{1u}	1	$\frac{1}{2}(N_2[0,0,0] - N_4[0,0,0])$	$\frac{1}{2}(N_1[0,0,0] - N_3[0,0,0])$
C_{4v}^D	G_1	1	$N_1[0,0,1]$	$N_2[0,0,1]$
		2	$N_3[0,0,1]$	$N_4[0,0,1]$
C_{2v}^D	G	1	$\frac{\sqrt{3}}{2}N_1[0,1,1] + \frac{i}{2\sqrt{3}}N_2[0,1,1] + \frac{1}{2\sqrt{3}}N_3[0,1,1] - \frac{i}{2\sqrt{3}}N_4[0,1,1]$	$\frac{1}{2}N_1[0,1,1] - \frac{i}{2}N_2[0,1,1] - \frac{1}{2}N_3[0,1,1] + \frac{i}{2}N_4[0,1,1]$
		2	$\frac{1}{\sqrt{6}}N_2[0,1,1] + i\sqrt{\frac{2}{3}}N_3[0,1,1] - \frac{1}{\sqrt{6}}N_4[0,1,1]$	$\frac{1}{\sqrt{2}}N_2[0,1,1] - \frac{1}{\sqrt{2}}N_4[0,1,1]$
C_{3v}^D	G	1	$\sqrt{\frac{2}{3}}N_1[1,1,1] + \frac{(\frac{1}{2}+\frac{i}{2})}{\sqrt{6}}N_2[1,1,1] + \frac{1}{\sqrt{6}}N_3[1,1,1] - \frac{(\frac{1}{2}+\frac{i}{2})}{\sqrt{6}}N_4[1,1,1]$	$\frac{1}{\sqrt{3}}N_1[1,1,1] - \frac{(\frac{1}{2}+\frac{i}{2})}{\sqrt{3}}N_2[1,1,1] - \frac{1}{\sqrt{3}}N_3[1,1,1] - \frac{(\frac{1}{2}+\frac{i}{2})}{\sqrt{3}}N_4[1,1,1]$
		2	$\frac{1}{2}N_2[1,1,1] - (\frac{1}{2}-\frac{i}{2})N_3[1,1,1] - \frac{1}{2}N_4[1,1,1]$	$\frac{1}{\sqrt{2}}N_2[1,1,1] + \frac{1}{\sqrt{2}}N_4[1,1,1]$

Table B.9 Nucleon operators projected for different rows and occurrences in relevant irreps. For brevity is listed only one momentum direction per irrep.